In: Surface Science Research Developments
Editor: Charles P. Norris, pp. 1-73
ISBN 1-59454-158-2

REDOX METALLOPROTEINS ON METAL SURFACES AS HYBRID SYSTEMS FOR BIONANODEVICES: AN EXTENSIVE CHARACTERIZATION AT THE SINGLE MOLECULE LEVEL

B. Bonanni, D. Alliata, L. Andolfi, A. R. Bizzarri, S. Cannistraro*

Biophysics & Nanoscience Centre, INFM
Dipartimento di Scienze Ambientali, Largo dell'Università
Università della Tuscia, I-01100 Viterbo, Italy

Abstract

Molecular bioelectronics is a rapidly growing field at the junction of biochemistry, physics and surface science, which combines selectivity of biology with processing power of modern microelectronics, by integrating biomaterials with electronic elements. Redox metalloproteins have gained considerable interest in view of such applications: their electron transfer (ET) capabilities and possibility of gating redox activity, as well as nanoscale dimensions make them a good candidate for incorporation in hybrid submicrometer-sized electronic components.

The ability to connect functional redox proteins to electrodes, preferably by covalent linkage to ensure good electrical contact between molecules and conducting substrate, is a fundamental step for such applications, and requires full characterization of the adsorbed proteins in terms of topology, spectroscopy, ET properties and conduction, at the single molecule level.

We address this issue by following two alternative approaches, namely focusing our attention on both wild type redox proteins, directly chemisorbed onto gold electrodes via cysteine residues, and engineered redox proteins, which have been suitably mutated to introduce an anchoring group. More specifically, wild type azurin and yeast cytochrome c, bearing a disulphide bridge and a free cysteine residue respectively, are directly adsorbed on bare gold electrode, whereas plastocyanin has been mutated by introducing alternatively a cysteine residue or a disulfide bridge to achieve a stable covalent immobilisation on gold surface.

* **Corresponding author:** Prof. Salvatore Cannistraro, tel: +39 0761 357136 / 027, fax: +39 0761 357179. E-mail: *cannistr@unitus.it*; *http://www.unitus.it/biophysics*

Morphological properties and functionality of such metalloproteins chemisorbed on Au(111) substrates are deeply investigated at the single molecule level by a combination of high-resolution microscopy techniques, such as Atomic Force Microscopy (AFM) and Scanning Tunnelling Microscopy. To gain further insight into the arrangement and orientation of the proteins on gold substrate, their structural and dynamic properties are also investigated by Molecular Dynamics simulations. Moreover, conductive AFM experiments and Scanning Tunnelling Spectroscopy allow to probe ET properties of adsorbed single molecules, as well as to assess the efficient conduction through the single molecule towards the electrode. The characterization is integrated with Cyclic Voltammetry in order to confirm the preserved redox functionality of molecules upon immobilization on gold.

For all systems investigated, we find that adsorbed metalloproteins are strongly bound to gold. A large population of molecules display uniform size, mostly in agreement with crystallographic data. Minor changes are observed in height distribution of different metalloproteins over the substrates, indicative of a slightly more homogenous orientation of molecules adsorbed via a disulphide bridge with respect to adsorption through a single cysteine.

The preserved functionality found for adsorbed molecules and their good coupling with the electrode, along with the high coverage of metal surface, provide clear indication of redox protein efficacy in integration with electronic components, for applications in biosensors and biocatalytic devices.

Abbreviations

AFM	Atomic Force Microscopy
AZ	Azurin
CAFM	Conductive Atomic Force Microscopy
CV	Cyclic Voltammetry
ECSTM	Electrochemical Scanning Tunnelling Microscopy
ET	Electron Transfer
MD	Molecular Dynamics
SPM	Scanning Probe Microscopy
STM	Scanning Tunnelling Microscopy
STS	Scanning Tunnelling Spectroscopy
PC	Plastocyanin
PCSH	Plastocyanin mutant bearing a single thiol
PCSS	Plastocyanin mutant bearing a disulfide bridge
PCWT	Wild Type Plastocyanin
SCE	Saturated Calomel Electrode
SHE	Standard Hydrogen Electrode
TMAFM	Tapping Mode Atomic Force Microscopy
YCC	Yeast Cytochrome c

1 Introduction

Molecular bioelectronics is a rapidly growing field at the junction of biochemistry, physics and surface science, which integrates biomaterials with electronic transducers [1, 2]. The molecular building blocks of life – as proteins, nucleic acids- are examples of biomaterials that possess unique properties determined by their size, folding and patterns at the nanoscale. Integrating biological building blocks into synthetic materials and devices allows to combine natural biological functions, such as binding, catalysis, recognition, self assembly and electron transfer (ET), with processing power of modern microelectronics for the realization of biosensors, devices for driving biotransformations, biofuel cells, and eventually biocomputers [3,4]. The possible applications involve drug and gene delivery, biocompatible nanostructured materials for implantation, artificial photosynthesis for clean energy, and nanoscale sensory systems, with considerable advantages in several fields such as medicine, environmental diagnostics and food and processing industries. Besides such applicative aspects, the increasing nanotechnological capabilities allow fundamental studies of biomaterials at the nanoscale, namely at the single molecule level rather than in bulk, both in their natural environment and as part of hybrid systems, thus addressing outstanding questions belonging to biology, chemistry and physical science. Moreover, by considering that most biological reactions occur at surfaces and interfaces, exploring mutual interaction between individual biomolecules and various surfaces is of fundamental importance [5,6,7].

In this framework, redox metalloproteins have gained considerable interest, not only for the possibility to study their properties at the nanoscale but also in view of nano bioelectronics applications [1,8,9]. Indeed, their inherent ET capability (thanks to the presence of a redox center) is very efficient: the peculiarity of ET processes mediated by metalloproteins is that they occur over long distances and in a very fast, directional way. Moreover, metalloproteins are, in general, part of ET chains where the conduction through the biomolecule occurs at the level of the single electron [10,11]. Such characteristic, besides the possibility of gating redox activity and their nanoscale dimensions, make them a good candidate for incorporation in hybrid submicrometer-sized electronic components [12-16]. Moreover, adsorption of biomolecules on a surface may take advantage of self assembling fabrication techniques [17-18], which allow arrangement of molecules, or group of molecules, in arrays by simply dipping the substrate in a suitable solution, thus representing a simple alternative to conventional optical lithographic techniques.

A variety of techniques can be used to join metalloproteins and electronic components, providing that the redox-active portions of the biomolecule and the electronic component are closely and appropriately positioned for efficient electronic connection. Linking redox proteins to metal electrodes, with preserved functionality of the biomolecule and fast ET from the biological component to the electrode, is of fundamental importance in the design of bionanodevices, and several approaches can be followed. Even if many proteins spontaneously adsorb on solid surfaces through hydrophobic or electrostatic interaction (physical adsorption), they adopt random and likely undesirable orientation and may even denature because of multiple contacts and interactions with the surface, thus compromising their inherent ET capability [2,19,20]. As an alternative to physical adsorption on bare surfaces, electrodes have been often modified, prior to protein deposition, with a layer of organic molecules [18,21-25]. This is the case, for instance, of proteins included in

polyelectrolytes or conduction polymers, which however results in a non-oriented multilayer biomolecule film [26]. Alkane thiol or other thiol-terminated chains can be used, instead, as spacers to link the biomolecule to the surface of a gold electrode with a preferential orientation and controlled density. Indeed, thanks to the high affinity of thiols for gold and self-assembling properties, this organic material can be easily deposited on Au surfaces, via S-Au bonds, in a uniform and stable monolayer [27,28]. The reactive function at the other end of the spacer can be suitably chosen for specific interaction, possibly covalent binding, with one group of the protein, thus providing a controlled distribution of adsorbed proteins over the electrode surface with well defined orientation, favourable for ET. For instance, carboxylic or amino functional ends can be exploited for covalent linkage with amino or carboxylic groups at protein surface [21, 29-31]. Nevertheless, slower ET is often observed for proteins adsorbed on such modified electrodes [32,33], and direct chemisorption of functional proteins on metal surfaces still remains a worthwhile challenge, deserving the advantage of direct ET between the redox-active biomolecule and the electrode. Indeed, direct ET is considered the basis for third generation biosensors [34] since offers the possibility to operate in a potential window closer to the redox potential of the metalloprotein, as well as a higher level of control on the device by possible modulation of biomolecule redox- and ET properties.

By exploiting the high affinity of protein disulphides and thiols for gold, direct chemisorption of functional proteins on Au electrode can be achieved. Experimental and theoretical studies showed a dissociative reduction of a disulphide with subsequent formation of strongly bound thiolates, whereas the binding of thiolates resulting from S–H bond cleavage in thiols is accompanied by the development of molecular hydrogen [27,28,35,36]. Native disulphide and thiols have been often exploited to achieve protein–metal adsorption [21,37-40], or thiol-terminating cysteine residues have been suitably introduced into the surface of metalloproteins (when lacking) by site-directed mutagenesis [41-44] as anchoring group for gold electrodes.

It is of primary importance that the functionality of the chemisorbed protein is preserved [45,46]. Therefore the full characterisation of the topological and conductive properties of redox proteins assembled on metal electrodes, possibly at the single molecule level, is a fundamental step in the development and application of nano bioelectronic devices [1, 2].

In this context, we investigated the direct site-specific attachment of redox proteins to gold. We address this issue following two alternative approaches, namely focusing our attention both on wild type redox proteins, directly chemisorbed onto gold electrodes via cysteine residues, as well as on engineered redox proteins, which have been suitably mutated to introduce an anchoring group. More specifically, wild type azurin (AZ) and yeast cytochrome c (YCC), bearing a disulphide bridge and a free cysteine residue respectively, are directly adsorbed on bare gold electrode [40,47], whereas plastocyanin (PC) has been mutated introducing sulfur based anchoring groups to achieve a stable covalent immobilisation on gold surface [44].

The blue copper protein Pseudomonas aeruginosa AZ is one of the best-characterized redox metalloproteins. This small molecule, (MW=14.6 kD) consisting of 128 amino acid residues, plays an important role as electron carrier in the respiratory chain of denitrifying bacteria, where its role is to transport electrons between cytochrome c551 and cytochrome oxidase. The active site consists of a single copper ion, switching between Cu(I) and Cu (II)

oxidation states during the ET process and located in a hydrophobic core approximately 7 Å from the surface. Opposite to the copper atom, AZ bears an exposed disulfide moiety (Cys3-Cys26), which is suitable for covalent linking to gold surfaces via S-Au bonds. As a matter of fact, AZ can be easily self assembled on gold surfaces [40,42,48]. A schematic representation of the AZ molecule with the anchoring group (S-S) assumed to be 'face down' for covalent binding to gold is shown in Fig. 1 (a).

Poplar PC is a copper-binding protein of only 99 amino acids (10.5 KDa) belonging to the cupredoxin family. This protein functions in photosynthesis as mobile electron carrier, being reduced by cytochrome f, which is part of the cytochrome b6f complex, and oxidized by the chlorophyll P700 reaction centre of photosystem I. Its structural features include a distorted tetrahedral copper site at one end of an eight-stranded antiparallel β barrel; the tetrahedral geometry of the copper site facilitates the ET that results from a transition from the oxidized to the reduced state with a characteristic redox potential. To make poplar PC suitable for stable and specific self-assembly onto gold, suitable anchoring groups have been introduced by site-directed mutagenesis [44]. In the first mutant (PCSS), a disulphide bridge is inserted within the protein, while in the second one (PCSH) a residue tail, containing a cysteine, is added as C-terminal extension. Both groups (S–S and S–H) are located in a region of the protein opposite to the copper active site and easily available for chemisorption onto a gold electrode, as schematically represented in Fig. 1 (b), (c).

Mitochondrial cytochromes c are among the best studied proteins to date, and cytochrome c is often used as a 'model protein' in a wide range of different experimental techniques. These hemeproteins function as electron carriers in the photosynthetic and respiratory ET chains. Consequently they interact with other redox proteins (often blue copper proteins) in order to exchange electrons [49]. An heme-iron redox centre is responsible for the ET function; the iron switching its oxidation state between +2 and +3 in biological function. Yeast cytochrome c (YCC) is a small (12.5 KDa) single-domain hemeprotein, which plays a major role in ET between two membrane-bound enzyme complexes, cytochrome c reductase and cytochrome c oxidase. The heme group is covalently bound to the protein matrix through thioether linkages involving two cysteine residues. An additional free sulfur-containing group (Cys102) is present in YCC, and it suitable for specifically oriented immobilisation on gold by covalent binding, as depicted in Fig. 1 (d), with only minor perturbation of the heme group.

The three systems have been extensively characterized in terms of topology, spectroscopy and ET properties at the single molecule level by a combination of several techniques. Morphological properties and redox functionality of individual metalloproteins chemisorbed on gold substrates are deeply investigated by high-resolution microscopy techniques, such as Atomic Force Microscopy (AFM) and Scanning Tunnelling Microscopy (STM) [40, 47, 50]. To gain further insight into the arrangement and orientation of the proteins on gold substrate, their structural and dynamic properties are also studied by Molecular Dynamics (MD) simulations [51,52]. Additionally, conductive AFM (CAFM) experiments and Scanning Tunnelling Spectroscopy (STS) allowed to probe ET properties of adsorbed single molecules, as well as to assess the efficient conduction through the single molecule towards the electrode [50,53]. The characterization is integrated with Cyclic Voltammetry (CV) in order to confirm the preserved redox functionality of molecules upon immobilization on gold [40,47,54].

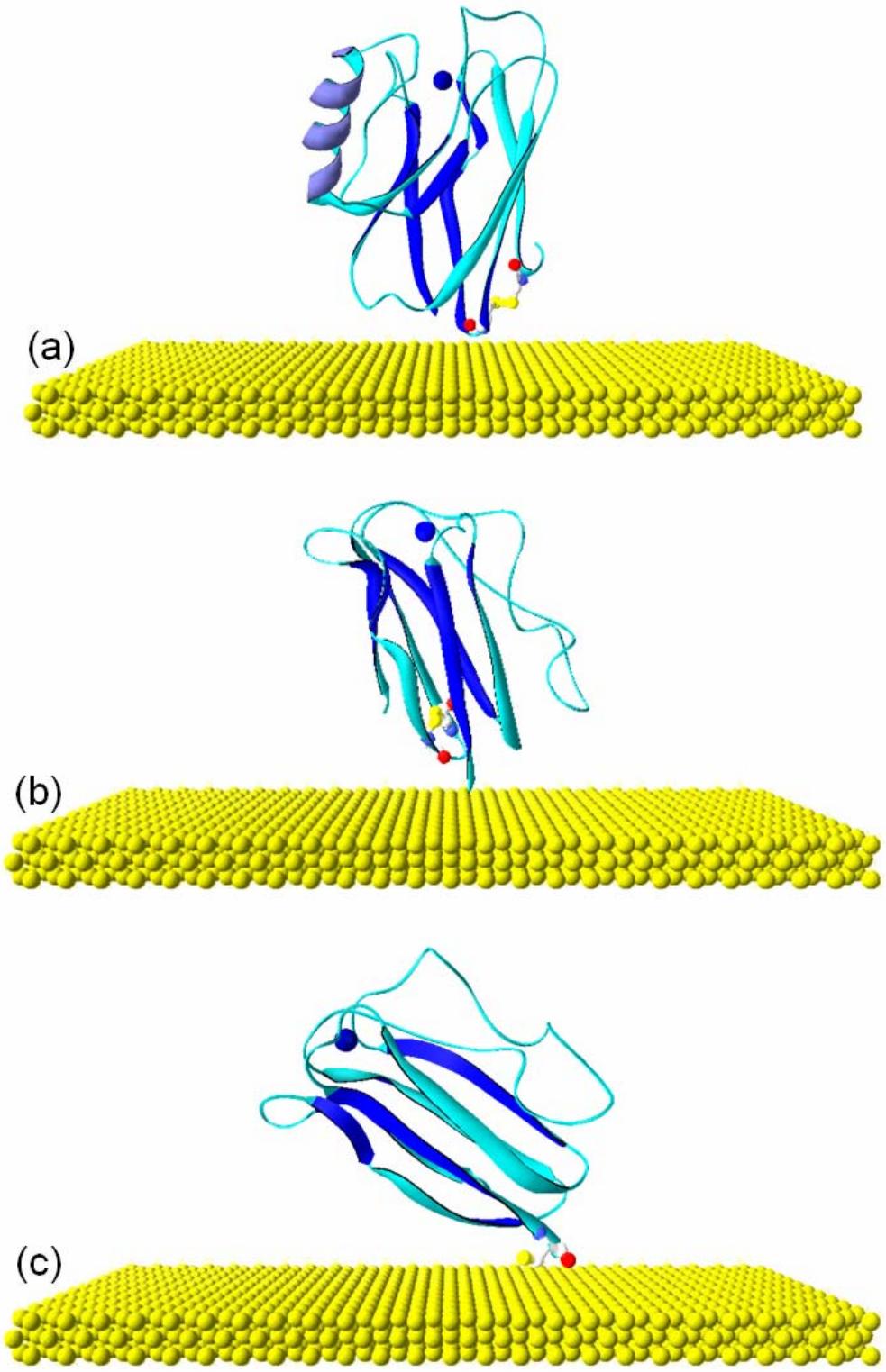
(a)
(b)
(c)

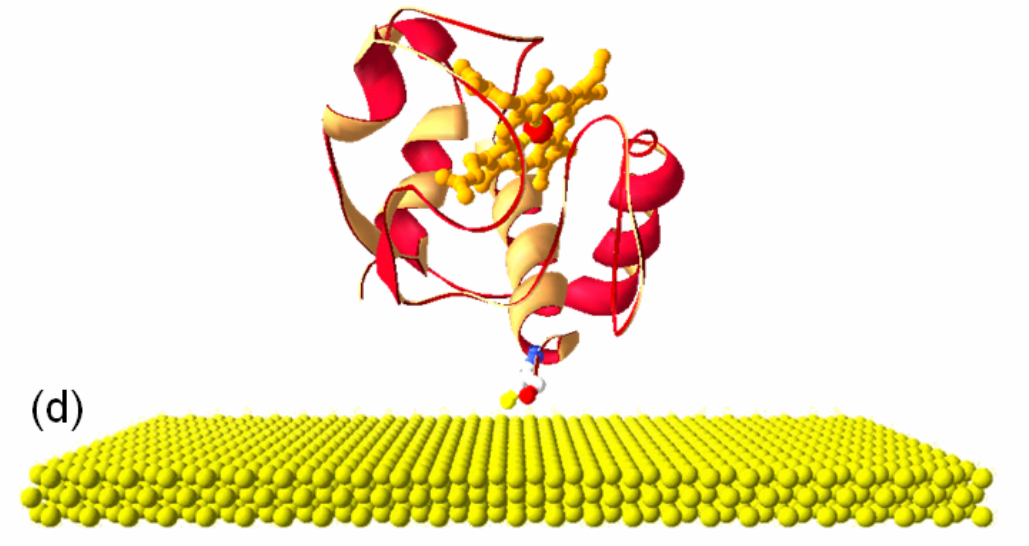

Fig. 1. Graphic representations showing metalloprotein adsorption on Au(111) substrate via the sulfur based anchoring groups. (a) AZ, (b) PCSS mutant, (c) PCSH mutant, (d) YCC. The cysteine residues, suitable for covalent linking to gold via sulfur (in red), are evidenced as well as the active site (the copper atom for proteins in (a), (b), (c) and the heme for YCC in (d)).

2 Description of the Techniques and Experimental Details

2.1 Scanning Tunnelling Microscopy

STM measures a quantum mechanical tunnelling current between a metallic tip, which is sharpened to a single atom point, and a conductive surface. The rate of tunnelling electrons depends sharply (exponentially) on the tip-sample distance [55]; hence if the tunnelling current is kept constant by a suitable feedback loop, the tip will track the sample surface closely, with an overall resolution of tenths of angstroms both in the vertical direction and in the sample plane. The STM image, which is acquired by recording the tip height while scanning the sample surface line by line, is actually a combination of topography and electronic properties of the sample.

Since its introduction, STM has been successfully applied to the study of bio-molecules, like proteins and DNA immobilized on conductive substrates [55-57]. The discovery that STM could be operated in fluid ambient [58,59] opened the feasibility of high-resolution studies of bio-molecules in a near-physiological condition [60]. The introduction of the electrochemical control (ECSTM) extended the potentiality of in situ STM to the investigation of the heterogeneous ET mechanism between bio-molecules and metal electrodes [61,62], whose knowledge is crucial for the development of bioelectronic devices [63]. In this configuration a bipotentiostat is used to suitably tune the electrochemical potential of the substrate and tip in order to sweep the redox levels of the adsorbed metalloprotein, thus investigating the possible contribution of redox levels in the tunnelling mechanism.

In combination to STM, STS can be used to investigate the conductive properties and extract information about electronic states of the sample being imaged. In STS the scan is stopped and I-V data are recorded, with the tip in a fixed position. By selectively positioning the tip for instance over a protein, conductive properties can be investigated at the single molecule level. Additionally, the dI/dV vs V data contain information about the local electronic density of states (LDOS) involved in the tunnelling process.

Despite STM has widely demonstrated to be a powerful tool for investigation of electronic and morphological properties of single molecules, it is commonly accepted that special care has to be dedicated to working conditions. When STM is operated in constant current mode, the estimated height of a single molecule on a flat metal surface corresponds to the tip retraction as governed by the feedback loop, which compensates the piezo position for a variation in current reading. If the tip retraction is not sufficient to overcome the top of the biomolecule, the scans may perturb the soft biological sample. As a matter of fact, the height of bio-molecules, as estimated by STM, is found significantly lower than the expected physical value [41,64].

The knowledge, and the control, of the initial tip to substrate distance is a key requirement to avoid invasive actions in STM and thus to obtain unperturbed imaging of biomolecules, which is fundamental to discriminate between intrinsic conductive properties and tip induced effects. Additionally, quantifying the tip to substrate distance is a essential prerequisite when attempting to model the involvement of electronic levels of a protein in the tunnelling mechanism [65,66], as well as when investigating the conductance properties of a biomolecule. For instance, when performing STS, I–V data are recorded by selectively positioning the tip over a single protein [50, 53, 67, 68] and, if the tip penetrates the biomolecule, it is difficult to infer which part has contributed to the current.

Therefore, special care has to be dedicated to the control of the starting tip-substrate distance. Generally the tip sample separation can be inferred from the tunnelling current and bias voltage settings, once the corresponding tunnelling resistance has been calibrated against the gap width (see paragraph 4.1) [69,70]. The resistance-distance dependence allows establishing the minimum tunnelling resistance at which the tip to substrate distance is at least equal, or even higher, the crystallographic dimension of the biomolecule, so that non-invasive STM imaging can be performed.

2.2 Atomic Force Microscopy

In AFM [71] a sharp tip is located at the end of a soft spring (cantilever), hundreds of microns long. The tip-sample interaction forces (electrostatic, van der Waals, frictional, capillary, binding…) result in cantilever deflections which can be detected with high accuracy, by using a laser beam which bounces off the back of the cantilever onto a position-sensitive photodetector. AFM has an overall resolution in the vertical direction of tenths of Angstrom, usually limited by thermal noise, and is capable of measuring ultra-small forces (as small as subpiconewton). The resolution in the sample plane is generally limited by tip radius of curvature, and is few nanometers; however it can improve up to subnanometers when scanning 2D ordered arrays [72-74]. Traditionally, AFM has been used in contact mode [71], namely measuring topography and friction by simply sliding the probe tip across the sample surface, keeping the tip in “physical contact” with the sample. This technique has been very

successful mostly for hard sample, whereas soft samples can be damaged when imaged in contact mode. This has resulted in the development of alternative AFM modes, aiming to overcome problems associated with friction and adhesion. In tapping mode (TMAFM), shear forces are greatly reduced thanks to the intermittent contact between tip and sample: the cantilever is oscillated vertically using a piezoelectric crystal, just barely "tapping" the sample, and the reduction in oscillation amplitude is used to identify and measure surface features [75]. The possibility to operate TMAFM under aqueous environment makes this technique a powerful tool for the study of biological samples [76-84].

Much work has been devoted at imaging topography of biological molecules with high-resolution; indeed, TMAFM has demonstrated to be a powerful tool to get direct information about molecule height and orientation above the substrate [42, 85-88]. In the past, orientation or adsorption studies of proteins on surfaces have been performed by techniques such as ellipsometry [89], surface plasmon resonance [90], fluorescence spectroscopy [91] or neutron reflectivity [92]. Nevertheless, most of these techniques have been often used to study substrates where a monolayer of proteins had been adsorbed, relating the orientation of molecules to an average value of the protein layer thickness. In contrast, AFM allows single molecule resolution, so that orientation and absorption studies can be performed at concentrations below monolayer coverage, thus minimizing protein-protein interaction. In the present work TMAFM in buffer solution was applied to investigate morphological characteristics of adsorbed proteins, with particular attention to how the molecules are immobilised on the electrode surface and how immobilisation affects their orientation. TMAFM images have been recorded in fluid conditions, thus avoiding sample drying (often needed when applying other techniques) which is likely to produce artefacts. Indeed, the morphological characterization of the adsorbed proteins in physiological conditions allows to eliminate capillary force and minimize height anomalies due to differences in adhesion at the sample surfaces and resulting from the inhomogeneous thickness of the adsorbed water layer [93], thus providing reliable evaluation of molecule height and orientation above the substrate.

AFM can also operate in conductive mode configuration. CAFM is a powerful current sensing technique suitable for the electrical characterization of conductivity variations in highly-to-medium resistive samples. The CAFM approach is complementary to a number of alternative strategies to form two-terminal junctions, such as break junctions [94], nanopores [95], crossed wires [96], and mercury drop contacts [97]. Among basic advantages it should be outlined the absence of nanofabrication steps to form the nano-junctions, and the possibility to change the metals that contact the sample.

In CAFM a bias is applied between an AFM conductive probe and the sample and the current flowing is recorded, while the pressure exercised by the probe is controlled by a feedback loop. In such a way, topography, lateral forces and current images are measured simultaneously in contact mode, and direct correlation of structural features with electrical characteristics is attained. As compared with STM, in CAFM forces, and not current, are used to control the feedback. Therefore, the indetermination on the vertical tip position, that is a key issue in STM [98], is here overcome.

In addition to the imaging mode, the local resistance behaviour of the sample can be investigated as well, by scanning the potential at a fixed point of the surface and recording the current flowing between the AFM tip and the sample. Several studies on organic molecules self-assembled on gold have been performed. Systematic measurements of current-voltage

characteristics on SAM monolayers have been accomplished by Wold and Frisbie [99], where the effect of voltage sweep range, tip radius, molecular structure and applied load on molecular resistance was evidenced. The I-V relation is found to be influenced by the properties of tip-sample contact [45], especially when it is achieved through non chemical bonds [100]. Indeed, it has been demonstrated that a junction formed with the same molecule either physisorbed or chemisorbed on a gold contact shows a different resistance dependence on the applied force [46], the electronic conduction from the molecule to the metal being facilitated when the binding is covalent [101]. To avoid such drawback, nano-gold-particles have been chemisorbed on thiol-terminated molecules so that a stable electrical circuit can be realized by positioning the conductive tip on the nano-metal-contact [102]. Furthermore, by including conjugated molecules within an insulating matrix of alkanes, the electrical resistance of single units could be evaluated [103].

Very recently the CAFM has also been successfully applied on the blue copper protein AZ [104], thus opening a new way to investigate the electrical conductivity of redox-active bio-molecules.

2.3 SPM Technical Details

STM images were acquired by a Picoscan system (Molecular Imaging Co., Phoenix) equipped with a Picostat (Molecular Imaging Co.) bipotentiostat. A 10 μm scanner with a final preamplifier sensitivity of 1 nA/V was used for STM measurements. Images were acquired in constant current mode, using electrochemically etched Pt/Ir tips purchased from Molecular Imaging. The measuring cell for ECSTM consisted of a Teflon ^{TM} ring pressed over the gold substrate operating as a working electrode. A 0.5 mm Pt wire was used as counter electrode and a 0.5 mm Ag wire as a quasi-reference electrode (AgQref). The AgQref potential was measured vs saturated calomel electrode (SCE).

Current–voltage curves were obtained by setting the gap at a tunnelling current of 50 pA and V_{bias} of 0.180 V; disengaging the feedback, the tunnelling current was monitored as the substrate potential is swept over ± 1 V, and every single sweep was collected in 0.01 s.

AFM topographic images of the surface were taken with a commercial microscope (Nanoscope IIIa/Multimode, Digital Instruments, Santa Barbara, Ca) equipped with a 12-μm scanner (E scannner) operating in tapping mode. Oxide-sharpened silicon nitride probes (Digital Instruments), 100 or 200 μm long, with nominal radius of curvature of 20 nm and spring constants of 0.15 and 0.57 N/m, respectively, were used. All protein imaging was performed in buffer solution using the commercial fluid cell (Digital Instruments) without the O-ring seal, in order to minimize lateral drift often caused by O-ring pressure over the sample. Tapping in solution was performed by oscillating the cantilever via a piezoelectric-actuator. Resonance peaks in the frequency response of the cantilever were chosen for the TM oscillation, corresponding to typical tapping frequencies in the range 8-30 KHz. Before engaging, scan size and offsets were set to zero to minimise sample deformation and contamination of the tip. Free oscillation of the cantilever was set to have a root-mean-square amplitude corresponding to ~ 1.5 V. In each measurement, the set point was adjusted before scanning, to minimise the force between the tip and the sample. The typical scan rate was 0.5 Hz.

CAFM measurements were performed by using the PicoSPM (Molecular Imaging Co., Phoenix), equipped with a current sensing module with a sensitivity of 1V/nA. Conductive probes were CSC12 model provided by Micromasch, which consist of standard silicon cantilevers coated by the manufacturer with a thin layer of Gold or Platinum. The typical radius of curvature was less than 50 nm and 40 nm, respectively. Nominal spring constants of 0.05 N/m and 0.08 N/m were used to convert the cantilever deflection signal to the corresponding force values. All cantilever chips were initially rinsed with acetone, ethanol and ultra pure water (Millipore 18.2 MΩ) before use.

2.4 Cyclic Voltammetry

CV is a classical electrochemical technique, which allows to investigate processes at the solid/electrolyte interface, such as adsorption/desorption [105], redox reactions [106], insertion phenomena [107], film formation [108]. CV method consists in sweeping, between two set limits, the electrochemical potential at the working electrode, with the simultaneous measurement of the current [109]. If the electrolyte contains an electrochemically active species, redox processes can be studied.

This technique has been extensively applied to investigate the redox activity of metalloproteins and enzymes and much progress has been made in attaining reproducible electrochemical responses of these biomolecules [110]. Voltammetric studies have led, not only to an enhanced understanding of the important role they play in biological energy transduction processes, (including structure/function correlations) but also to significant biosensing developments and, more recently, of bioelectronics.

Particularly beneficial in this context is the level of control achievable by confining voltammetric investigations to the electrode surface (and thereby removing complicating diffusion-based contributions to voltammetry) [111, 112]. In recent years, we, and others, have developed methods whereby metalloproteins can be assembled on electrode surfaces in well-defined molecular arrays which are electrochemically-addressable [41,54]. The electrode is effectively a redox partner, delivering or removing electrons, with the additional possibility to vary and control the potential (driving force) and measure corresponding rates. For redox proteins, a good indicator that the film has been successfully adsorbed on the electrode without denaturation is the retention in the monolayer of the native redox electrochemistry that is commonly found in solution. The process of ET between planar electrode surface and immobilised metalloproteins has now advanced to the point where detailed kinetic and thermodynamic investigations, including quantitative electronic coupling (such as structure and distance dependency) experiments and reorganization can be pursued [113].

2.4.1 CV Technical Details

CV on protein monolayers adsorbed on gold electrodes was performed with a Picostat bipotentiostat (Molecular Imaging Co., Phoenix). The electrochemical cell housed two Pt wires as counter- and reference electrodes and was filled with 100 µl of buffer solution. The gold substrate served as working electrode, with a geometric area of 0.384 cm^2. Before measuring the cyclic voltammogram of protein adlayers, the faradaic current of the bare Au(111) substrate was recorded. Typical scan rates were in the range 5 - 500 mV/sec.

2.5 Molecular Dynamics Simulations

Classical MD simulations provide a detailed atomic description of a system in a temporal window ranging from femto– to nano or even micro–seconds [114-116]. The classical dynamics of a biomolecule can be simulated, by integrating the Newton equations for each atom, modelled as hard sphere; such an approach involving the computation of the coordinates and velocities of each atom in the system as a function of time. The essential prerequisites are the knowledge of a starting set of atomic coordinates, (for proteins usually obtained from X-ray crystallographic or refined-NMR structure data) and of the interaction potential among atoms. Usually, the interaction potential is represented by an empirical energy function that takes into account for both the bonding and non bonding contributions [114-116]:

$$U(R) = \frac{1}{2}\sum_{bonds} K_b(b-b_o)^2 + \frac{1}{2}\sum_{angle} K_\theta(\theta-\theta_o)^2 + \frac{1}{2}\sum_{dihedrals} K_\chi[1+\cos(n\chi-\delta)] + \frac{1}{2}\sum_{impropers} K_\varphi(\varphi-\varphi_o)^2 + \sum_{nonbondspairs} \varepsilon_{ij}\left[\left(\frac{\sigma_{ij}}{r_{ij}}\right)^{12} - \left(\frac{\sigma_{ij}}{r_{ij}}\right)^{6}\right] + \frac{q_i q_j}{4\pi\varepsilon_o r_{ij}} \quad (1)$$

where R is the coordinates of the atoms; K_b, K_θ, K_χ, K_ϕ, are the bond, angle, dihedral angle, improper dihedral angle force constants, respectively; b, θ, χ, ϕ, are the bond length, bond angle, dihedral angle and improper torsion angle, respectively; the subscript zero representing the equilibrium values for the individual terms. Lennard-Jones 6-12 and Coulomb terms contribute to the external or nonbonded interactions; ε_{ij} is the Lennards-Jones well depth and σ_{ij} is the distance at the Lennard-Jones minimum between atoms i and j, q_i is the partial atomic charge, ε_o is the dielectric constant, and r_{ij} is the distance between atoms i and j.

Different sets of parameters for empirical potential energy function have been developed for proteins (CHARMM, GROMOS, AMBER, etc.) [117-119] and for hydration water (SPC, TIP3P) [120, 121].

The biomolecule can be partially hydrated by a layer of water molecules just covering the solvent-exposed surface or it can be fully solvated by a large box filled of solvent molecules. In the last case, the whole system is usually replicated in three dimensions and treated with periodic boundary conditions [122]. To save computational time, a variety of approximate methods for the treatment of electrostatic long range interactions have been developed [123, 124]. Given an initial set of atomic coordinates and velocities, a numerical integration of equations of motions is performed [125] by keeping constant the energy constant (NVE ensemble), the temperature (NVT ensemble) or both pressure and temperature constant (NPT ensemble) [122].

From MD simulated trajectories, a variety of quantities can be calculated and compared with the corresponding experimental values; e.g. Raman spectra, incoherent neutron scattering data etc. Additionally, once the reliability of the simulation has been assessed, the MD simulation capabilities can be exploited to extract information which cannot be directly obtained from experimental data

2.5.1 MD Simulations: Technical Details and Stability of the Trajectories

The MD simulations of proteins immobilized onto a gold substrate have been performed with CHARMM version c28b using PARM27 all-atom parameter set [117].

To model the Au(111) surface, the gold atoms have been arranged hexagonally into a cluster of three layers each one with 22x25 atoms; the charge of the gold atoms has been set to zero. The nearest neighbour distance has been assumed to be 2.88 Å and the positions of the gold atoms have been kept fixed during all the simulations.

Initial coordinates of AZ have been taken from the X-ray structure at 0.193 nm resolution (AZU4, entry of Brookhaven Protein Data Bank) [126]. The copper ion has been bound to three ligands (two nitrogens from His46 and His117, respectively, and one sulfur from Cys112), while the much weaker interactions of copper with the sulfur from Met121 and carbonyl oxygen from Gly45 have been treated by a nonbonded approach [127]. AZ has been covalently bound to the gold surface, without breaking of the Cys3 and Cys26 disulphide bridge.

Initial coordinates of PCSS have been taken from the X-ray structure, at 0.160 nm resolution, of the mutant poplar PC bearing a disulphide bridge introduced by replacing Ile21 and Glu25 by two cysteines (1JXG entry of Brookhaven Protein Data Bank) [128]. The copper ion has been bound to three ligands (two nitrogens from His37 and His87, respectively, and one sulfur from Cys84), while the much weaker interaction of copper with the sulfur from Met92 has been treated by a nonbonded approach, according to previous works [52, 129].

PCSS has been covalently bound to the gold surface, after the breaking of the disulphide bridge, by involving one or both the sulfur atoms of the engineered S-S bridge. For the system labeled as PCSS-I, Cys25 sulfur has been assumed to form a covalent bond with the gold substrate; the second sulfur of the bridge having been saturated with a hydrogen atom as in a standard cysteine configuration. In the configuration labeled as PCSS-II, both Cys25 and Cys21 sulfurs have been covalently anchored to the gold substrate.

Initial coordinates of YCC have been taken from the X-ray structure at a 0.123 nm resolution (YCC,entry of Brookhaven Protein Data Bank) [130]. A covalent bond between the heme iron and the sulfur of Met80 is maintained during the simulation. In addition, bonds from Cys 14 and Cys 17 to the porphyrin ring have been added. The S-C bond stretching parameters have been taken to be 240 kcal/mol with an r_o of 1.816 Å and the S-Fe bond stretch has been taken to be 250 kcal/mol with r_o equal to 2.32 Å, according to ref. [131]. With the exception of the metal ligands, all the ionizable residues are assumed to be in their fully charged state, according to the pH value. In all the cases, the sulfur has been bound with 3-fold fcc hollow site gold atoms, placed at the center of the area surface; such a geometrical arrangement having shown to be energetically more favorable [132]. More details about the anchoring procedure are reported in Refs. [51,52].

Starting from the initial structure, each protein molecule, previously adsorbed on gold, has been centered in a cubic box of edge 5.6568 nm and filled with 5832 water molecules equilibrated at 300 K. Any water molecule placed from any protein or gold atom at a distance smaller than 0.280 nm and exceeding a threshold have been removed in order to reach a hydration level corresponding to about 0.4-0.5 g of water per g of protein. For all the systems, the protein charge has been balanced by randomly placed anions or cations to ensure the charge neutrality of the system.

The resulting systems are constituted by 395 water molecules and two sodium ions for AZ, by 303 water molecules and 7 sodium ions for both PCSS-I and PCSS-II and by 338 water molecules and 8 chloride ions for YCC. A schematic representation of the protein adsorbed on the Au(111) substrate and surrounded by water molecules is shown in Fig. 2 for AZ. The parameters used to describe the gold-protein interactions are reported in ref. [51,52].

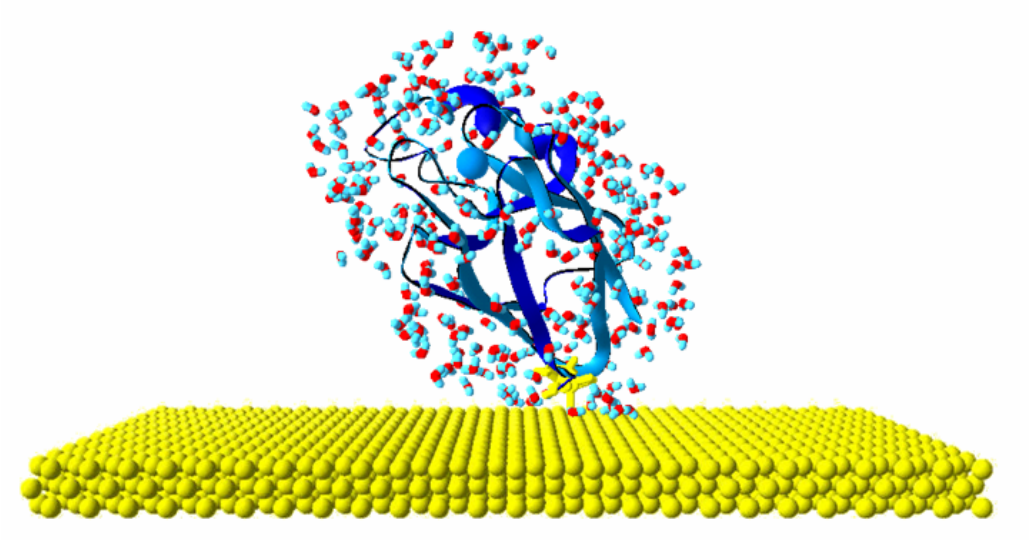

Fig. 2. Graphic representation showing AZ immobilized through the S-S-group on Au(111) substrate, surrounded by 395 water molecules represented by small spheres.

For all the simulations, 2000 steps of minimization followed by a heating procedure from 0 K to 300 K with increments of 5 K every 0.2 ps have been performed. Subsequently, a MD simulation at 300 K has been carried out for 200 ps with a Gaussian velocity reassignment followed by 10 ns of run by sampling trajectories at intervals of 0.1 ps. The Shake constraint algorithm [125] for all hydrogens and cut off ratios of 11 and 13 Å for the Lennard-Jones and the electrostatic energy functions, respectively have been used. The MD simulations have been conducted at constant temperature of 300 K using the Nose-Hoover method [133,134].

To assess the protein-gold systems have properly equilibrated, a number of properties have been first analyzed. In Table I, the mean values, and the standard deviations, averaged over 10 ns of run, of the root mean square deviations (RMSD), from the starting structure, the gyration ratio, R_g, of the macromolecule, are reported for AZ, PCSS-I, PCSS-II and YCC, immobilized on gold. For comparison the values corresponding to the same protein system not bound to gold, are also reported.

For all the protein systems, the gyration ratio R_g values of the bound and the free proteins result to be quite similar (see values in Table I). This is generally indicative of the fact that the overall protein organization, during the dynamical evolution, is not substantially modified by the anchoring to the gold surface.

Table I. Average values and standard deviations of RMSD, from a time interval of 10 ns of MD simulated trajectories for AZ, PCSS-I, PCSS-II and YCC immobilized onto a gold substrate. In parentheses, the values as obtained, by the same simulation procedures, for proteins not bound to gold.

	RMSD (nm) **Gold-adsorbed (free)**	**R_g (nm)** **Gold-adsorbed (free)**
AZ	**0.085±0.003 (0.108±0.008)**	**1.385±0.005 (1.384±0.005)**
PCSSI	**0.078±0.004 (0.115±0.007)**	**1.250±0.001 (1.240 ±0.004)**
PCSSII	**0.084±0.003 (0.115±0.007)**	**1.232±0.001 (1.240 ±0.004)**
YCC	**0.111±0.002 (0.221±0.011)**	**1.275±0.002 (1.278±0.004)**

Concerning the RMSD, we note a reduction in the values of both the average and the standard deviation for all the gold-adsorbed systems in comparison to those of the free proteins.

This can be interpreted in terms of a reduced capability of the protein to explore, during its dynamical evolution, the different substates, local minima of the potential energy hypersurface.

The reliability of the simulations has been further assessed by monitoring the energies during the dynamics. After a short initial time, the potential energies show fast-small amplitude oscillations around a constant value, similarly to what observed for the fully hydrated wild type PC [51, 52, 129].

In summary, the overall properties of AZ, PCSS-I, PCSS-II and YCC result to be only slightly affected by the anchoring to the gold substrate.

2.6 Sample Preparation

AZ from Pseudomonas aeruginosa was purchased from Sigma and used without further purification. The protein was diluted in 50 mM NH_4Ac buffer solution, pH 4.6 at a final concentration of 3.5 μM. At this pH value the protein is stable and approximately neutral, therefore little exposed to double layer effects. The solution purity was checked by measuring the ratio A_{628}/A_{280} (where A_λ is the absorbance at λ nm) by using a Jasco V-550 UV/visibile spectrophotometer. The measured value (A_{628}/A_{280} = 0.607) was in accordance with literature values of 0.53-0.58 [135].

The PC mutants were constructed according to the strategy described into details elsewhere [44, 50]. Sample purity was verified by SDS-PAGE and an isoelectric focusing gel (PhastGel IEF 3-9 Pharmacia). The identity and integrity of PCSS and PCSH was confirmed by using N-terminal sequencing and mass spectroscopy. The N-terminal sequence and mass (by Electron Spray Mass spectroscopy) were determined at the protein sequencing facility, LUMC, Leiden. In the mass spectra a dominant form, corresponding to a PCSH glutathione extension, was revealed. The tetrahedral geometry of the copper active site was confirmed by further spectroscopic characterization carried out by UV-Vis. (Jasco V-550), Resonance Raman spectroscopy (Dilor LaBram (ISA)) and Electron Paramagnetic Resonance (X-band Varian E109 spectrometer) [44]. For substrate incubation, solutions 20 mM sodium phosphate, pH 6.0, with final protein concentration ranging between 7 and 20 μM were used.

YCC, purchased from Sigma Chemical Co., was used without further purification and dissolved in 1mM Tris buffer (pH 8.0) to a concentration of 2.6 μM. The solutions were prepared with ultrapure water (resistivity 18.2 MΩcm). The protein solution exhibited typical UV/Vis absorption spectrum comparable with data from literature [136], and indicative of both reduced and oxidized forms, in agreement with supplier specifics.

The substrates (from Arrandee®) consist of vacuum evaporated thin gold films (thickness 200 nm) on borosilicate glass. For SPM experiments the Au-glass substrates have been flame-annealed prior to incubation, in order to obtain recrystallized Au(111) terraces. The quality of the annealed gold surface was assessed by STM and contact AFM measurements, which showed the presence of atomically flat (111) terraces, over hundreds of nanometers, with typical roughness of about 0.1-0.05 nm.

The annealed Au(111) substrates were directly incubated with the protein solutions at 4 ˚C for times ranging between 30 min and a few hours. After incubation, samples were gently rinsed with buffer solution to remove any unadsorbed material and immediately immersed in buffer solution for fluid imaging. As a control, Au(111) substrates were treated in similar way using only the buffer solutions, without the addition of proteins, to rule out possible spurious images due to buffer effects.

For CV experiments the gold evaporated substrates from Arrandee were cleaned, before incubation with protein solution, by oxidative-reductive cycling treatment in an electrochemical cell containing 1 M H_2SO_4 [137]. The electrode potential was cycled from -0.7 V to 1.5 V vs. Saturated Calomel Electrode (SCE) reference. During this treatment the top gold surface of the electrode is dissolved and re-deposited so as a fresh layer of poly crystal gold is obtained.

3 Azurin on Au(111) Electrodes

The presence of stable AZ monolayer adsorbed on Au(111) substrates via the disulfide group on the protein surface, with the copper center facing the solution, has been demonstrated by XPS, capacitance and in situ STM experiments [38]. Despite the stable adsorption on gold, retention of redox function of adsorbed AZ has been widely debated in the past [39, 48]. Indeed, since the disulfide bond is an integral part of the protein structure, and presumably dissociate upon adsorption, the retention of the 'native' protein structure may accordingly be questioned. More recently, differential pulse voltammetry experiments [138] as well as CV measurements [54] have provided evidence of the functionality of AZ adsorbed on gold electrodes.

Here, AZ molecules adsorbed on gold electrodes have been investigated by the combination of several techniques and their behaviour is compared with that of other adsorbed metalloproteins.

3.1 Morphological Characterization

An accurate morphological characterisation of the adsorbed proteins has been achieved by the combination of STM and AFM experiments.

A systematic analysis in TMAFM has allowed us to gain deeper insight in topological properties of adsorbed proteins, especially in terms of their height and orientation with respect to the gold substrate. Indeed, lateral forces exerted on the proteins by the scanning tip are significantly reduced in TMAFM, if compared to contact mode, thus minimizing both damaging and indentation of the sample by the tip. Moreover, in order to eliminate capillary forces, which may produce artifacts [93], TMAFM images have been recorded in fluid.

Several TMAFM images were recorded from different zones of the adsorbed gold substrates under buffer solution. In Fig. 3 the TMAFM image of an immobilized AZ monolayer on Au(111) substrate, as obtained after overnight incubation, is shown. The molecules are uniformly distributed over the gold surface and display homogeneous lateral and vertical dimension, with no evidence of aggregates. The proteins appear stably bound to gold, producing high quality images even after repeated scans. Higher resolution images of adsorbed single molecules have been obtained on substrates displaying lower concentration of AZ, resulting from shorter incubation times (1 hour max) (Fig. 4). In such samples, individual molecules are well resolved above the substrate, so that height evaluation can be obtained with high resolution (~0.1 nm), by single molecule cross section analysis.

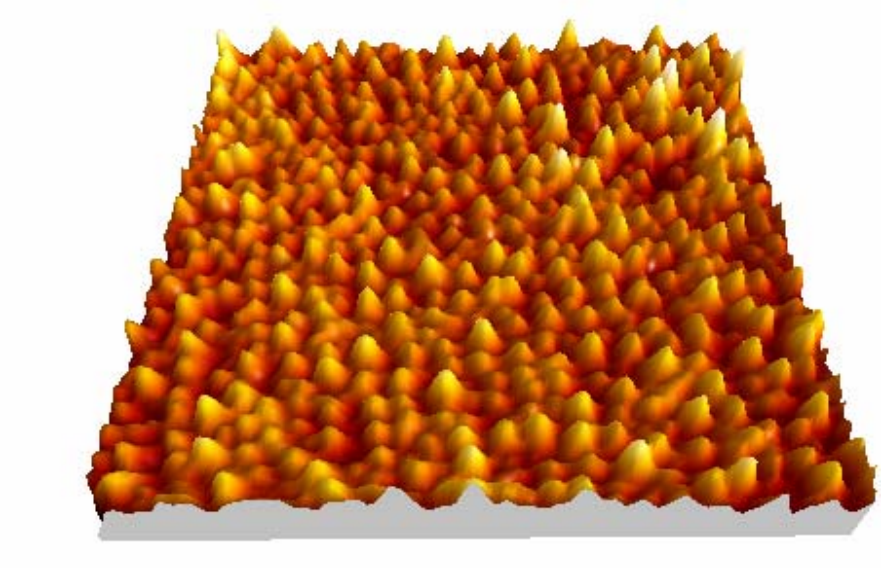

Fig. 3. TMAFM image of an AZ monolayer on Au(111) surface, recorded in buffer solution. Image size: 550 x 550nm; z range 5 nm.

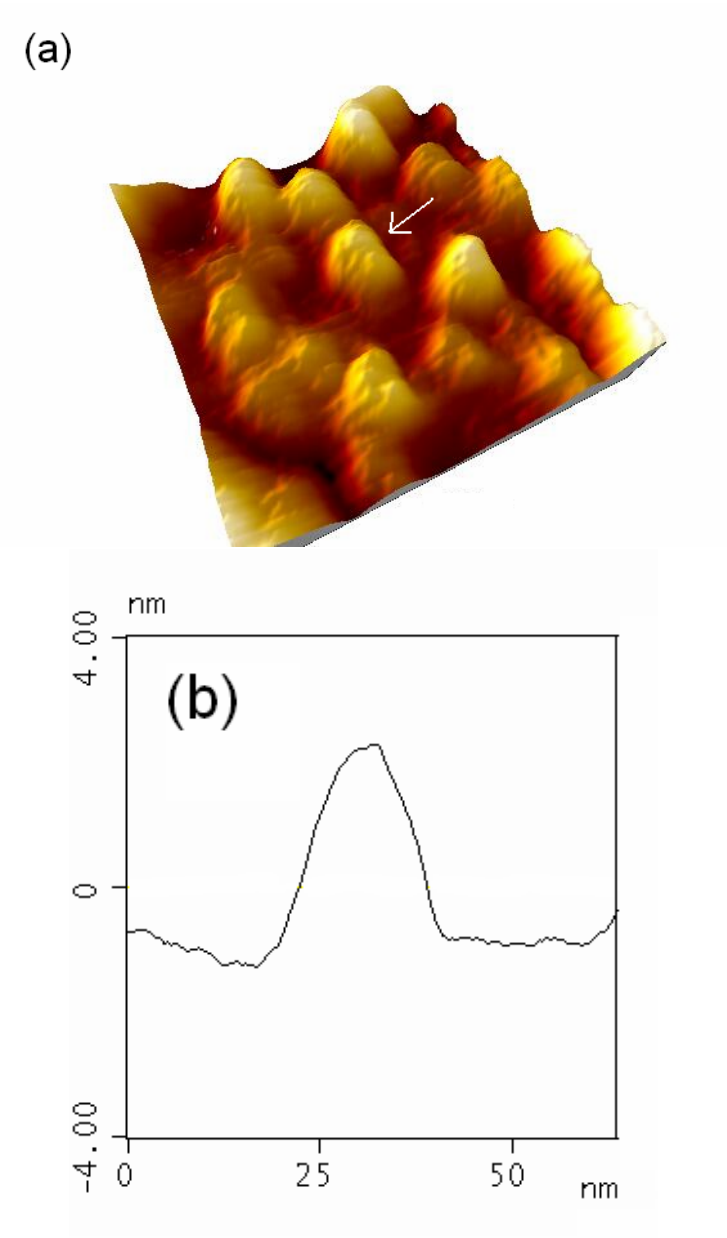

Fig. 4. (a) Representative TMAFM image of AZ single molecules adsorbed on Au(111) surface, recorded in buffer solution. Image size: 130 nm x130 nm, z range: 5 nm; (b) cross section profile as recorded for the molecule indicated with the white arrow.

The statistical distribution of the AZ vertical size above the Au(111) surface provides information not only about the mean vertical dimension of the immobilized protein but also on its flexibility over the gold substrate. Results from cross section analysis on more than 800 different molecules are summarised in the histogram of Fig. 5. The height distribution is centered around a mean value of 1.7 nm, a bit lower than the expected value as obtained by x-

ray crystallography [126] (4.4 nm x 3.3 nm x 3.0 nm), and also lower than estimated vertical size (~ 3 nm) for topological arrangement of the protein immobilized on gold via the disulfide bridge (see Fig. 1(a)). This finding is somehow resembling the results obtained by other groups [42] which reported a possible denaturation for adsorbed proteins, corresponding to a low-height form of AZ (h < 1.7 nm) for 50% of imaged molecules. Even if we do not find the double peak distribution shown by these authors, the population of molecules with h < 1.7 nm results to be about 60 %, namely comparable to the denatured population found by Davis. However, the standard deviation of 0.6 nm, reflecting some heterogeneity in protein dimension, may be also connected to protein flexibility and possible reorientation on the substrate.

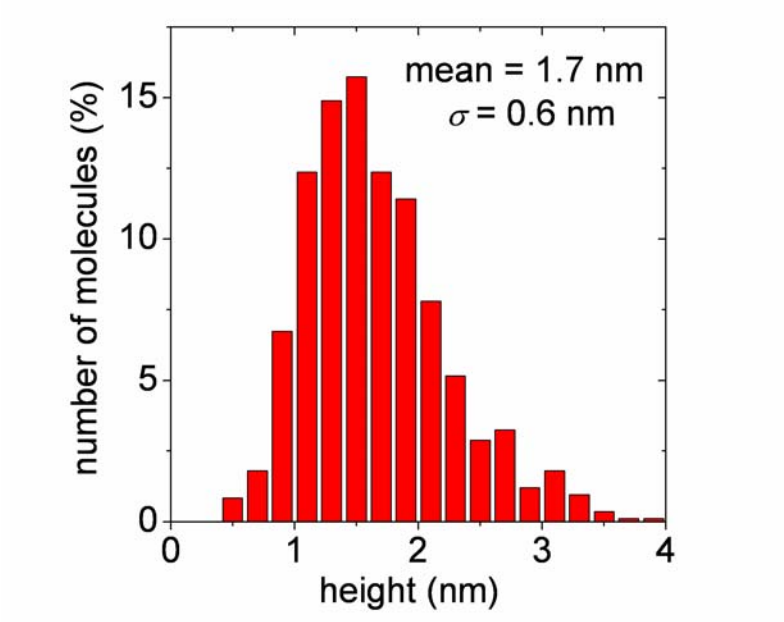

Fig. 5. Statistical analysis of AZ molecular height on the Au(111) surface, measured by TMAFM in buffer solution. Data are obtained from individual cross section profiles over 832 molecules.

Minor information can be obtained, by AFM, about lateral dimensions of the proteins. In fact, the relatively large size of the tip and its geometry induces broadening effects in the biomolecule images [139]. The measured lateral dimensions of the protein can be up to five times larger than expected from crystallographic data, so that the lateral dimension should be evaluated by deconvolution of the image with the tip shape. The typical protein lateral dimension, as evaluated from full width at half maximum of molecule cross section profile (see Fig. 4 (b)), is in the range 20-30 nm, considerably larger than the crystallographic data [126]. An estimate of the true lateral size of an imaged object can be obtained as follows [140]: for a spherical object and a tip of radius of curvature r, the real diameter *d* can be estimated by the relation $d = W^2/8\ r$, where W is the measured apparent width. In our experiment the nominal tip radius is 20 nm and the average apparent width 25 nm, so that we obtain for the lateral size of the adsorbed AZ the value d=3.9 nm, which is close to crystallographic data.

The protein lateral dimension can be generally recovered by STM imaging [40, 42, 67], which is known to induce a minor tip convolution respect to AFM, often revealing interesting submolecular features [37, 68].

Therefore, adsorbed AZ molecules have been imaged by STM in buffer solution. A typical STM image recorded in air from a sample incubated for about one hour with the protein solution is shown in Fig. 6. Single AZ molecules are well resolved above the Au(111) substrate. The high quality of the image, even after repetitive scans, is in agreement with stable adsorption of the proteins over the substrate, as for covalent binding. An estimate of the molecule lateral size can be obtained by cross section analysis. The mean protein diameter, evaluated from the full width at half maximum, is in the range 3-4 nm, namely in agreement with crystallographic size of AZ [126]. Nevertheless, the height of the molecule over the substrate is about 0.5 nm, significantly smaller than that crystallographic size, and even smaller than the value measured by TMAFM. The considerable height reduction of biological materials in STM imaging was already observed in numerous previous investigations [38, 40, 41, 64, 141] and only in few cases the physical height of the biomolecules has been reported [142, 143]. Such a discrepancy is still a controversial aspect in the interpretation of STM images. Although a number of groups have reported successful STM imaging of biomolecules, the imaging mechanisms of molecular adsorbates [144, 145] and correlation between contrast and physical shape of bio-molecules [146] are not fully understood. It has been proposed that the STM contrast of organic adsorbates on metallic surface arises from modification of the metallic states at the Fermi energy caused by the interaction of the molecules with the metal surface [147]. Experiments performed in ambient atmosphere on DNA pointed out that the presence of water around the bio-molecules and above the substrate may generate an ionic conductivity, which plays an important role in tunnelling between STM tip and sample surface [148, 149]. Moreover, for high vacuum STM of biological molecules, an electric field-induced mechanism for conduction of electrons through the molecule was suggested [142]. In the case of a metalloprotein, the redox centre was proposed to mediate the tunnelling current [37, 66]. This has been interpreted in the framework of two theoretical models. One model takes into account the effect of the coupling between adsorbate redox levels and the substrate Fermi level. In this model [66], electrons tunnel from tip to substrate (or vice-versa) by a resonant tunnelling process through the molecular unoccupied states (oxidised states) when they are brought to align with the substrate or tip Fermi level. In a second model a strong coupling of molecular electronic states with the nuclear fluctuations is considered. In this case the electron transfers to the protein and reduces the copper site, which begins to relax vibrationally; this relaxation allows the molecule to transfer the electron to the other electrode and to return to its oxidised state [37, 150]. Even if the physical mechanism governing the STM process through a biomolecule has not been fully established, it is commonly accepted that STM images are a complex convolution of topographic and electronic contributions; therefore the height of biomolecule as measured by STM may deviate significantly from the purely topographic one, being normally underestimated.

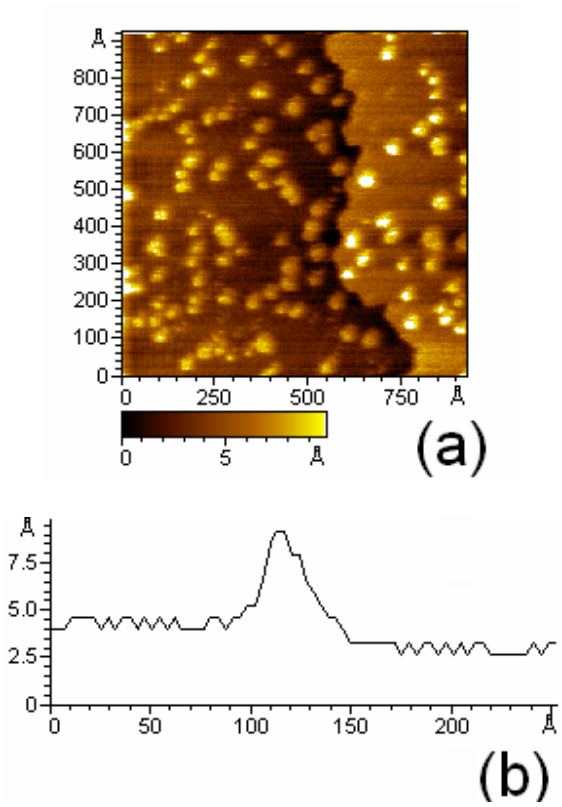

Fig. 6. STM image of AZ molecules adsorbed on Au(111) recorded in buffer solution (a) with representative cross section profile (b). Tunnelling current: 2 nA; bias voltage: 400 mV; substrate potential +25 mV vs SCE.

3.2 Conduction of Adsorbed Molecules

Electrical properties of AZ monolayer self-assembled on gold were investigated by STS. Single current – voltage spectra were recorded at room temperature in air. After positioning the scanning tip at a pre-set tunnelling distance, as defined by the choice of the tunnelling resistance, the feedback was disengaged and the current recorded, while the bias was sweeping within ±1 V. Fig. 7 shows typical current – voltage characteristics obtained on AZ monolayers by local STS at two different starting tunnelling current which implies different tip/bio-molecule tunnelling distances. The two I-V plots appear to be quite different. In particular, the bio-molecular junction shows an electrical response highly asymmetric, when I-V were recorded at starting tunnelling currents of 10 pA. The rectifying properties of the metal/AZ/metal tunnelling junction are still evident, but quite reduced in intensity, when the tunnelling current is increased to 50 pA. This effect is possibly due to the fact that the local tip/bio-molecule interaction has been changed. Because of the exponential dependence of current on the tunnelling distance, even a small increase in tunnelling current can lead to a huge reduction of the width of the tunnelling gap, and consequently the local pressure exercised by the STM probe should increase.

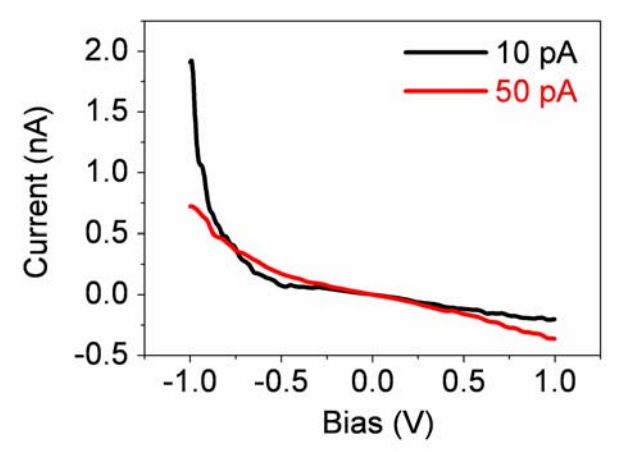

Fig. 7. I-V characteristics of AZ monolayer on Au(111) substrate recorded by STM at a starting tunnelling current of 50 pA (red curve) and 10 pA (black curve).

Some explanations might be invoked to explain the observed I-V asymmetry. In connection with the theories describing the electron tunnelling through a redox molecule, the copper site immersed in the protein matrix may play a role in generating the I-V asymmetry [66, 150]. This, indeed, has been already reported in STS experiments on electroactive molecules [67, 147, 151-153].

On the other hand, I-V asymmetry is a characteristic of a rectifying-like behaviour. Earlier models developed by Aviram and Ratner describe molecular rectification for a metal-insulator-metal junction with an organic molecule, containing a donor-acceptor pair, placed between the metal electrodes [154, 155]. Alternatively, rectification was attributed to the presence of a single electron acceptor asymmetrically placed in a metal-insulator-metal junction [156], or to conformational changes driven by the external electric field [157], or even to Schottky barrier effects [158].

Therefore, it is clear that molecular rectification is not an unambiguously resolved process and its mechanism is currently under investigation.

In our case, it is worth stressing that pressure is known to affect the tunnelling current [159] and the change from asymmetric characteristic to a symmetric one may be likely due to either variations of the gap width between the tip and the protein or to different tip to molecule local pressure.

On the basis of these results, quantifying the tip to substrate distance appears to be a fundamental requirement to investigate the biomolecular conductance by STS [67, 68].

To overcome the limitations of the STS measurements and investigate more accurately the electrical junction properties also as function of the applied pressure, conducting AFM (CAFM) was employed. In such methodology forces, and not current, were used to control the feedback, and the AFM tip can be controllably positioned in contact with the protein monolayer.

To form a bi-terminal junction, the wild type form of AZ was immobilized on bare Au(111) substrates via its exposed disulfide moiety, being a metal coated AFM probe used as second electrode. In order to minimize any contribution to the current signal from the water molecules surrounding the bio-molecules, the relative humidity was controlled and reduced

by purging the measuring chamber with nitrogen. To avoid any damaging of the metal coating at the tip and possible contamination, the monolayer of AZ on gold was electrically investigated by local I-V spectroscopy. An example is shown in Fig. 8. I-V characteristics for the metal/AZ/metal junction were recorded between ±1 V at applied forces ranging from 2 nN to 14 nN. All curves appear sigmoidal in shape and well reproducible. Slight asymmetry was observed, especially when the bio-molecules were only gently compressed (2-4 nN). For justifying the asymmetry in I-V responses, in addition to explanations previously discussed, we may consider that the position of the copper ion in the bio-molecule is non symmetric with respect to both metal terminals of the junction. Moreover, while AZ molecules are covalently linked to the substrate, the AFM probe is in physical contact with the bio-molecules, and the specificity of the chemical contact is known to cause a different efficiency in current transmission.

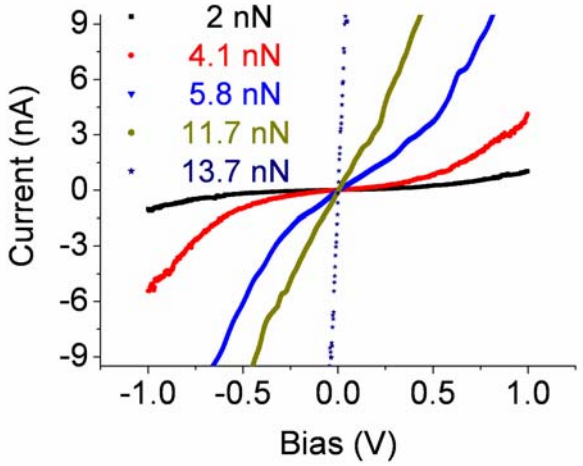

Fig. 8. I-V characteristics recorded by CAFM on a monolayer of AZ chemisorbed on Au(111) substrate at increasing applied forces, from 2 nN (black symbols) to 13.7 nN (dark blue symbols).

A well defined ohmic region was observed within ± 0.3 V, as shown in Fig. 9. The linear current-bias dependence yields information on the resistance of the metal/AZ/metal junction. By the slope of the I-V plots in the ohmic region, the resistance was studied as a function of the force exercised by the AFM probe. Fig. 10 shows the typical response obtained on a monolayer of AZ molecules included between the Au(111) substrate and the gold coated tip. The resistance is monotonically decreasing as the force is lowered with an exponential dependence on the applied force. A very similar dependence was observed for the current flowing through the bio-molecule *versus* the applied force, when force-distance curve and current signal were recorded simultaneously at a fixed bias. In Fig. 11 applied forces and current flowing through the junction are represented as a function of the piezo actuator position. No current was observed to flow below 7 nN of applied force, being this consistent with the presence of a contact resistance at the tip/protein interface. Afterwards, the current increases almost exponentially until saturating the pre-amplifier.

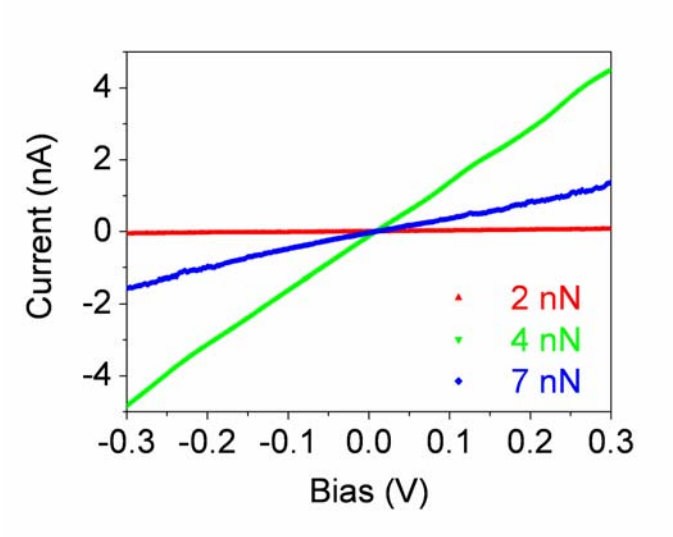

Fig. 9. I-V characteristics recorded by CAFM on a monolayer of AZ chemisorbed on Au(111) substrate at increasing applied forces: ohmic region.

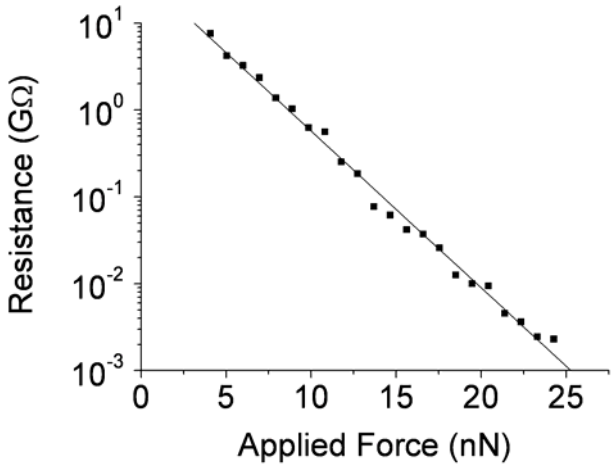

Fig. 10. Semi logarithmic plot of resistance vs applied force for a monolayer of AZ on Au(111) substrate in nitrogen atmosphere.

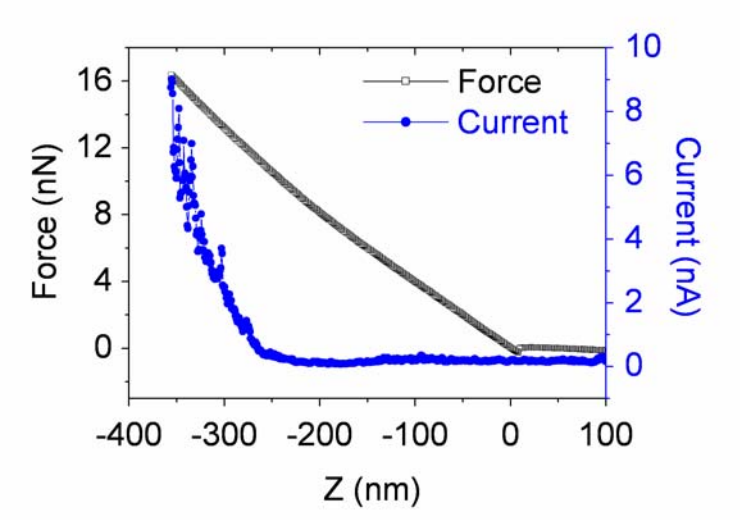

Fig. 11. Current/force vs piezo displacement as recorded by CAFM on an AZ monolayer; bias applied: +1 V.

Both experiments summarized in Figs. 10 and 11 were in agreement with what recently observed on the same protein by CAFM [104]. The transport mechanism was assumed to be dominated by electron tunnelling through AZ protein, since the protein is mechanically compressible and therefore the width of the tunnelling barrier may be modulated by varying the applied forces.

3.3 Functionality and Redox Activity of Adsorbed Molecules

Cyclic Voltammetry

Preserving natural ET properties up on immobilization on a metal electrode is a key requirement toward the integration of a bio-molecule in bioelectronic devices. CV is a consolidated electrochemical technique that allows probing ET reaction at a solid/electrolyte interface.

To perform CV experiments, poly-crystalline gold electrodes fully covered with AZ molecules were assembled in a small volume (2 ml) electrochemical cell, subsequently filled with 50 mM sodium phosphate solution at pH 4.6. The typical cyclic voltammogram, as recorded at 50 mV/s, is shown in Fig. 12. From these data, a redox midpoint of +120 mV_{SCE} was estimated, consistent with the data for AZ solution [160]. The marked depression of the anodic peak, along with the rather large peak separation (160 mV) seems to point out the involvement of a mechanism of slow ET that has already been reported for this protein [37]. These data thus indicate the presence of redox-active AZ molecules on the surface of the gold electrode. In addition, from the current consumed to oxidize the redox protein, a 90% of surface coverage was estimated.

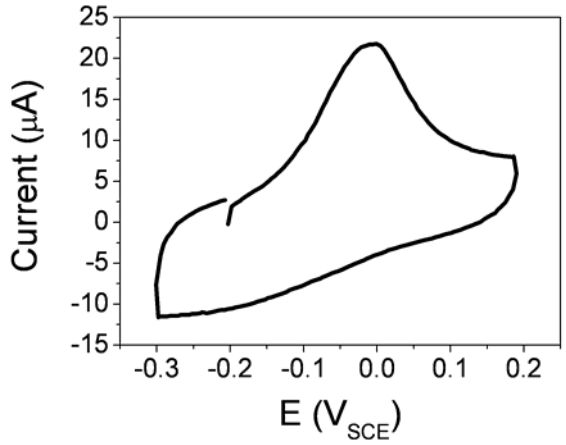

Fig. 12. Cyclic voltammogram of AZ on Au(111) electrode; data are recorded in NH4Ac 50 mM, pH 4.6, T = 25 ºC. Redox mid point +120 mV_{SCE}, peak separation 160 mV, sweeping rate 50 mV/s.

As shown in Fig. 13, the analysis of the increment in current at the anodic and cathodic peaks revealed a linear dependence on the scan rate. This result is a typical feature for an electro-active species, permanently confined at the solid/electrolyte interface (for a diffusion-limited process a dependence on the square root of the scan rate is instead expected) thus indicating that AZ molecules were stably immobilized on the gold electrode and were preserving their ET capability.

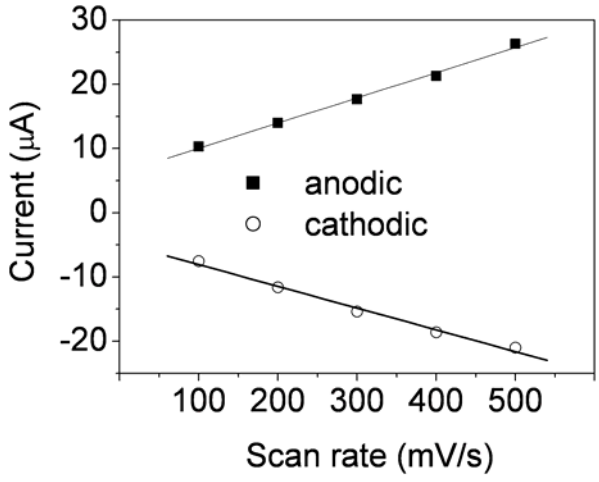

Fig. 13. Anodic (filled squares) and cathodic (open circles) peak current vs. voltage scan rate, as measured from cyclic voltammograms.

In situ ECSTM

In an effort to correlate the amount of current transmitted through AZ from/to the metal substrate, in situ STM was performed under full electrochemical control provided by a bipotentiostat, which enables to control separately the electrochemical potential of the two working electrodes involved in the measurements (substrate and tip). This condition offers the possibility to tune the electrochemical potential of the working electrodes to the protein redox midpoint potential [37, 39, 40] allowing the investigation of image contrast in relation to the ET properties of the molecule.

We have carried out a parallel STM-AFM experiment under electrochemical control, i.e. by imaging the samples in a wide range of the substrate potential. Fig. 14 shows representative AFM (upper set) and STM (lower set) images acquired at -200 and +80 mV, i.e. on the negative side of the redox midpoint of AZ [160] (+116mV vs SCE) and in a potential range where the Au(111) surface structure is still unaffected by the buffer ion adsorption [161]. While the AFM images show the spots corresponding to AZ adsorbates in the whole set of potential values investigated, albeit a certain drift due to recurrent scans, the STM data look completely different. In fact the typical STM bright spots, which are repeatedly seen when tuning the substrate potential to the proper region, now appear to be strongly potential-dependent.

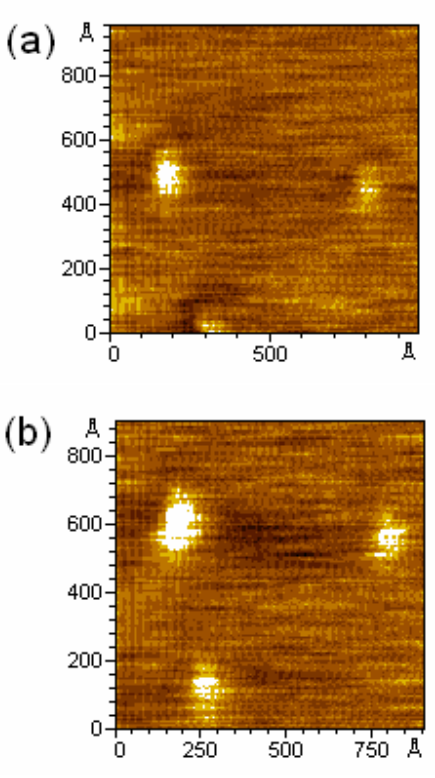

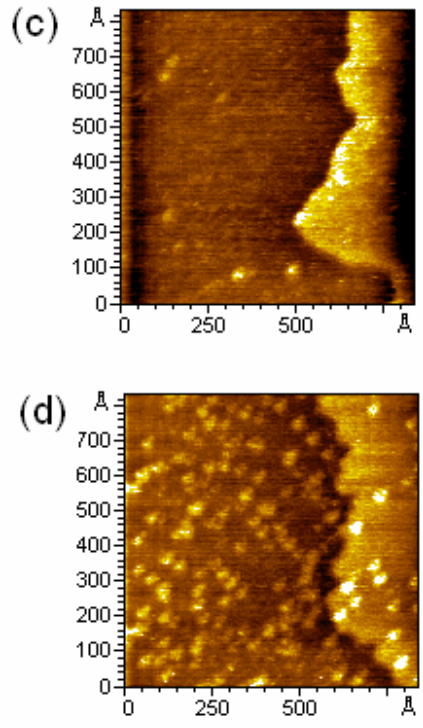

Fig. 14. Upper set, in situ AFM images of AZ recorded at -200 mV (a) and +80 mV (b) vs. SCE in contact mode. Vertical range, 1 nm. Scan rate, 4 Hz. Lower set, in situ STM images of AZ recorded at -200 mV (c), -and +80 mV (d) vs. SCE (tunnelling current, 2 nA; bias, 400 mV tip positive).

Therefore, the topographic AFM images are not affected by changes in the electrochemical potential of the substrate, whereas STM images appear to be unambiguously dependent on tuning its value to that of the AZ redox midpoint. Such behaviour discloses the resonant nature of the current measured in STM experiments in gold-adsorbed AZ samples. Tunnelling appears to take place via the protein redox level once the substrate potential is properly tuned to it.

The limitations imposed by the particular experimental system do not allow us following the dependence of the current intensity on the electrochemical potential also for more positive substrate values (resonance profile), overcoming the equilibrium potential of AZ and eventually monitoring the corresponding potential de-tuning. In fact, likely due to buffer ion adsorption on Au surface and the consequent lift of the reconstruction, more positive potential values do not allow for molecular resolution; rather, they result in an adlayer formation which stacks up as the potential is increased. The only consideration that can be done is that the estimated width of the resonance profile seems to be consistent with a width of about 300 mV, which corresponds to the value observed also in the experiment of Tao in case of Fe(III)-protoporphyrins IX [162] and similarly appears to be underestimated with respect to the predictions of Marcus' ET theory [163].

Interestingly, we note that, as far as the potential remains in the aforementioned range, it is possible to step back and forth its value and switch accordingly on and off the visible spots.

Fig. 15 reports such an example, in which the potential is stepped by 100 mV to a more negative value (from -25 to -125 mV) and then is tuned back to the original value. The molecular features, clearly visible in the first image (a), disappear in the second (b) and reappear only once the potential is re-established (c). It is also remarkable that in the image at -125 mV some darker zones appear in correspondence to the brighter spots in the other two images. These effective depressions are likely to be interpreted in terms of work-function mediated features [60], suggesting once more that when the substrate potential is not tuned to the redox midpoint of AZ, the protein itself cannot elicit a current flow through it; rather, it behaves as an insulating barrier. This evidence is somehow confirmed also by the occurrence of a sort of blurring in Fig. 15 (c), which could be consistently due to the interaction of the tip apex with the protein globule when scanning the surface in de-tuned conditions. However, several imaging cycles can be performed without a drastic loss of resolution.

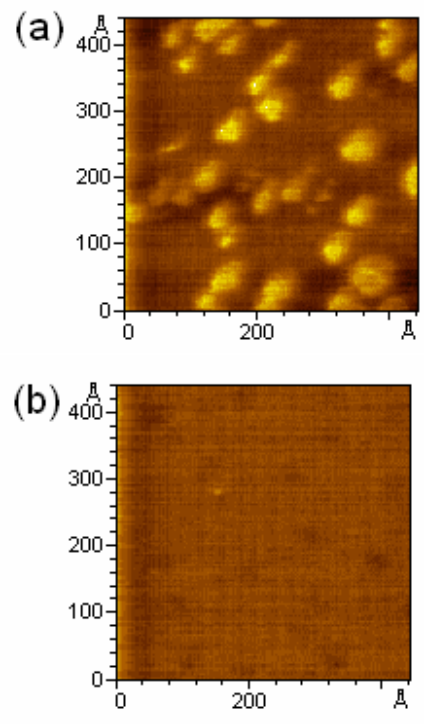

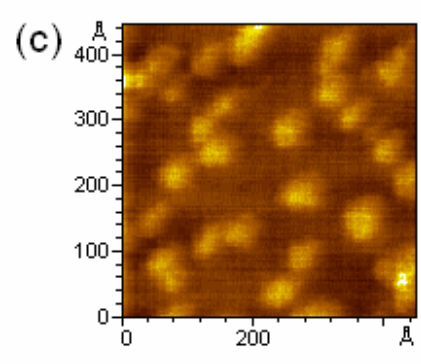

Fig. 15. Sequence of in situ STM images of AZ-adsorbed Au(111) in 50 mM ammonium acetate (pH 4.6) obtained at -25 mV (a), -125 mV (b) and -25 mV (c) vs. SCE. Bias voltage,+400 mV; tunnelling current, 2 nA; vertical range, 1 nm; scan rate 16 Hz.

These data demonstrate that the origin of the bright spots visible when performing in situ STM of gold-adsorbed AZ under electrochemical control is resonant in nature.

3.4 Molecular Dynamics Simulations

Although MD simulations are currently employed to investigate the dynamical properties of proteins also in connection with experimental approaches [164, 165], only a few attempts have been done to describe the chemisorption of proteins on surfaces [166] and to compare MD simulated and AFM experimental data [167]. On such a ground, with aim to investigate the topological organisation and the dynamical response of a protein immobilized on gold, we focus our attention to the dynamical properties of the AZ covalently bound to a gold electrode, with a particular emphasis to those properties related to SPM data.

The root mean square fluctuations (RMSF, $<\Delta r^2>^{1/2}$) averaged on 10 ns, indicative of the mobility of the macromolecule, show a decrease of both the average and the standard deviation, in comparison to the values for AZ not bound to gold (gold-bound AZ: $<\Delta r^2>^{1/2}$ = (0.013± 0.005) nm; free AZ: $<\Delta r^2>^{1/2}$ = (0.05 ± 0.02) nm). Such behaviour reflects that the protein flexibility is significantly reduced when the macromolecule is anchored to a substrate.

To analyze the orientation and the dynamics of AZ, with respect to the gold substrate, the θ and Φ angles, as depicted in Fig. 16, have been analyzed as a function of simulation time: θ is the angle that the axis **p**, joining the sulfur of Cys3 and the copper atom, forms with the normal to the gold surface; Φ is the precession of **p** about the gold surface normal (see inset of Fig. 16). The trend with time of θ and Φ during the MD trajectory, are plotted in Fig. 16. We note that a deviation of **p** from the normal axis is registered with small values for the standard deviation. Such behaviour is indicative of the fact that the position assumed by protein, with respect to the gold substrate, is substantially maintained during the dynamical evolution. This indicates that the presence of the two covalent bonds between the macromolecule and the gold substrate results into a strong anchoring, which prevents large displacements from the starting position.

Concerning the Φ angle, a spread around the average value, similarly to what observed for θ, is detected. Such a behavior suggests that the macromolecule can assume different

lateral positions with respect to the gold surface. In summary, the orientation and the position of AZ with respect to the gold substrate evolve during the MD simulated dynamics.

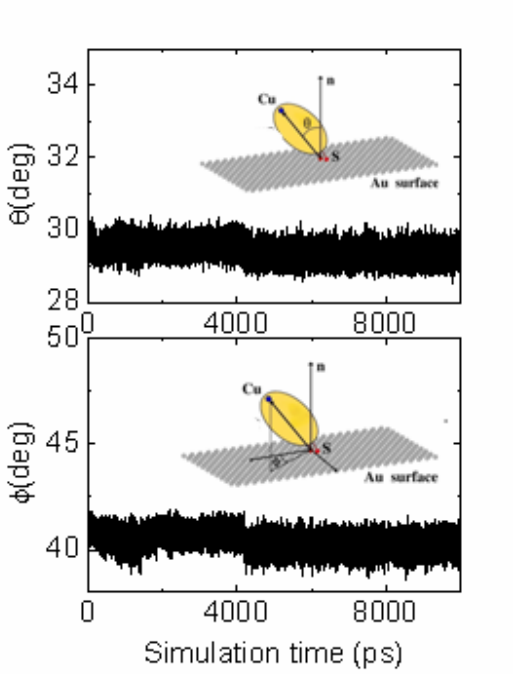

Fig. 16. Temporal evolution, along a 10 ns MD simulated trajectory, of θ and Φ angles describing the orientation and the precession, respectively, of the protein p axis with respect to gold surface normal, for the AZ. The mean value and the standard deviation are (29.5±0.5)° and (41±1)° for θ and Φ, respectively. A description of the θ and Φ angles is also shown.

Generally, these results, suggesting some variability in the arrangement of the protein on gold, provide some hints to interpret the experimental topological and morphological data of immobilized proteins. In this connection, the protein has been represented by an ellipsoid centered at the center of mass of the protein and oriented as its main inertia axes. The ellipsoid, evaluated from the MD simulated trajectories, giving an overall representation of the macromolecule, can thus provide a description of the height of the protein onto gold; such a quantity being appropriate to be compared with that from topological TMAFM data. The ellipsoid and its corresponding height over the gold substrate have been extracted from the MD simulated trajectories by sampling structures every 10 ps. The histogram of the heights, as obtained by 1000 structures, is shown in Fig. 17. From this figure, it comes out that a single mode distribution is registered. The mean values is in substantial agreement with that expected from the crystallographic data by assuming that protein is anchored to gold via the disulphide bridge (h ~ 3 nm). Additionally, the spread around the mean values is indicative of the fact that, during its dynamical evolution, the macromolecule can assume a variety of arrangements, resulting into different heights, with respect to the gold substrate.

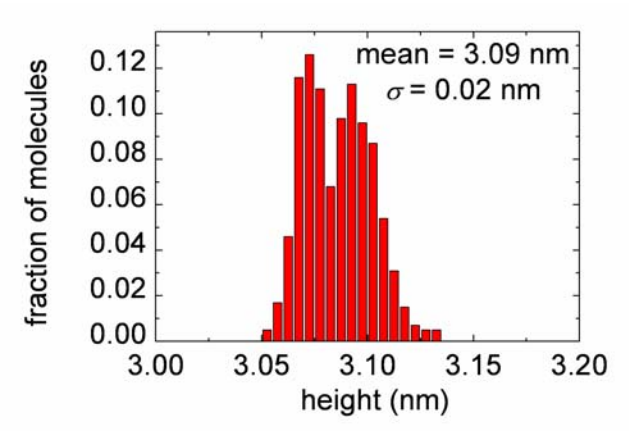

Fig. 17. Statistical analysis of the AZ height above the Au(111) substrate, as extracted from 1000 molecular structures sampled every 10 ps of 10 ns MD simulated trajectories.

By comparing these data with those as derived from TMAFM by analysing 1000 different individual molecules (see Fig. 5), we note that the central value of the TMAFM distribution is drastically reduced with respect to that observed by MD simulation. However, since a partial denaturation of AZ adsorbed on gold likely characterized the experimental samples, as previously suggested, a direct comparison between MD simulated and our TMAFM data cannot be done. Concerning the spread of the distribution, we note that the standard deviation, as derived by TMAFM is larger than that from MD simulated data. Irrespectively of denaturation aspects, we remark that such a result finds a correspondence with what expected by taking into account the stress exerted by the tip on the biomolecule during the AFM measurements. Indeed, even in TMAFM, an interaction between the tip and the biomolecule can occur. Additionally, we remark that TMAFM data refer to a collection of molecules, likely in different starting arrangements, which, moreover, may be anchored to gold by one or both sulfur atoms, whereas MD simulations consider a single molecule by only a way of anchoring.

4 Plastocyanin Mutants on Au(111) Electrodes

To make poplar PC suitable for stable and specific self-assembly onto gold, we designed two mutants bearing anchoring groups that carry sulphur atoms in a region of the protein opposite to the copper active-site [44]. As schematically represented in Fig. 1, the anchoring groups are readily available for chemisorption onto a gold electrode [28], in order to create well-defined molecular adlayers of high stability and, more importantly, to control the electronic coupling between the metalloprotein and the underlying gold electrode. In the first mutant (PCSS), a disulfide bridge is inserted within the protein, while in the second one (PCSH) a residue tail, containing a cysteine, was added as C-terminal extension.

4.1 Morphological Characterization

To characterize the protein morphology, in particular the height and orientation of the macromolecules respect to the gold substrate we performed a systematic analysis by TMAFM and STM. Fig. 18 shows representative topography of PCSS (a) and PCSH (b) molecules adsorbed onto Au (111). Both mutants are homogeneously distributed over the substrate, as confirmed by several images recorded in different zones of the substrates, whereas the high quality of the recorded image, even after repetitive scans, is indicative of a stable binding to gold. Individual molecules are well distinguishable above the substrate, making these samples suitable for statistical analysis of molecule height distribution.

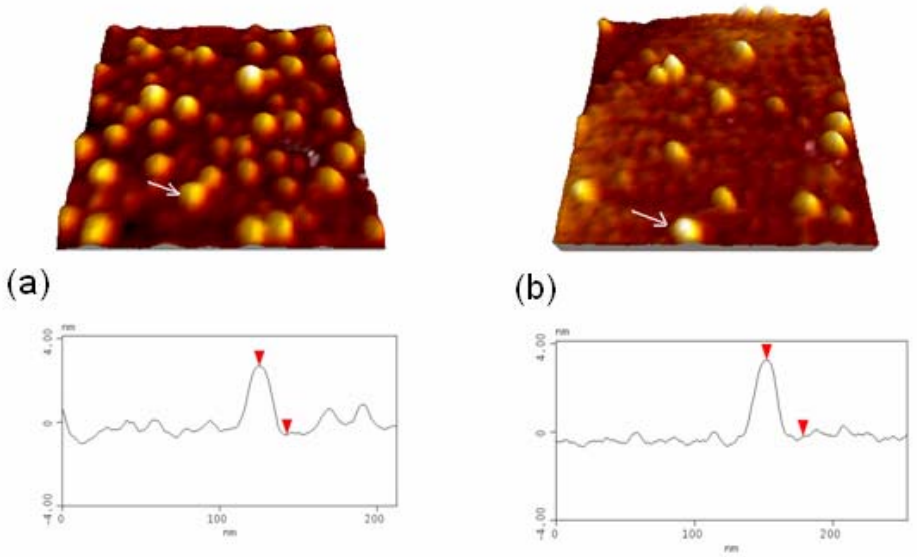

Fig. 18. TMAFM image and representative cross section profile of PCSS (a) and PCSH (b) molecules adsorbed on Au(111), recorded in buffer solution. The cross section profiles are recorded for molecules indicated with white arrows.

The vertical dimension of the PC mutants was estimated from individual cross section analysis, as shown in Fig. 18. Data taken for hundreds of molecules are represented in the histograms of Fig. 19. The monomodal distribution is indicative of a preferential orientation of the adsorbed proteins on the gold substrate. The data for PCSS molecules have a mean value equal to 2.3 nm and a standard deviation of 0.5 nm, whereas for PCSH the mean height is 1.9 nm with a standard deviation of 0.6 nm. With reference to graphical representations of the PC mutants with the anchoring groups assumed to be 'face down' for covalent binding to gold (see Fig. 1 (b), (c)), one expects a vertical size of about 2.8 nm. Therefore, data for PCSS are centred at a value close to the expected value, whereas the vertical dimension of PCSH above the gold substrate slightly differs from this value. The standard deviation, which is in both cases much larger than the experimental error, is indicative of a significant spread in the vertical size of the molecule. Similar values for the standard deviation of the height were found by other groups in TMAFM imaging of various biomolecules [30, 168]. Generally, the

observed spread in the experimental TMAFM data is directly connected to protein flexibility above the substrate. Indeed, if we consider that the tapping frequency is in the kilohertz range, we can expect that even protein movements on the millisecond scale may result in a spread of the measured heights. In addition, a contribution to the observed spread in heights could arise from heterogeneity in the protein arrangement on the substrate. To evaluate if standard deviations of the two sets of data are significantly different, the F-test has been executed, indicating that the standard deviation for the PCSH is higher than that for PCSS data with a confidence level of 95%. This result suggests that the disulfide bridge provides a stricter immobilisation and a more homogeneous orientation of PCSS molecules onto gold compared to PCSH, where the single thiol, external to the main structure, could allow a higher flexibility of the adsorbed proteins.

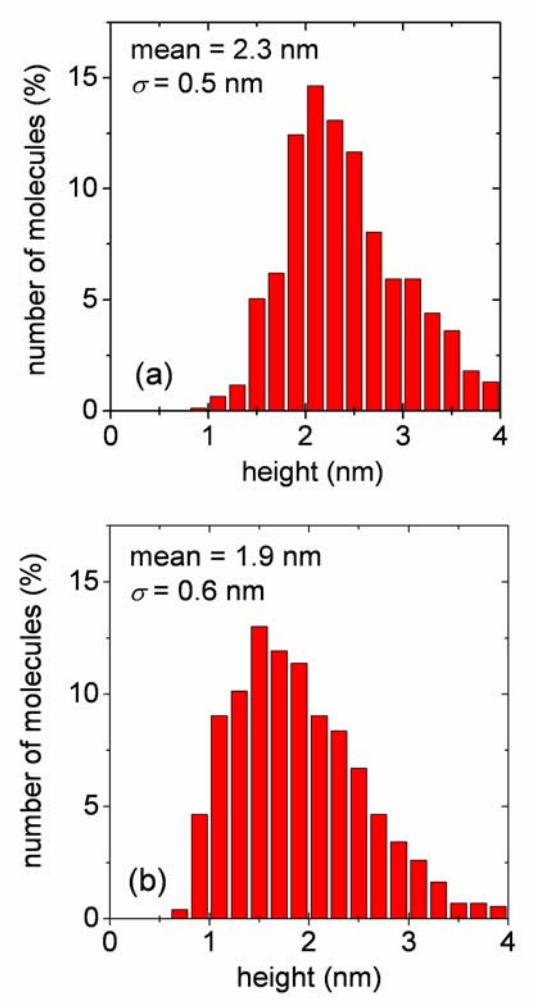

Fig. 19. Statistical analysis of PCSS (a) and PCSH (b) height above the Au(111) substrate, as evaluated from individual cross section profiles over hundreds of molecules (772 for PCSS and 730 for PCSH).

The adsorbed PCSS and PCSH molecules have been also imaged by STM under electrochemical control, air and under nitrogen atmosphere. Similar features and no substantial differences in shape between the two mutants could be observed in the STM images. For both PC mutants, the STM images appear to be stable and reproducible even after repetitive scans, thus confirming a robust binding of the protein molecules to Au(111) substrate. In contrast, analogous STM experiments performed on adsorbed wild type PC (PCWT) revealed protein mobility over the substrate upon repeating scans, which indicates that no stable binding occurs for PC in the absence of S-S or S-H groups (data not shown). Some representative STM images are shown in Fig. 20 for PCSS on Au(111) under various experimental conditions. Independently of the imaging conditions (fluid, air and controlled atmosphere), single molecules showing similar features are clearly discernible on the gold substrate. The lateral dimension of these single molecules well agrees with the crystallographic values of PCSS showing a diameter of about 4.0 nm [128]. The vertical size of PCSS and PCSH is ranging between 0.5-0.7 nm, as measured by the tip retraction along the z axis and shown in the cross section profile of Fig. 20. Even in this case, as previously observed for AZ and for most of the biomolecules imaged by STM [41, 64], the vertical size appears to be underestimated and significantly smaller than the expected value. This recurrent characteristic of the STM images on biological material has drawn our attention, specifically on the possibility that the tip may interfere with the soft biological sample during scans.

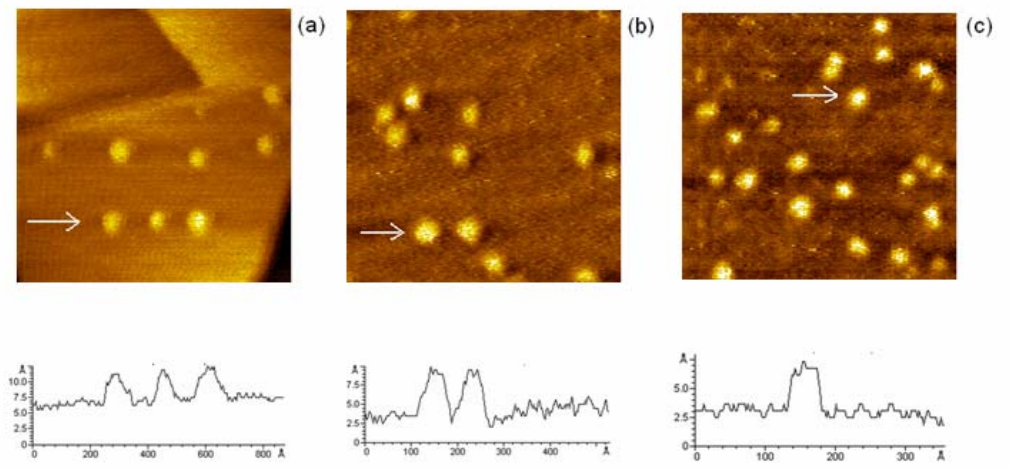

Fig. 20. STM images of PCSS molecules on Au(111) recorded under electrochemical control (a), in air (b), and in nitrogen atmosphere (c). The image sizes are respectively 100x100 nm^2, 52x52 nm^2, and 60x60 nm^2. Tunnelling current 50 pA, Vbias 0.2 V.

For this reason we have first estimated the tunnelling gap between the scanning tip and the gold substrate, and then investigated its relevance when imaging PC mutants chemisorbed on Au(111) [98]. Since the absolute vertical position of the tip over the conductive substrate is difficult to be estimated, generally the tip sample separation can be inferred from the tunnelling current and bias voltage settings, once the corresponding tunnelling resistance has been calibrated against the gap width [69, 70]. In Fig. 21 the dependence of the resistance on

the tip-substrate distance is shown as measured in air and in water environment on an Au(111) substrate by using a Pt-Ir tip. Here, the initial tip position (Z = 0 nm) refers to a tunnelling resistance of 4 x 10^9 Ω, while maximum tip extension corresponds to a contact resistance of 2 x 10^4 Ω [169]. From data in Fig. 21 we inferred tunnelling distances of about 3 nm and 6 nm in water and in air, respectively, at a working resistance of 4 x 10^9 Ω. A clear evidence of the possible tip-molecule interaction, once the tunnelling distance is reduced, is shown in the sequence of STM images as recorded in water for PCSS (see Fig. 22). As inferred by the resistance-distance plot of Fig. 21, the tunnelling gap width was initially reduced from 2.9 nm (Fig. 22 (a)) to 2.4 nm (Fig. 22 (b)). If a tip retraction of 0.5 nm is added to such distances, in both cases the tip has enough vertical space to overcome the proteins, without interfering with their molecular structure. In full accordance, no changes in shape or lateral dimensions were observed for the imaged proteins.

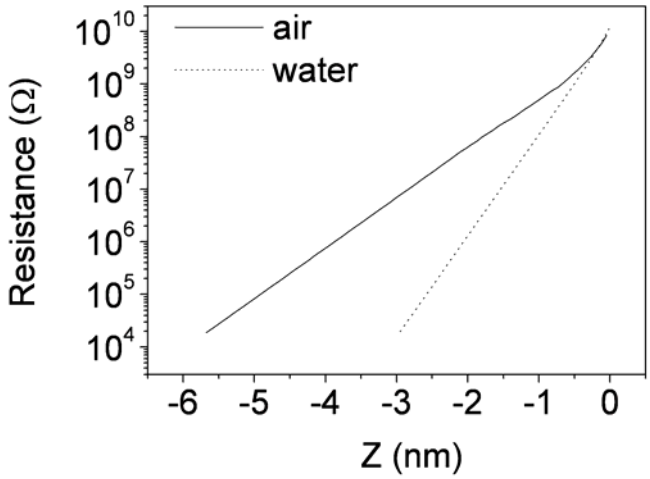

Fig. 21. Tunnelling resistance measured on a flat Au(111) substrate and plotted, in semilogarithmic scale, against the vertical tip position (distance spanned by the tip).

However, when the tunnelling gap was reduced to 1.9 nm (Fig. 22 (c)) by setting the resistance to 4 x 10^8 Ω, the available vertical space results to be 2.5 nm, which is below the physical height of the proteins. As a major consequence, some PCSS molecules display a considerable enlarged lateral dimension. For example, the molecule indicated by the white arrow increases its lateral size from 5.7 nm (Figs. 22 (a), (b)) to 14.9 nm (Fig. 22 (c)). Finally, when the resistance is set to 2 x 10^7 Ω (Fig. 22 (d)), which corresponds to a tip-substrate distance of 1.4 nm, the lateral size of the indicated PCSS molecule is enlarged to a value of 16.9 nm. At the last two tunnelling resistances, the tip can either squeeze or pass through the protein, leading to invasive measurements of the biological sample.

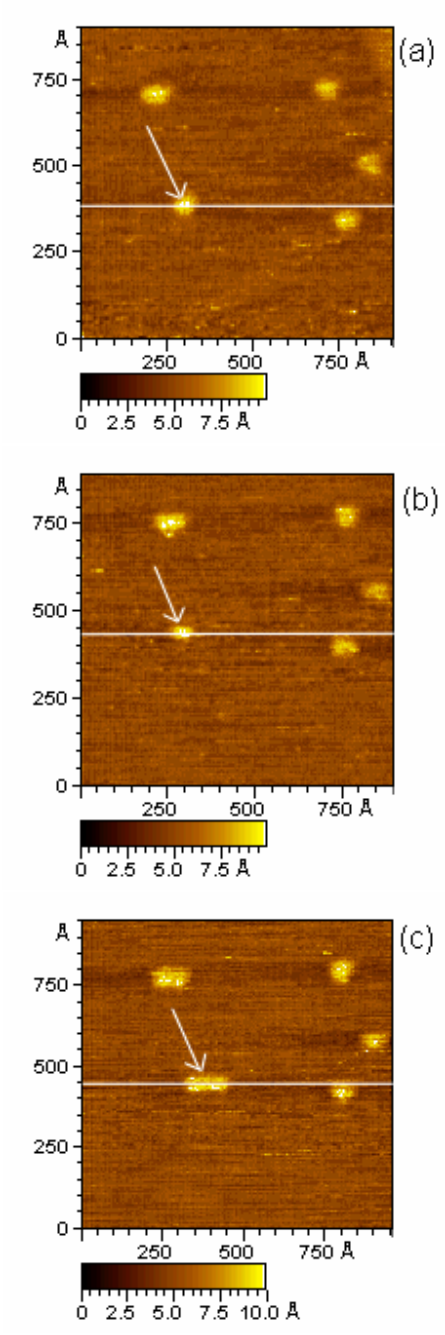
Å
750
500
250
0
250
500
750 Å
0 2.5 5.0 7.5 Å
(a)
Å
750
500
250
0
250
500
750 Å
0 2.5 5.0 7.5 Å
(b)
Å
750
500
250
0
250
500
750 Å
0 2.5 5.0 7.5 10.0 Å
(c)

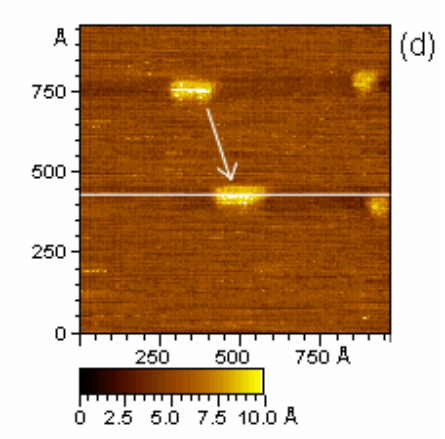

Fig. 22. PCSS proteins adsorbed on an Au(111) substrate as imaged by constant current STM in ultra pure water at decreasing tunnelling resistances: 4 x 10^9 Ω (a), 4 x 10^8 Ω (b), 4 x 10^7 Ω (c), 2 x 10^7 Ω (d).

As a major consequence, both lateral forces and vertical pressure may reasonably cause a deformation of the protein. The strong interaction locally applied could affect either the structure or the function of the bio-molecule, preventing any investigation of the inner electron transport properties. Such results indicate that deviation from optimal imaging conditions can lead to image artefacts induced by the tip interaction with the biological sample.

On the basis of these results, it is important to remark that in the present chapter STM imaging has been done at tunnelling resistance required to non destructive interaction with metalloproteins.

4.2 Conduction of Adsorbed Molecules

4.2.1 Conductive Properties of Single Molecules

The stable binding of the PC mutants allowed studying the conductive behaviour of individual molecules by STS. For both PCSS and PCSH, current-voltage measurements were recorded by positioning the tip over individual molecules. Afterwards, the feedback loop was temporarily disengaged and the tunnelling current was monitored as the sample bias was ramped in the range of ± 1V.

Initially the I-V data were acquired in ambient conditions and compared with those obtained on Au(111) substrates [50]. The slight asymmetry observed for gold finds its explanation in the atomic structure of the tip apex, which has been theoretically and experimentally demonstrated to influence the I-V relation [170]. PCSS molecules exhibit a reproducible and significant asymmetry when compared to gold. In contrast, a slight asymmetric I-V relation for PCSH is observed, being however almost indistinguishable from that of gold within the experimental error.

Although both mutants seem to be electronically coupled to the electrode, the origin of the observed differences is presently not clear. Bearing in mind the importance of the tip-

sample interaction in the STM method, a variation in tip-sample interaction for the two mutants may be envisaged to influence the conductivity of the proteins differently [45, 171]. According to the molecular height analysis performed by TMAFM, a narrower height distribution for PCSS compared to PCSH is found. This seems to indicate a more homogeneous orientation of molecules anchored to gold by the disulfide bridge than when they are anchored via a single external thiol. Therefore, the latter binding is likely to provide more motional freedom to molecules above the substrate, and as a consequence, the two mutants may be indeed subjected to different pressures by the tip.

To get insight into the possible factors influencing the I-V characteristics of the two mutants a more detailed STS analysis under controlled conditions was addressed. One has to consider that the water adlayer, always present at the sample surface, can play a relevant role in the tunnelling mechanism [172, 173]. In several cases the presence of hydration water has been demonstrated to affect image contrast formation especially for insulating samples such as biomolecules [174-176]. Hence, I-V measurements were recorded under nitrogen atmosphere, where we may reasonably assume that the water layer at the sample interface is strongly reduced. In the case of gold substrate and PCSH, the I-V curves closely resemble those obtained under ambient conditions, whereas the asymmetry observed for PCSS molecules has almost disappeared, with a concomitant decrease of the recorded current.

On the basis of results obtained in both environments, it can be reasonably assumed that water molecules adsorbed at the sample-tip interface may be involved in generating the observed PCSS asymmetry. Nevertheless, some observations stand out mainly related to the fact that PCSH presents a symmetric I-V relation under both experimental conditions. In fact, it is hard to conceive that PCSH would retain a different level of humidity with respect to the similar mutant PCSS. We might invoke some differences between the orientation and interfacing of the two mutant proteins towards the electrode surface. In the case of PCSH, binding to gold through the thiol group at the carboxy-terminal free end might lead to a less hindered protein surface-electrode coupling than that obtained via the S-S bridge.

4.2.2 Conductive Properties of Protein Monolayer

PCSS

I-V curves were also acquired for protein monolayer. In view of the expected contact dimensions of a tunnelling tip, data are expected to be representative of the properties of a single or very low number of protein molecules. On the other hand, in this case, the proteins are densely packed and possible effects on protein conductivity, when organised in a monolayer, can be further investigated.

The formation of the PCSS monolayer on the Au(111) substrate was monitored by STM. Full coverage of the substrate was obtained upon 36 hours of incubation time. Fig. 23 shows a STM image taken in ambient conditions. Proteins appear homogeneously distributed to form a well densely packed monolayer.

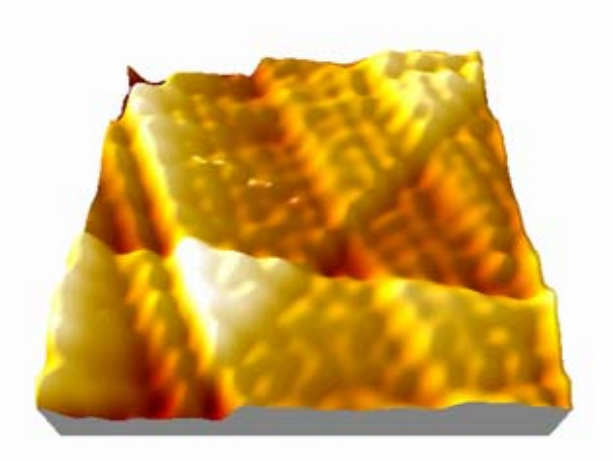

Fig. 23. STM image of a monolayer of PCSS molecules chemisorbed on Au (111), recorded in ambient conditions. Tunnelling current 50 pA, Vbias 0.180 V.

After ascertaining the monolayer formation, the conductivity of the PCSS monolayer was investigated by STS. The experiments were performed in air and at room temperature as described previously. This time I-V characteristics of gold/PCSS/PtIr junctions were measured for different values of initial tunnelling current in order to investigate the influence of the tip-molecule gap on tunnelling spectra. I-V plots recorded at fixed location on PCSS monolayer by varying the initial tunnelling current are shown in Fig. 24. I-V response is asymmetric at the various initial tunnelling conditions explored. However the amount of rectification decreases as the tunnelling current is raised. The data shown for PCSS seem to resemble what obtained by STS analysis for AZ, supporting the dependence of conductive properties on the tunnelling gap width.

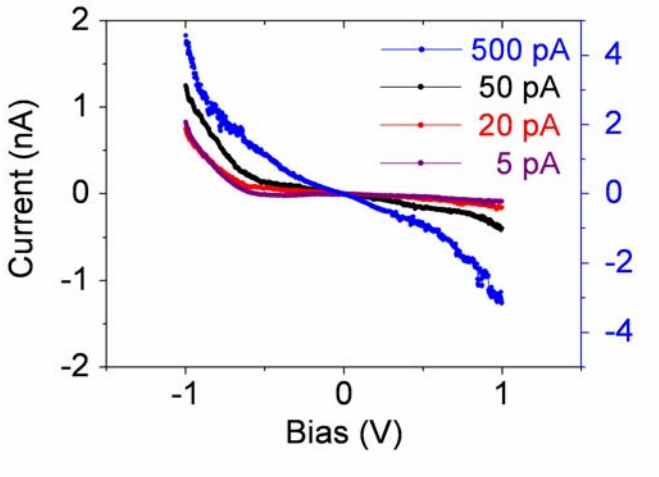

Fig. 24. I-V characteristics recorded by STS on a monolayer of PCSS on Au(111) in ambient conditions. Each curve was recorded at a different initial tunnelling current (over a range of 5-500 pA), i.e. at different tunnelling distances.

We also expanded the voltage range in order to see the effect of the applied bias on the electrical response. A sequence of I-V curves was recorded at the same location by extending the bias range from ± 1V to ± 3 V as shown in Fig. 25. An abrupt change was observed when applying ± 3 V; actually after reaching this voltage, an unusual increase in current flowing was revealed. Nevertheless, the initial conductivity was recovered as soon as the bias range was reduced below ± 2 V. This last finding indicates that the bio-molecule was hopefully not damaged, but only subjected to transient phenomena induced by the strong local electric field applied by the STM tip.

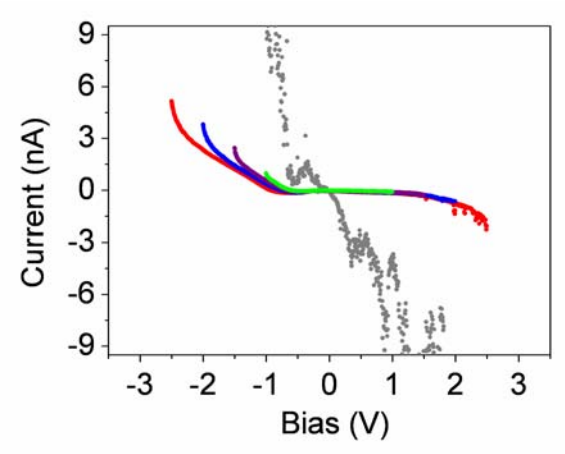

Fig. 25. I-V characteristics recorded by STM on a monolayer of PCSS on Au(111) in ambient conditions, at increasing bias voltage ranges ±1 V (green curve), ±1.5 V (purple curve), ± 2 V (blue curve), ±2.5 V (red curve) and ±3 V (grey curve).

In summary, the STS analysis performed on single molecule and on protein monolayer, pointed out an evident effect of tip-protein gap, in terms of width and water content, on the tunnelling spectra. Therefore, in these measurements the conduction properties of the STM tip/PCSS/gold junction are dominated not only by the protein, but also by the properties of air (vacuum) gap.

To shed light on molecular conductive properties of PCSS, CAFM was employed. In this case the AFM tip can be controllably positioned in direct contact with the protein monolayer thereby eliminating the tunnelling gap. In addition, CAFM allows studying electronic properties of PCSS monolayer as a function of the applied forces. Metal-PCSS-metal junctions were formed by immobilising the proteins through the engineered SS group on the Au (111) substrates. A gold coated AFM tip was used to contact a protein monolayer with a controlled contact force. Scanning on the surface was intentionally avoided so as to minimize any contamination or possible damage to the tip metal coating that may drastically affect the final conductivity signal [177]. I-V characteristics of the so formed junction, as recorded under nitrogen atmosphere at room temperature, are shown in Fig. 26. Within ±1 V (see Fig. 26 (a)), the I-V characteristics appear asymmetric, particularly at higher applied forces. This asymmetry resembles that observed for AZ and correspondingly may be related to the asymmetric position of the redox active centre or also to nature of the molecular contacts. In Fig. 26 (b) the current – voltage response is almost linear, i.e. ohmic, in a bias range within ±

0.3 V. From this bias region, the resistance of the bio-junction was determined and studied as a function of the force exercised by the conductive AFM probe.

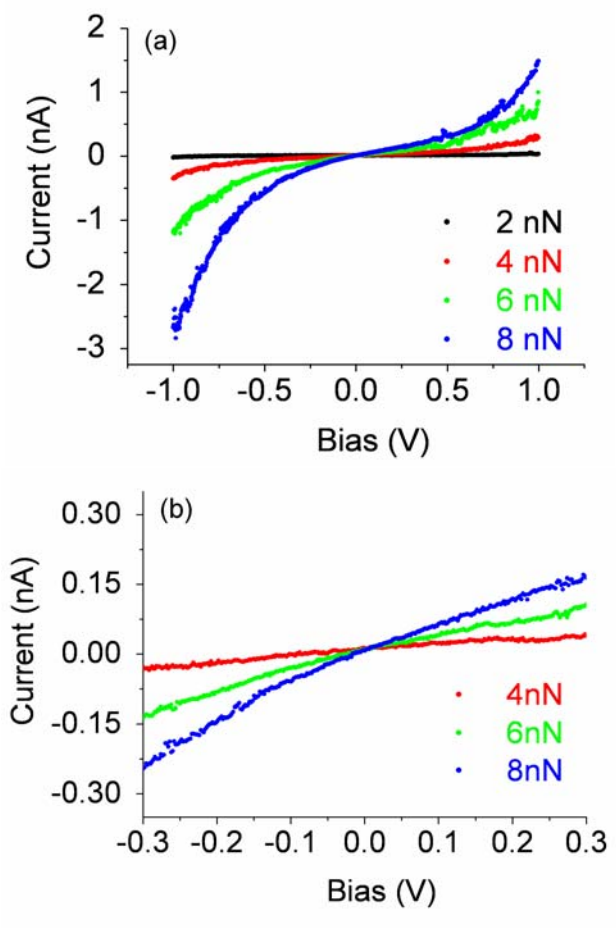

Fig. 26. I-V characteristics recorded under nitrogen atmosphere by CAFM on a monolayer of PCSS; non linear region (a); ohmic region (b).

The resistance – force dependence is shown in Fig. 27. For forces of 3-4 nN the resistance estimated for PCSS proteins was found to be 10^9-$10^{10}\Omega$ a value in agreement with what observed on the copper protein AZ. Nevertheless, the resistance as function of applied forces behaves differently. AZ presents a single exponential dependence, whereas PCSS resistance presents two distinct trends, decreasing exponentially up to 10 nN, and with a faster exponential law for higher forces. The discontinuous behaviour indicates the presence of a critical pressure, at which a jump in the molecular conduction of PCSS molecule occurs. Our data seem to be consistent with an electron transport mechanism, which depends on structural deformations of the compressed protein inside the junction, as proposed for junctions formed with alkane thiol molecules as well [99]. The major difference between the two copper proteins may be related to a more stable structure of AZ compared to PCSS in the force range explored.

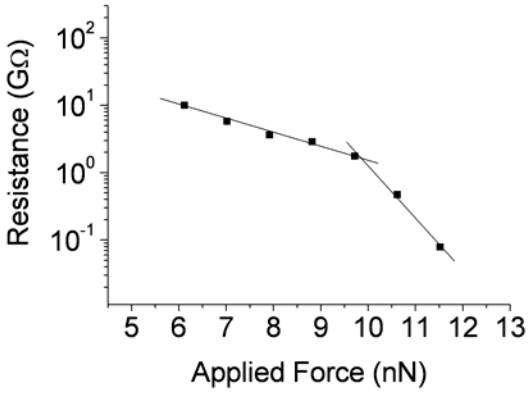

Fig. 27. Semi logarithmic plot of resistance vs applied force obtained by CAFM on a monolayer of PCSS proteins in nitrogen atmosphere.

The dependence of the current on the contact force was further investigated by simultaneously recording force-distance curve and current signal at a fixed bias. Fig. 28 shows the applied force and current flowing through the junction on y axis, and the piezo actuator position on x axes. The experiment was realized on the same metal/PCSS/metal junction previously investigated by local I-V spectroscopy. No current was detected before the AFM probe has contacted the PCSS monolayer. Afterward, the current increases almost linearly until 8 nN. No further increase is recorded up to 20 nN. Above this value, the current signal jumps to a very high value, beyond the pre-amplifier limit. Such behaviour resembles the resistance trend as function of increasing applied forces.

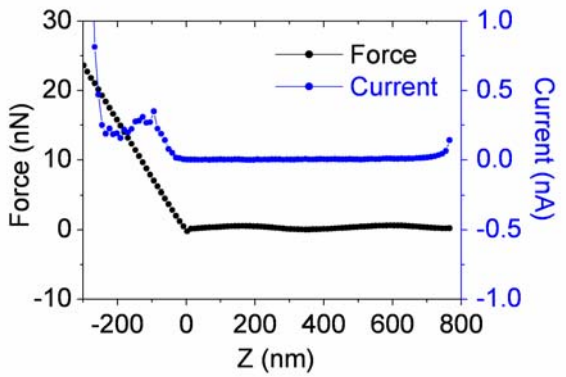

Fig. 28. Current/force vs piezo displacement as recorded by CAFM on a PCSS monolayer at 1 V bias.

In contrast, when similar experiments were repeated by approaching the metal-coated AFM probe on a bare gold substrate, we observed that as soon as the tip approaches the metal surface, the current rises very quickly to values that saturate the preamplifier (data not shown). Therefore, we conclude that the current – force dependence evidenced in Fig. 28 can

be mainly attributed to the presence of the PCSS molecule, which probably undergoes structural changes at a critical pressure.

PCSH

The electrical coupling of PCSH molecules with gold was investigated by STM / STS. In Fig. 29 a typical STM image of a closely dense packed monolayer of PCSH molecule on Au(111) is shown.

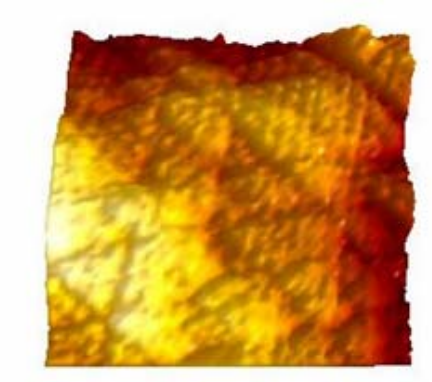

Fig. 29. Monolayer of PCSH molecules chemisorbed on Au (111) surface as imaged by STM in ambient conditions. Tunnelling current 50 pA, Vbias 0.180 V.

I-V characteristics have been recorded at 5 and 50 pA as displayed in Fig. 30, being in both cases the starting bias set at 0.2 V. The STS data show highly asymmetric I-V response for PCSH monolayers at low starting tunnelling current, as also observed for the PCSS mutant and for AZ. In contrast with what observed with PCSS and AZ, the asymmetry completely disappears as the tunnelling gap is lowered. However, the observed symmetric I-V is in accordance with that observed on single PCSH molecules at similar tunnelling conditions [50].

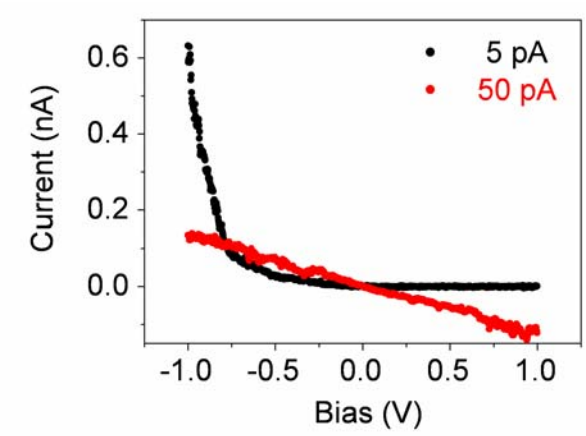

Fig. 30. I-V characteristics as recorded by STS in ambient conditions on PCSH molecules chemisorbed on Au, starting bias condition 0.2V.

The conductive properties of PCSH and the effect of compressibility on conductance were explored with conducting AFM technique. The biomolecular junction was built up by contacting monolayers of PCSH proteins with gold coated AFM probes. All conducting AFM measurements were performed under nitrogen atmosphere to improve the reproducibility. Typical current voltage characteristics as recorded at different pressures are shown in Fig. 31. All plots appear to be highly symmetric and sigmoidal in shape. The high level of symmetry in current signal here observed is in agreement with what observed by STS on single molecules of PCSH under controlled atmosphere [53]. Independently of the applied pressure, I-V plots show an ohmic region within ± 0.1 V (Fig. 32). This is a quite restricted region as compared with other two copper proteins, AZ and PCSS, whose I-V linear dependence was observed up to ± 0.3 V.

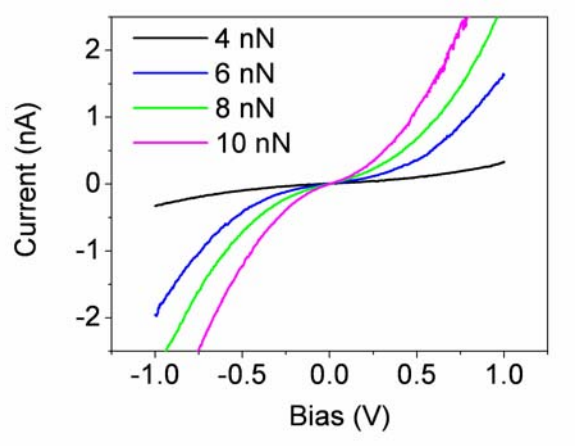

Fig. 31. I-V characteristics as recorded by CAFM on PCSH molecules chemisorbed on Au(111) under nitrogen atmosphere; applied forces varied between 4 nN and 10 nN.

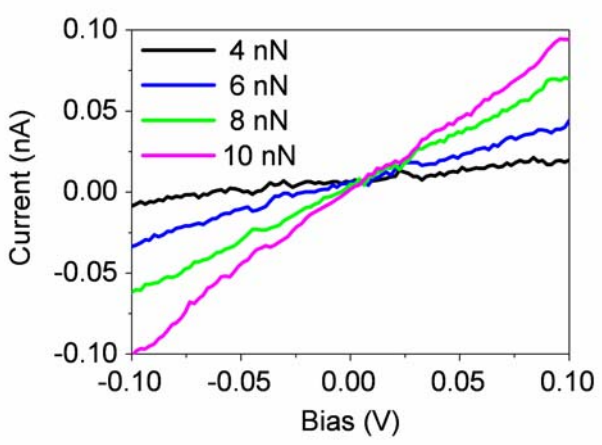

Fig. 32. I-V characteristics as recorded by CAFM on PCSH molecules chemisorbed on Au(111) under nitrogen atmosphere; applied forces 4, 6, 8, 10 nN.

In Fig. 33, the resistance is plotted as a function of the force exercised by the conducting AFM probe. Resistance of the bio-molecular junction decreases when rising forces over a range of 15 nN. Even for this PC mutant, the resistance is scaling with two distinct exponential laws, differently from AZ. Therefore, a simple-uniform-barrier model [104, 178] cannot be assumed to explain the mechanisms of conduction through the metal/PCSH/metal junction. As seen for PCSS, the presence of such discontinuity in the resistance–force dependence confirms the occurrence of an electron transport mechanism dependent on structural deformations of the compressed proteins inside the junction. Nevertheless, applying higher forces is likely to establish a wider tip sample contact area, thus increasing the number of molecules brought into electrical contact.

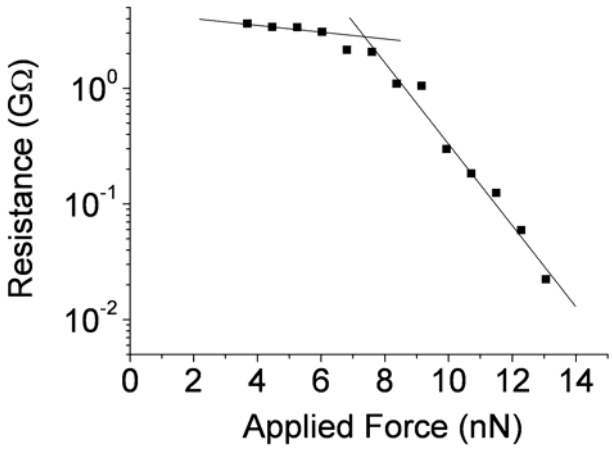

Fig. 33. Semi logarithmic plot of resistance vs applied force obtained by CAFM on a PCSH monolayer under nitrogen atmosphere.

4.3 Functionality and Redox Activity of Adsorbed Molecules

Cyclic Voltammetry

The study on the functionality of PC mutants monolayer covalently immobilised on gold electrode was addressed by CV. In these measurements robust voltammetric responses, stable to continual scanning (>100 cycles at 10 mVs^{-1}), were obtained for PCSS adlayers on polycrystalline gold as shown in Fig. 34. The height of anodic and cathodic peaks is proportional to the scan rate (data not shown) consistently with a redox reversible process of molecules confined at a surface electrode, and the ratio Ia/Ic is 1. The redox midpoint potential of the PCSS adlayer was 162 ± 10 mV vs SCE, a value close to that obtained diffusively with the wild-type protein at edge oriented pyrolytic graphite electrode [179]. This confirms that immobilization at the gold surface is occurring without significant perturbation of the native structure.

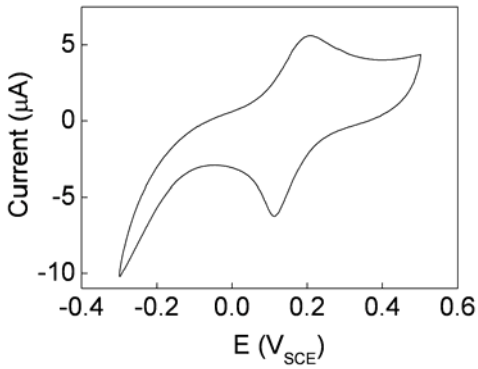

Fig. 34. Voltammogram recorded on gold immobilised PCSS molecules in 100 mM sodium phosphate pH 7.14 at 100 mV/s scan rate.

The surface coverage of electroactive molecules, estimated by integrating the faradaic response, and correcting for an AFM-determined surface roughness factor of 1.3, was of 2-8 × 10^{14} molecules/cm^2. This value is in good agreement with an expected coverage for a molecule with a lateral dimension of ~3.5 nm, and indicates that immobilisation occurs with a high degree of functional retention.

In order to investigate the role of the introduced S-S group, once the protein is tethered on gold electrode, in terms of stability and efficiency of ET, analogue CV measurements were performed on PCWT. As shown in Fig. 35 the recorded voltammogram for PCWT reveals a broader and weaker faradic response if compared to that observed for the immobilised mutant. The PCWT coverage, estimated from the peak areas in the CV spectra, was of 7 × 10^{13} molecules/cm^2, lower than that obtained for the PCSS. Furthermore, calculated peak widths at half height were ~90 mV and 115-125 mV for PCSS and PCWT adlayers respectively. The broader voltammetric peaks observed for the wild-type protein may be indicative of uncontrolled protein surface orientation. In the absence of a surface anchoring-group, the protein is expected to be physically adsorbed rather than chemically anchored, and the protein-surface interaction is clearly quite different to that observed with the mutant.

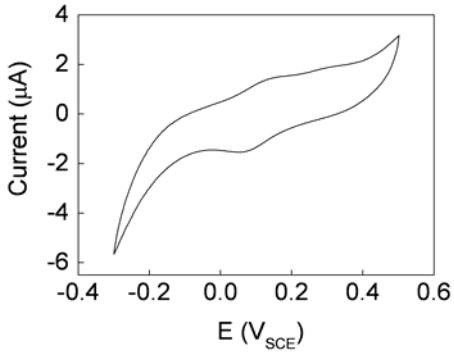

Fig. 35. Voltammogram recorded on gold immobilised PCWT molecules in 100 mM sodium phosphate pH 7.14 at 100 mV/s scan rate.

Typical voltammograms recorded on PCSH immobilised on gold are represented in Fig. 36, for increasing scan rates. Independently of the sweeping rate, two well distinct peaks due to the oxidation and reduction process are evident. The high symmetry of voltammograms and the peak separation, very close to the theoretical value, indicates that the redox process is fully reversible and almost ideal.

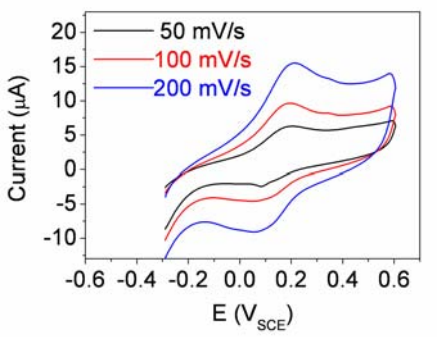

Fig. 36. Voltammograms recorded for PCSH adlayers on bare poly crystal gold in 20 mM sodium phosphate at pH 6.

To investigate possible kinetics effects, the anodic and cathodic peak current was plotted versus the scan rate (Fig. 37). Since the current was increasing linearly with the scan rate, we believe that PCSH molecules were firmly immobilized on gold. To estimate the redox midpoint and the surface coverage, the background current generated by the gold electrode in buffer was subtracted to the cyclic voltammogram recorded on the PCSH adlayers on gold. Fig. 38(a) shows the CV graph for PCSH, and in Fig. 38(b) the background subtraction result is presented. From this graph, the redox midpoint for PCSH molecules immobilized on bare gold was found to be +168 mV_{SCE} ± 10 mV, a value close to that obtained diffusively with the wild-type protein and the PCSS mutant. Furthermore, the peak separation was 72 mV, suggesting a quasi-ideal ET consistent with no significant perturbation of the native structure. To estimate the electroactive surface coverage, the faradaic current was integrated, being the result in excellent agreement with a gold electrode entirely covered with PCSH molecules.

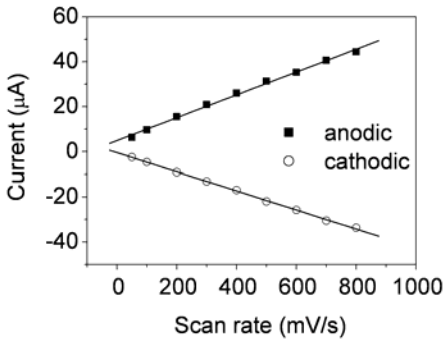

Fig. 37. Anodic (filled squares) and cathodic (open circles) peak current vs. voltage scan rate, as measured from cyclic voltammograms of Fig. 36.

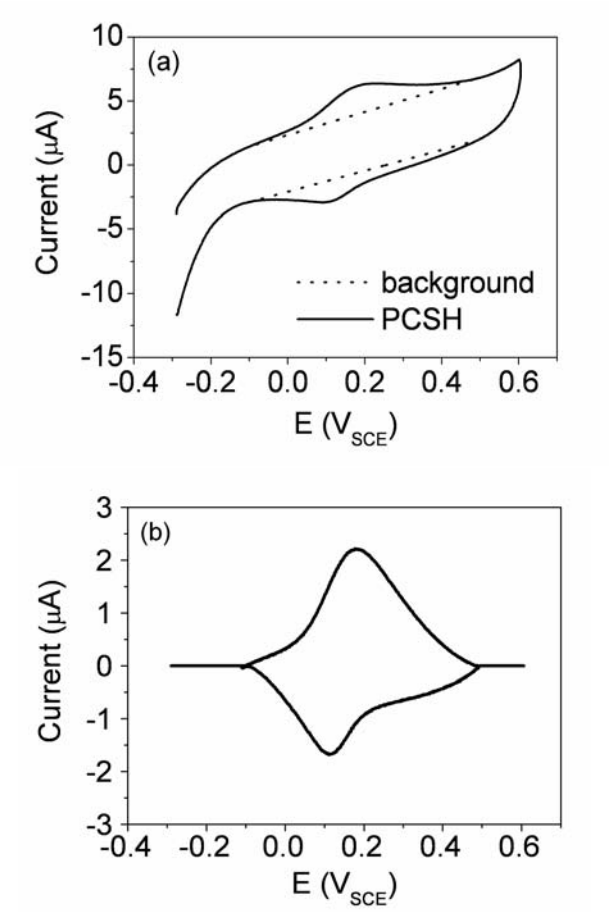

Fig. 38. (a) Voltammograms recorded in 20 mM NaP at pH 6 of bare polycrystal gold (dot line) and PCSH adlayer (solid line); (b) result of background subtraction.

In Situ ECSTM

With the aim to investigate the ET capabilities of the adsorbed single mutants, as well as the role of the copper atom in the tunnelling mechanism, STM imaging under electrochemical control was performed. By using a bipotentiostat, the electrochemical potential of the two working electrodes (substrate and tip) was tuned in a wide range around the redox midpoint potential of the proteins [179]. In Fig. 39, a sequence of in situ STM images of PCSS adsorbed on Au(111) is shown for three of the several substrate electrochemical potentials investigated, ranging between - 222 mV and + 28 mV vs SCE. The molecular features are clearly visible for substrate potentials close to the midpoint potential (Fig. 39 (a)), the image contrast is weaker when the potential is far from this value (Fig. 39 (b)) and it is recovered once the initial potential is re-established (Fig. 39 (c)). This effect is also reflected in slight changes of height in the cross sections. Such findings seem to be consistent with results reported for AZ, although in that case a full bleaching was observed.

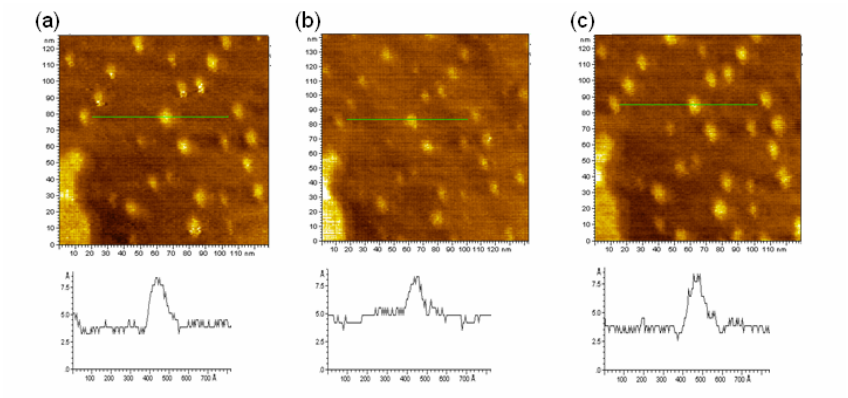

Fig. 39. STM imaging under electrochemical control in constant current mode of PCSS molecules in 50 mM ammonium acetate, pH 4.6. Scan area: 120 x 120 nm2. Tunnelling current 50 pA; Vbias 0.180 V (tip positive), scan rate 4 Hz. Substrate potential is + 28 mV vs SCE (a), -222 mV vs SCE (b), + 28 mV vs SCE (c). Single molecule cross section profiles are shown in the lower panel.

They support, as already predicted by theoretical models [66, 150], that the copper site represents a preferential way for the tunnelling process through the protein, once its redox levels are properly aligned with the substrate and tip Fermi levels.

Similar STM experiments were performed for the PCSH mutant. In Fig. 40 (a), (b), (c) a sequence of ECSTM images is shown for substrate electrochemical potentials ranging from – 222 mV to + 28 mV vs SCE. No relevant contrast variation is observed upon sweeping substrate potential, as is also evident from the unchanged height in the cross sections. The redox functionality of adsorbed mutant was demonstrated in CV experiments, therefore, we can hypothesize that the higher protein flexibility resulting from immobilisation via external SH group may lead to an unfavourable alignment of molecular redox levels with tip and substrate Fermi levels [37, 40, 61].

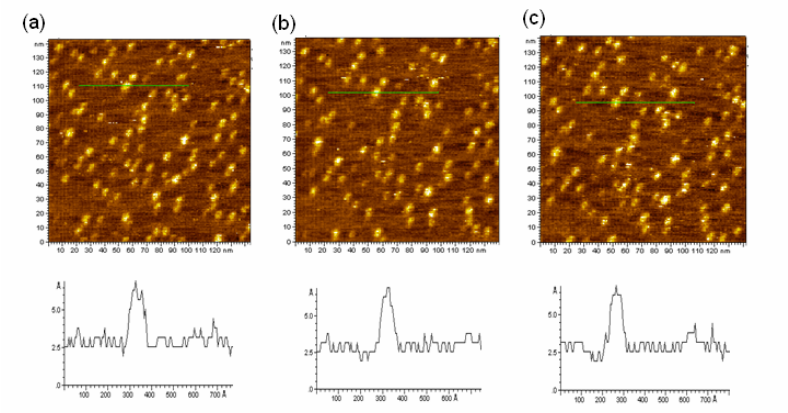

Fig. 40. STM imaging under electrochemical control in constant current mode of PCSH molecules in 50 mM ammonium acetate, pH 4.6. Scan area: 140 x 140 nm2. Tunnelling current 50 pA, Vbias 0.180 V (tip positive), scan rate 4 Hz. Substrate potential is + 28 mV vs SCE (a), -222 mV vs SCE (b), + 28 mV vs SCE (c). Single molecule cross section profiles are shown in the lower panel.

4.4 Molecular Dynamics Simulations

Similarly to what observed for AZ, the RMSF of both PCSS-I ($<\Delta r^2>^{1/2}$=(0.013± 0.005)nm) and PCSS-II ($<\Delta r^2>^{1/2}$=(0.015± 0.005)nm) are significantly lower in comparison to that of PCSS ($<\Delta r^2>^{1/2}$=(0.03± 0.01)nm). Accordingly, the flexibility of the macromolecule can be affected by the immobilization onto a substrate. The observation that larger RMSF values are revealed in PCSS-II with respect to PCSS-I suggests that the presence of two covalent bonds might yield a larger flexibility at least in same regions of the macromolecule.

The trend with time of θ and Φ (for definition see Fig. 16), calculated during the MD trajectory, are plotted, for both PCSS-I and PCSS-II, in Fig. 41. In both cases, a significant deviation of **p** from the normal axis is registered, according to what observed for AZ. This means that both the gold-anchored systems can assume different orientations with respect to the gold electrode. In addition, the mean value of θ is smaller for PCSS-I than for PCSS-II (see legend of Fig. 41); this means that the protein anchored by a single bond assumes a configuration closer to the normal. Such a behaviour might be indicative of a less extensive contact, for PCSS-I, between the protein and the gold atoms.

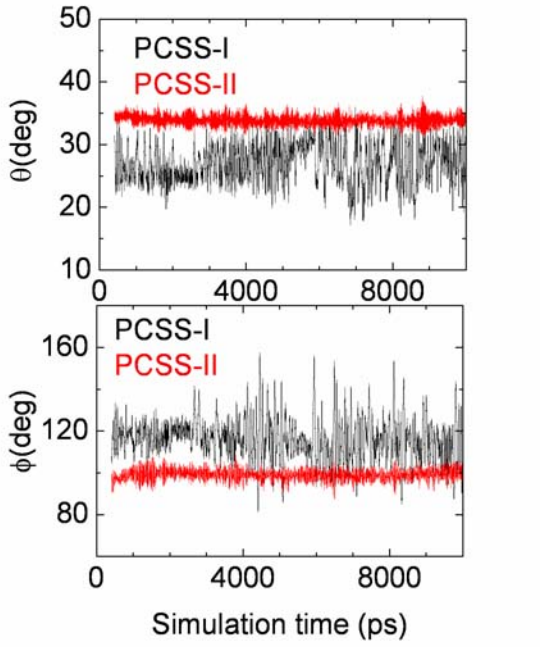

Fig. 41. Temporal evolution, along a 10 ns MD trajectory, of θ and Φ angles describing the orientation and the precession, respectively, of the protein **p** axis with respect to gold surface normal, for the PCSS-I (black) and PCSS-II (red). The mean value and the standard deviation of θ are (27± 3)° and (34± 1)° for PCSS-I and PCSS-II, respectively. The mean value and the standard deviation of Φ are (116± 10)° and (99± 3)° for PCSS-I and PCSS-II, respectively.

Furthermore, we note that θ exhibits a larger standard deviation for PCSS-I with respect to PCSS-II (see legend of Fig. 41); such a behaviour being in agreement with higher degrees

of freedom for PCSS-I with respect to PCSS-II. It is interesting to note that, for both PCSS-I and PCSS-II, the spread of θ is larger in comparison to that of AZ. Such a result can be attributed to the maintaining of an intramolecular disulphide bridge in AZ which, preserving a more rigid structure, can induce a decrease in the flexibility of the overall protein. Concerning Φ, PCSS-I and PCSS-II show different average values, reflecting a different average position of the macromolecule with respect to the gold substrate. Interestingly, a much larger standard deviation of Φ is observed for the PCSS-I in comparison with PCSS-II (see legend of Fig. 41). Such a result, together with what observed for θ, is indicative that the macromolecule, during its dynamical evolution, can assume different arrangements with respect to the gold surface; such a variability being more marked in the case of a single anchoring point. Notably, the trend of Φ for PCSS-I shows, over the fluctuations, oscillations whose presence might be indicative a sort of periodicity in the lateral movements of the macromolecule anchored by a single sulfur-gold bond. Again, both the PCSS-I and PCSS-II exhibit a spread in Φ larger than that of AZ. This is indicative of the fact that PCSS moves more freely, in comparison to AZ, with respect to the gold surface.

To compare the MD simulated and AFM data, the ellipsoid and its corresponding height over the gold substrate, extracted from the MD simulated trajectories, are shown in Fig. 42 by sampling structures every 10 ps. It comes out that a single mode distribution is registered for both PCSS-I and PCSS-II. The mean values are, in both cases, close to that expected for the crystallographic data by assuming that protein is anchored to gold via the disulphide bridge (h ~ 3 nm). On the other hand, PCSS-I is characterized by a mean value slightly higher than that of PCSS-II (see the mean values in Fig. 42). Such a finding is consistent with the previous results showing that the protein anchored by a single bond can assume, in average, a configuration closer to the normal to the surface.

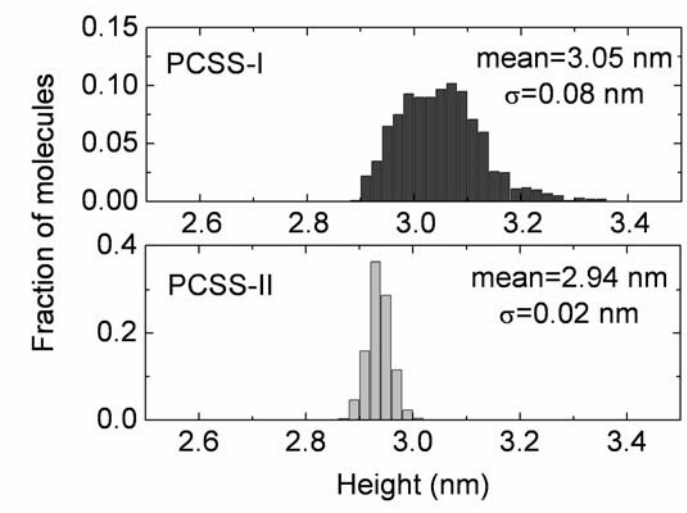

Fig. 42. Statistical analysis of the molecular height above the Au(111) substrate, as extracted from the MD simulated trajectories for PCSS-I and PCSS-II. The vertical dimension of proteins has been estimated from 1000 molecules sampled every 10 ps of the MD simulated trajectory.

For both systems, a spread of heights is registered (see the standard deviations in Fig. 42). Generally, this means that, during its dynamical evolution, the macromolecule, by exploring its accessible conformations, can assume a variety of arrangements, and then of heights, with respect to the gold substrate. On the other hand, we note that PCSS-I is characterized by a wider distribution in comparison with PCSS-II. As a consequence, molecules covalently bound to gold through a sulfur atom show slightly higher flexibility than molecules anchored via two covalent bonds. In this respect, we remark that the spread observed for PCSS-II is in agreement with that observed for AZ. This finds a correspondence with the presence, in AZ, of the disulfide bridge which can restrict the protein movements with respect to the gold substrate.

These results are in a qualitative agreement with those derived by TMAFM. However, we note that the height distributions, as extracted by MD simulation, result markedly narrower if compared to those derived by TMAFM (see Fig. 19). To explain such discrepancies different effects should be taken into account. First, we remark that TMAFM data refer to a collection of molecules, likely in different starting arrangements, which, moreover, may be anchored to gold by one or both sulfur atoms, whereas MD simulations consider only a single molecule and the two different way of anchoring separately. Additionally, it should be taken into account that a further contribution to the structural and dynamical heterogeneity of the adsorbed protein could arise from the complex interaction between the protein and the gold surface. A more accurate modellization of this interaction should be introduced in the MD simulations.

Finally, it should be stressed that TMAFM is sensitive to protein movements on a much longer time scale (at least milliseconds if we refer to a tapping frequency in the range of kHz). Therefore, it can be hypothesized that the flexibility of the molecules, on this temporal scale, above the substrate can also contribute to the broadening of the experimental height distribution; during the measurements the proteins assuming different arrangements. Nevertheless, we remark that, even in the restricted temporal window as explored by MD simulation, our data show that the proteins can assume a variety of orientations with respect to the gold substrate.

5 Yeast Cytochrome c on Au(111) Electrodes

Several works have shown that adsorption of cytochrome c on bare gold electrodes via the cysteine residues directly bound to the heme group (namely Cys14 and Cys17) is very critical, as for horse hearth cytochrome c which has no additional cysteines. In particular many groups have found that, upon adsorption on gold surface, horse hearth cytochrome c does not give well-defined and stable electrochemical response, due to formation of aggregates [180] progressive adsorption of inactive molecules [181] or even protein denaturation [182].

Here we focus on a particular cytochrome c (YCC), which thanks to the additional sulphur-containing group (Cys102), not directly bound to the heme group, is suitable for direct chemisorption on bare gold electrode (see Fig. 1), while avoiding the perturbation of the heme active site. In what follows, we present a deep investigation of morphological, conductive and functional properties of the immobilized YCC molecules, at the single molecule level.

5.1 Morphological Characterization

Morphological characterisation of YCC molecules self assembled on Au(111) was provided by combined AFM and STM experiments. We found that the density of adsorbed YCC molecules above Au(111) can be varied from very low density to full coverage by suitable choice of the incubation time. A representative topography of YCC molecules adsorbed on the Au(111) surface is shown in Fig. 43. The sample was incubated several hours and measured by TMAFM in buffer solution. Several images similar to that shown in Fig. 43 were recorded from different areas of the sample, revealing the presence of adsorbed proteins uniformly distributed over the Au(111) surface and with homogeneous size. Single molecules are well resolved above the gold substrate, as shown in the high-resolution image of Fig. 44 (a), and there is no evidence of aggregates or of protein mobility above the substrate, as for robust binding of proteins to gold. A representative cross section profile of a single YCC molecule is shown in Fig. 44(b). The molecular height above the gold surface can be estimated from the maximum vertical size. A systematic analysis of cross section profiles over 440 different YCC molecules provided the statistical distribution of protein vertical size. The resulting histogram, shown in Fig. 45, indicates a single mode distribution. The mean height of YCC molecules above the gold substrate results 2.6 nm, with a standard deviation of 0.7 nm. This value, within the error, is close to X-ray crystallographic data, [130] and to the value expected for a non-denaturing immobilisation on gold via the sulphur atom in the Cys102 residue (about 3.8 nm). The standard deviation of the height distribution can be connected to the protein flexibility above the substrate. The standard deviation estimated for adsorbed YCC molecules (σ = 0.7 nm) is closer to the value found for the PC mutant anchored via the single thiol (σ = 0.6 nm), rather than to the lower value found for PCSS (σ = 0.5 nm), consistently with a comparable flexibility of the two molecules above the substrate. Nevertheless YCC value for σ is also close to the value found for AZ (see paragraph 3.1.), but it is important to recall that a low-height form of adsorbed AZ has been observed, which contributes to spread the overall AZ height distribution.

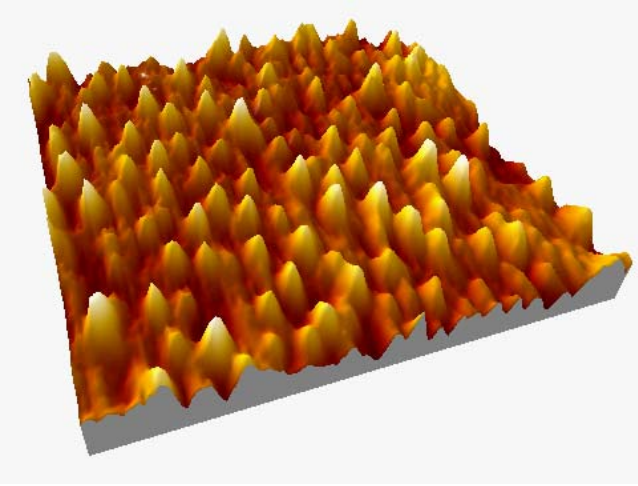

Fig. 43. Topographic image of YCC molecules adsorbed on Au(111) as measured by TMAFM in buffer solution. Scan area: 600 x 600 nm^2. Vertical range: 6 nm.

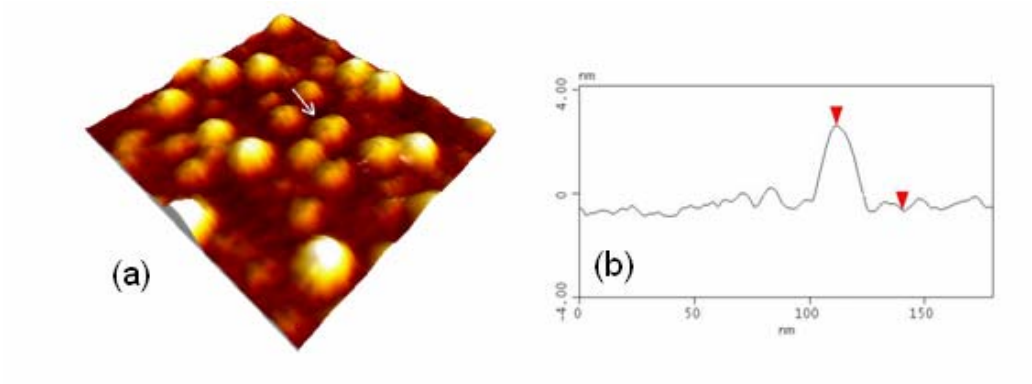

Fig. 44. (a) TMAFM image of YCC molecules adsorbed on Au (111), recorded in buffer solution, with (b) representative cross section profile as recorded for the molecule indicated by the white arrow in Fig 44 (a). Scan area: 145 x 145 nm^2. Vertical range: 8 nm.

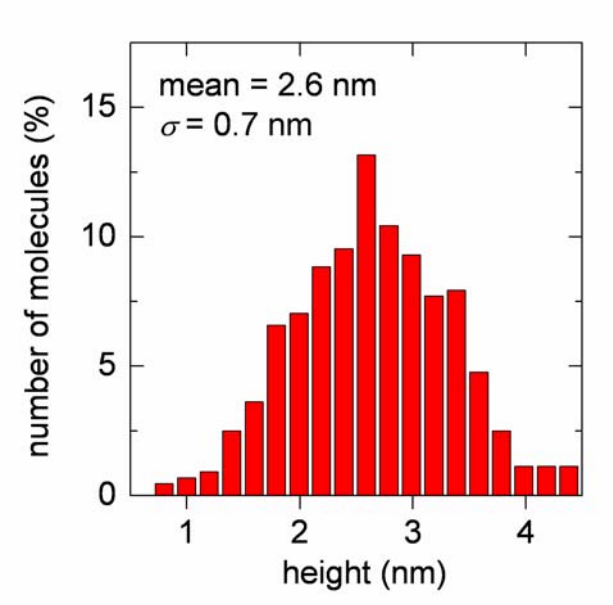

Fig. 45. Statistical analysis of YCC molecular height above the Au(111) substrate, as measured by TMAFM under buffer solution. The vertical dimension of the proteins was estimated from individual cross section analysis of 440 different molecules.

The typical protein lateral dimension, as evaluated from full width at half maximum of molecule cross section profile (see Fig. 44 (b)), is in the range 20-30 nm, considerably larger than the crystallographic data [130], due to the well-known tip broadening. Therefore, adsorbed YCC molecules have been imaged by STM in ambient conditions. A typical STM image recorded in air from a sample incubated for about one hour with the protein solution is shown in Fig. 46 (a).

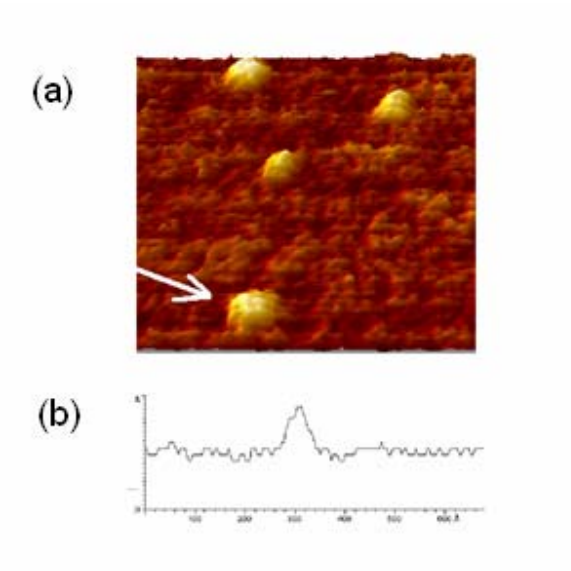

Fig. 46. (a) STM image of YCC in ambient conditions, with (b) representative cross section profile recorded for the molecule indicated by the white arrow in Fig. 46 (a). Tunnelling current 100 pA, V_{bias} -0.300 V (tip positive), scan rate 1.5 Hz, scan size 70 x 70 nm^2.

To verify the robustness of the single protein-gold bond, the same area was consecutively imaged at different tunnelling currents, from 50 pA up to 1 nA and bias fixed at -0.3 V. In such a way, the tip-protein distance was reduced, i.e. the local tip-molecule interaction was increased. Despite this procedure, none of the imaged YCC isolated proteins was swept away, confirming a robust binding of YCC to gold. The typical molecule cross-section profile is reported in Fig. 46 (b). The full width at half maximum provides an estimate of YCC lateral dimension with values in the range 4.8 ± 0.7 nm, close to that obtained from X-ray crystallography. In contrast, the height of adsorbed YCC molecules (0.3-0.5 nm) is notably smaller than the crystallographic size, as already observed and discussed for AZ and PC mutants (paragraphs 3.1 and 4.1).

5.2 Conduction of Adsorbed Molecules

Tunnelling spectroscopy was employed to investigate the electronic conduction of YCC monolayers on Au(111) substrate. Two typical I-V plots recorded in air at room temperature for different initial tunnelling currents are shown in Fig. 47. While the current-voltage characteristic recorded at 10 pA is asymmetric, the I-V plot obtained at 50 pA does not show any appreciable rectification properties. The same effect was observed for the PCSH mutant, which interestingly is also characterized by the presence of a single cysteine suitable for covalent immobilization on a gold surface.

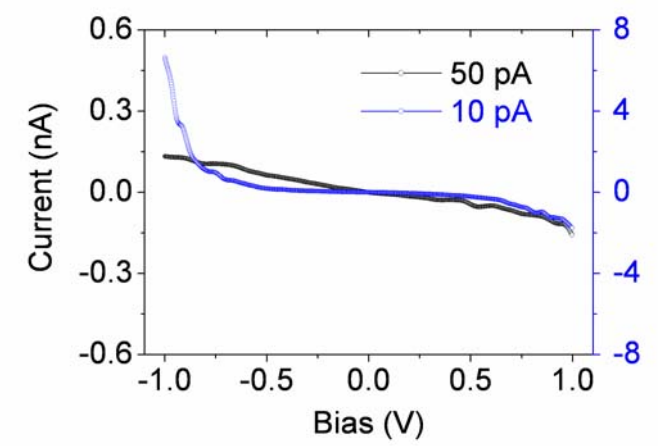

Fig. 47. I-V characteristics as recorded in air by STS on YCC monolayer chemisorbed on Au(111).

Similarly to the copper proteins, the electrical conductivity of the YCC protein was further examined by CAFM technique. For this purpose, YCC molecules were self assembled on a single crystal Au electrode. A two terminal junction was obtained by contacting the YCC monolayer with a metal-coated AFM probe. I-V spectroscopy was performed under nitrogen atmosphere, so as to minimize any contribution from the water surrounding the bio-molecules. A sequence of I-V plots recorded at different forces is shown in Fig. 48. I-V characteristics recorded within ±2 V appear to be almost symmetric with respect to the applied bias. A similar symmetric current response was also found for the PC mutant tethered to gold with a single SH group indicative of no preferential direction for the current flow. This implies the formation of a symmetric metal/protein/metal junction, as conversely revealed for the copper proteins (AZ and PCSS) immobilised via the SS group.

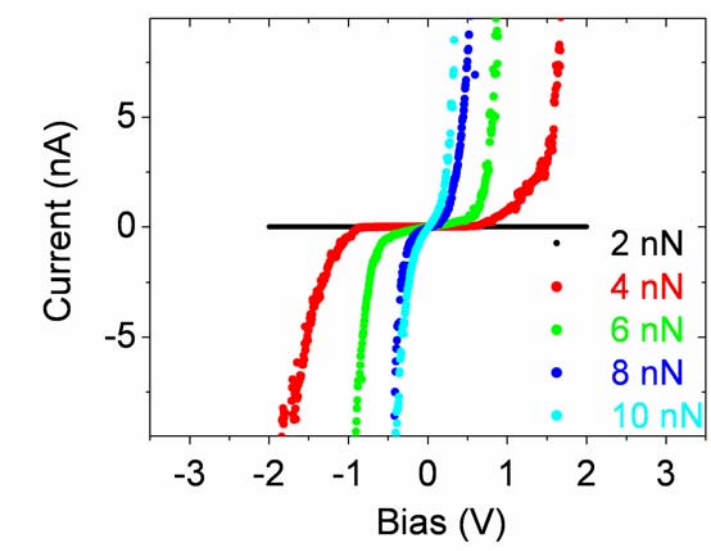

Fig. 48. I-V characteristics as recorded by CAFM on an YCC monolayer on Au(111) in nitrogen atmosphere.

The linear portion of the I-V characteristics between ± 0.2 V was used to define the junction resistance, and studied as a function of the force exercised by the AFM probe. Fig. 49 shows the typical response obtained on a monolayer of YCC molecules included between the Au(111) substrate and the metal coated tip. In the range of forces explored, resistance shows a well marked point of discontinuity at 7 nN, and almost three different regimes. Such a complex dependence of the resistance on the applied force is very difficult to be described in term of simple transport mechanism. At the moment we may argue that several factors can contribute. A simple increase in the contact area between tip and YCC monolayer may explain the exponential decrease of resistance from 0.2 to 6.3 nN. The overcoming of a sort of contact resistance at the tip/YCC interface may justify the jump of more than one order of magnitude at 7 nN. An inner structural reorganization of the YCC molecule may cause the discontinuity of the resistance at 14 nN.

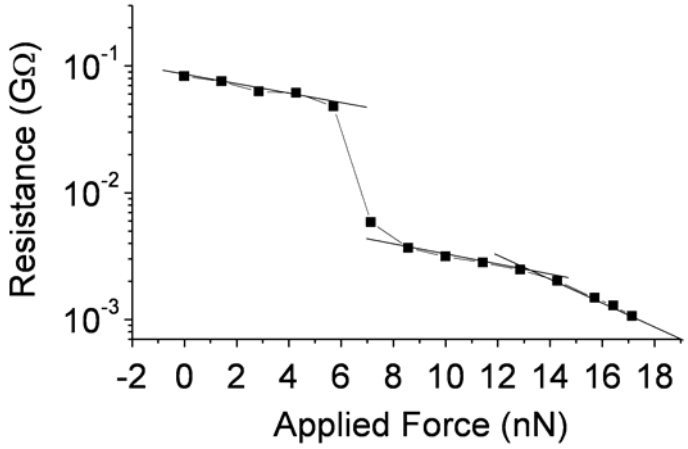

Fig. 49. Semi logarithmic plot of resistance vs applied force obtained by CAFM on a monolayer of YCC proteins adsorbed on Au(111) in nitrogen atmosphere.

The effects of mechanical compression on conductivity were additionally investigated by recording force-distance curve and current signal, simultaneously at a fixed bias. Fig. 50 shows the typical result obtained when a metal coated AFM probe approached a YCC monolayer chemisorbed on Au(111). As clearly visible in the graph, current starts to flow as soon as the tip is in contact with the bio-molecules. Thus, the current increases exponentially until forces overcome 4 nN. Then, the junction conductivity remains almost constant, and finally the current jump to the saturation level when the applied force exceeds 5 nN.

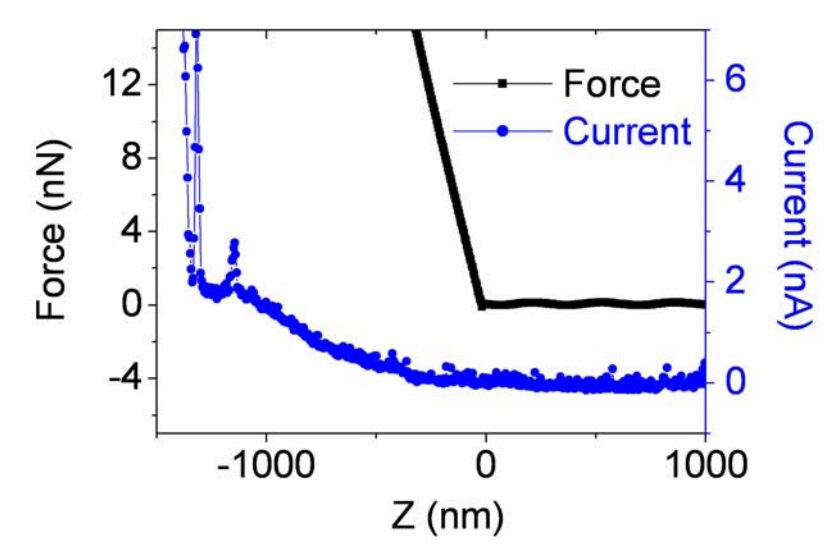

Fig. 50. Current/force vs piezo displacement recorded by CAFM on a monolayer of YCC monolayer on Au(111); bias applied +1 V.

5.3 Functionality and Redox Activity of Adsorbed Molecules

Cyclic Voltammetry

The functionality of immobilised YCC on bare gold electrodes was investigated by CV experiments where the faradaic current was measured as a function of the substrate potential. The first cycle as recorded in pure buffer solution is shown in Fig. 51. The first cycle reveals the presence of two peaks corresponding to the oxidation and reduction of YCC in the native form and a second cathodic peak with a transient behaviour, which may be consistent with the alkaline form of YCC [183]. Fig. 52 shows the typical cyclic voltammograms, recorded after ten cycles, for Au(111) electrodes incubated with YCC solution overnight. The measurements were done in buffer solution at voltage scan rates of 10-150 mV/s. Only two peaks can be clearly observed, corresponding to the reduction and oxidation of YCC. The presence of a single anodic and a single cathodic peak is indicative of redox reactions all occurring at a well-defined potential, consistently with the presence of YCC monomers at the surface [184]. The voltammetric response is highly stable, persisting in unperturbed form for hours of experimentation, and is indicative of a quasi–reversible electrochemical process.

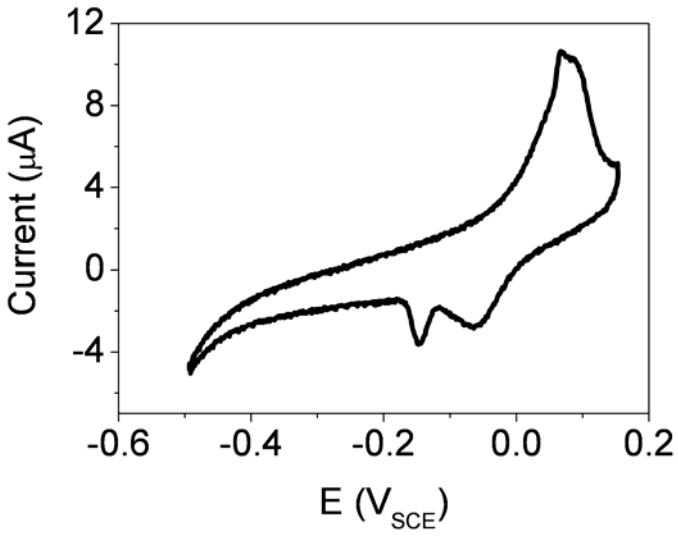

Fig. 51. First cycle voltammogram of YCC on Au(111) electrode as recorded in pure buffer.

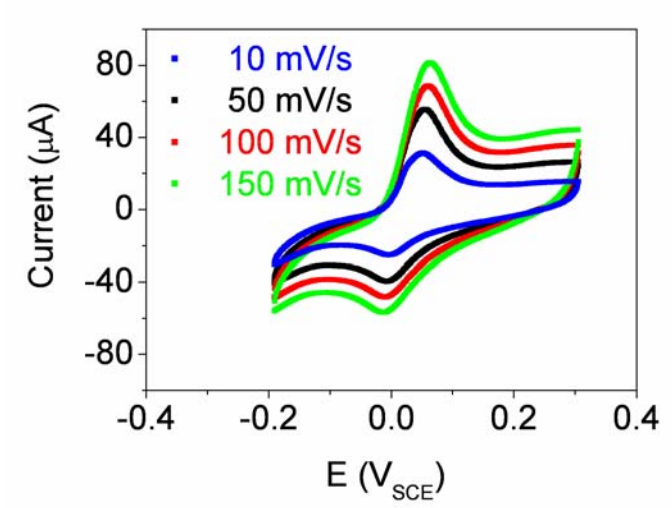

Fig. 52. Cyclic voltammograms of YCC on Au(111) electrode; data are recorded in buffer solution.

To estimate the redox midpoint, data were renormalized by subtracting the faradaic current of the Au(111) bare substrate. In Fig. 53 the result of the background subtraction is presented. The redox potential, as estimated from CV, is +0.27 ± 0.02 V referred to SHE, which is in agreement with reported values for cytochrome c [185] and close to the value found with this technique for YCC adsorbed on gold modified electrodes [186].

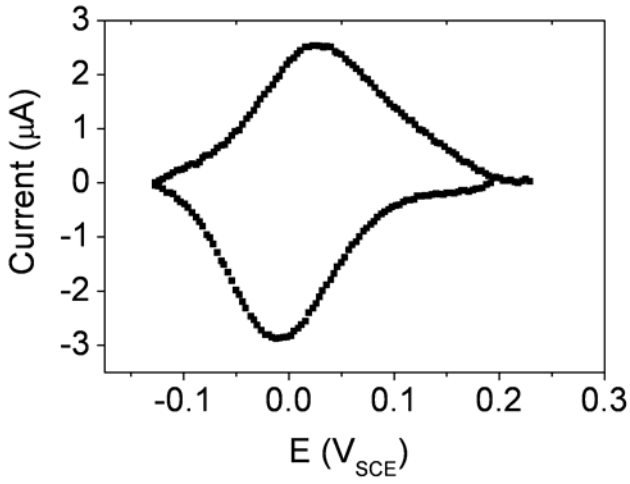

Fig. 53. Cyclic voltammogram of YCC on Au(111) electrode after subtracting the faradaic current of the bare substrate. Data are recorded in buffer solution at a potential scan rate of 50 mV/s.

Anodic and cathodic peaks are separated by 0.075 V, which is quite close to the value expected for an ideal one-electron transfer reaction [135]. This is an indication that the ET process is not influenced by the direct adsorption on gold, as instead it was observed for other types of cytochrome c proteins [181].

The height of anodic and cathodic peaks was monitored as a function of the voltage scan rate, as reported in Fig. 54. The linear dependence of the peak current versus the voltage scan rate is consistent with the redox reaction of an adsorbed species. An estimate of the surface coverage with YCC electroactive molecules has been obtained from the following relation:

$$I_p(\nu)=[N\, n^2F^2/(4RT)]\ \nu \qquad (2)$$

where I_p is the peak current (anodic or cathodic), ν is the voltage scan rate, N is the number of redox active sites on the surface, n is the number of electrons transferred, F the Faraday's constant, R the gas constant and T the temperature. From the slope of the peak current I_p versus the scan rate ν, with $n=1$, we estimate a surface coverage of 1.21 x 10^{-11} mol/cm^2. For YCC molecules adsorbed on the electrode surface forming a closely packed monolayer, the surface coverage is expected to be 1.44 x 10^{-11} mol/cm^2 [187], assuming that each of the adsorbed molecules has the same size as that obtained by X-ray diffraction [130]. Therefore, our data indicate that up to 84% of the electrode surface was successfully functionalised with electro-active proteins. Such coverage estimate is consistent with that found by SPM of samples incubated overnight. For the 16% missing coverage, as estimated by CV, we cannot exclude some deposition of alkaline form of YCC at pH 8, even though it is normally observed at pH higher than 9 [183].

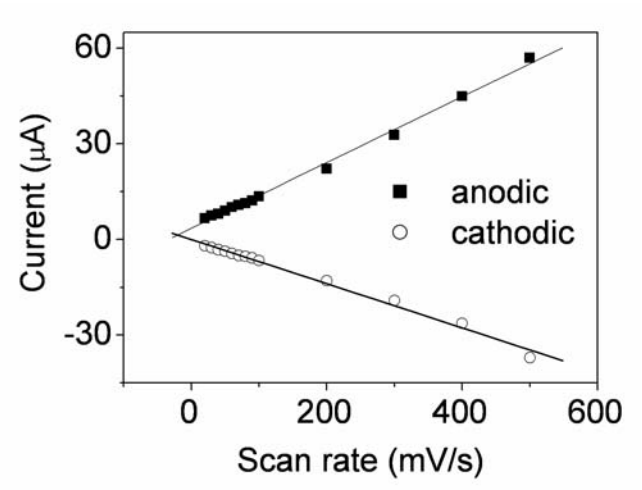

Fig. 54. Anodic (filled squares) and cathodic (open circles) peak current vs. voltage scan rate, as measured from cyclic voltammograms.

In Situ ECSTM

To investigate the ET through individual tethered YCC, we also performed *in situ* STM in electrolyte, where the electrochemical potential of the two working electrodes involved in the measurement, i.e. substrate and tip, was controlled separately. Fig. 55 reports a STM image of single YCC on Au(111) acquired at a substrate potential of +270 mV vs SHE, in TRIS electrolyte.

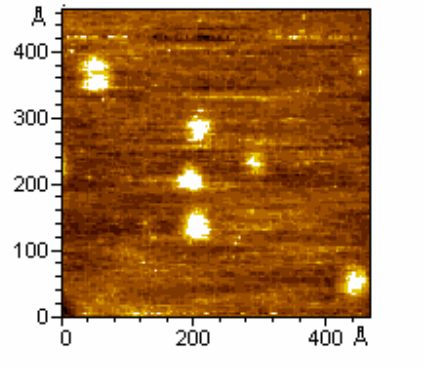

Fig. 55. Isolated YCC proteins chemisorbed on gold substrate as measured in buffer solution by STM at electrochemical potential of +270 mV_{SHE}. Tunnelling current 50 pA, V_{bias} 0.200 V (tip positive), scan rate 2 Hz.

Here, the substrate electrochemical potential was appositely tuned to a value close to the redox midpoint of the protein. In other metalloproteins like AZ and PC mutants, we proved that tunnelling appears to take place through a favourite pathway once the substrate potential is properly aligned to the protein redox level and, as the substrate potential is moved away the

protein redox midpoint, STM images are immediately affected. Similarly the experiments were repeated with YCC and a typical example of the obtained STM images is shown in Fig. 56. The YCC molecules are stable between +150 mV_{SHE} and +380 mV_{SHE}, but we did not detect any change in the image contrast upon sweeping substrate potential in this range, as also observed by other groups [188].

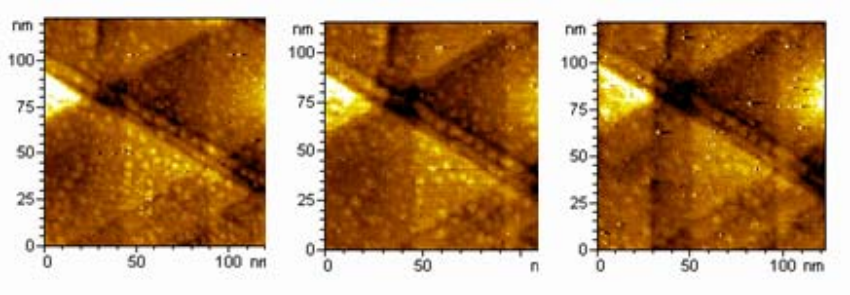

Fig. 56. Sequence of in situ STM images recorded under electrochemical control in buffer. Left, +150 mV_{SHE}; centre +380 mV_{SHE}; right, +500 mV_{SHE}. Vertical range 2.5 nm.

For further increase in electrochemical potential, the image quality starts to deteriorate and becomes no more reproducible when reaching 500 mV_{SHE}. Such deterioration is explained in terms of reorganization of the substrate, in fact, it is well known that the crystal orientation of gold can switch from (111) to (100) when the electrochemical potential exceeded a certain value [189]. One has to notice that, as seen for the PCSH mutant, immobilised on gold via a single thiol group, the heme active site of YCC seems not to be the unique pathway for the tunnelling process between tip and substrate through the molecule.

5.4 Molecular Dynamics Simulations

The RMSF of YCC adsorbed onto the gold surface ($<\Delta r^2>^{1/2}$=(0.015± 0.002)nm) again reveal a marked decrease in the RMSF values, with respect to that of free protein (($<\Delta r^2>^{1/2}$=(0.05 ± 0.02)nm). Therefore, as already observed for AZ and PCSS, YCC, covalently bound to a surface, reveals a significant reduction of its flexibility. It is interesting to note that a reduction in the RMSF is observed for proteins characterized by both α and β structures. Such behaviour suggests that the secondary structure does not drastically affect the flexibility of the macromolecule anchored to a substrate.

In analogy with what done for AZ and PCSS, the arrangement of the protein, with respect to the gold substrate, during the simulation, has been analyzed by taking into account the orientation of the heme group with respect to the gold substrate. In particular, the angle α, giving the orientation of the normal vector to the gold plane, is reported in Fig. 57 as a function of the simulation time. The α angle oscillates around a rather constant value with a rather small spread. This means that the variability in the orientation of the heme, and then of the protein, with respect to the gold substrate is rather restricted. In other words, YCC maintains an almost fixed orientation with respect to the gold surface. Such behaviour is in a qualitative agreement with what observed for YCC attached to a self-assemble monolayer [166] for which, however, the average values of the α angle results to be higher.

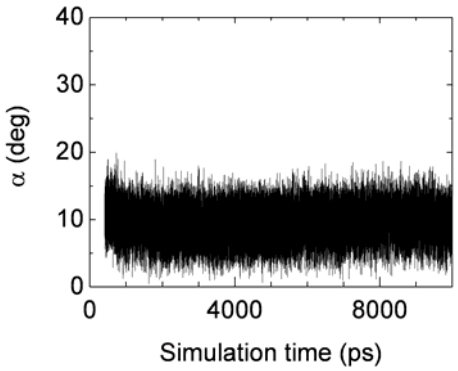

Fig. 57. Temporal evolution, along a 10 ns MD trajectory, of the α angle describing the orientation of the heme group with respect to gold surface normal, for YCC. The mean value and the standard deviation of α are (9±2)°.

The ellipsoid centered at the center of mass of the protein and oriented as its main inertia axes, evaluated from the MD simulated trajectories, and its corresponding height over the gold substrate has been extracted in order to compare MD simulated and AFM data. The histogram of the heights, as obtained by 1000 structures, shown in Fig. 58, reveals a single mode distribution. The mean value is consistent with the crystallographic data by assuming that protein is anchored to gold via the disulphide bridge (h ~ 3 nm). Additionally, the spread in the protein height over the substrate is indicative of the fact that, during its dynamical evolution, the macromolecule, can assume a variety of arrangements with respect to the gold substrate. In this respect, it is interesting to note that, in comparison to PCSS-I, YCC reveals a smaller standard deviation value for the height. Therefore, even if both the protein systems are bound to the gold substrate by a single bond, YCC is characterized by a reduced heterogeneity in the height; such behaviour could be generally attributed to the reduced mobility which generally characterizes YCC bound to gold. On the other hand, the rather spherical shape of this protein conformation should be also taken into account.

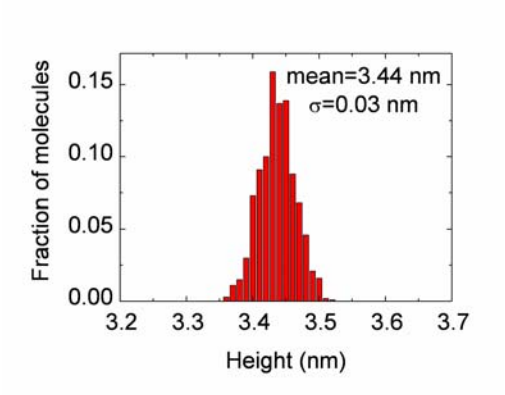

Fig. 58. Statistical analysis of the YCC height above the Au(111) substrate, as extracted from 1000 molecular structures sampled every 10 ps of 10 ns MD simulated trajectories.

The height distribution, as extracted by MD simulation, results to be again narrower if compared to that derived by TMAFM for YCC. Such a difference could be explained by considering similar considerations already done for AZ and PCSS.

6 Conclusions

In the present chapter the possibility to connect functional redox proteins to metal electrodes has been deeply investigated. The ability to create an appropriate connection between metallic electrode and functional biomolecules, and to convert biological functions into a detectable signal, is a fundamental step for applications in bionanotechnology and requires full characterization of the adsorbed proteins in terms of redox functionality, as well as topological and conductive properties, at the level of single molecule.

Three different redox proteins have been here examined upon adsorption on gold electrodes: wild type AZ and YCC, naturally bearing sulfur based anchoring groups for covalent linkage to gold electrode, and PC which, conversely, has been suitably mutated to introduce cysteine residues for chemisorption on gold. An extensive characterization has been performed to test the morphological, conductive and functional characteristics of the adsorbed proteins. The combination of different techniques, such as SPM, CV and MD simulations, has demonstrated to be extremely powerful for a deep study of such hybrid systems at the level of single molecule.

The investigated metalloproteins do not display mobility or formation of aggregates on the gold substrate. High-resolution and stable best-quality AFM and STM imaging is indicative, for all systems examined, of individual biomolecules robustly anchored to the gold electrode, as expected for covalent immobilization. Protein lateral dimensions and height on the gold substrate agree well with crystallographic data as for nondenaturing adsorption of the molecules on bare Au(111) surface, even if for AZ a low-height form of adsorbed molecules is observed as well, possibly connected to a denatured percentage of adsorbed molecules.

Importantly, the functionality of all adsorbed redox metalloproteins has been herein widely demonstrated by CV experiments. Indeed, the well-defined voltammetric response of the adsorbed molecules has provided a measure of the redox potentials, which are in good agreement with the formal potential for the three systems investigated. Additionally, the linear dependence of peak currents on voltage scan rate is indicative of a redox process of adsorbed species. The redox activity of metalloproteins is even confirmed, at the single molecule level, by ECSTM which in some cases (AZ and PCSS) gives evidence of a tunnelling mechanism likely assisted by the redox active site. Conversely, this behavior is not observed for YCC and PCSH, for which we can hypothesize that the higher protein flexibility (resulting from immobilisation via a single sulfur based group) as indicated by the broader height distribution of these adsorbed molecules, may result in unfavorable alignment of molecular redox levels with tip and substrate Fermi levels.

The protein conductive properties have been investigated by both STS and CAFM measurements. In air the STS investigation revealed asymmetric I-V characteristics for the redox protein anchored with a SS group (AZ and PCSS), whereas mainly symmetric I-V relations for single SH immobilisation is registered. Paying particular attention to possible factors influencing conduction through a tunnelling junction, we found that asymmetric and symmetric characteristics are affected by the experimental conditions (air or nitrogen

atmosphere) and by the tunnelling gap width (different starting tunnelling conditions). On the basis of these results, it is difficult to separate the intrinsic protein conduction from the contribution of such factors and the importance to establish an appropriate tip molecule contact emerges. This has been achieved by CAFM, which uses a metal probe to directly contact the protein adlayer. A sigmoidal I-V relation was detected in the same bias region explored in STS analysis, with a more symmetric behaviour for protein immobilised via SH group and asymmetric for those adsorbed through a disulfide, whereas in the low bias range an ohmic relation was identified. Despite their similarity in functionality and three dimensional structures, remarkable differences were observed for the copper proteins when studying their conductance as function of compression. In fact, while AZ presents a monotonically decreasing resistance when increasing the compressional forces, the PC mutants show the occurrence of a critical pressure, which determines a jump in the conduction of the biomolecular junction. Similar features are observed for cytochrome, even if a more complicated relation is revealed. These results suggest that electron transport through the gold/biomolecule/gold junction can be strongly influenced by the variation of the structural and functional properties of the inserted protein. Nevertheless, efficient conduction through the molecule towards the electrode has been observed for all the biomolecules investigated, as expected for a covalent linkage to gold, thus assessing good coupling to the electrode.

Our analysis has also taken advantage of MD simulations techniques. Specifically, MD capabilities have been exploited to more deeply investigate the dynamic response and flexibility of the adsorbed macromolecules. Relating MD simulations and experimental data has offered new insight to the understanding of how anchoring to gold may affect protein structure and how the dynamics of the adsorbed protein is reflected in the topological properties of the adsorbed molecules.

The characterization here presented has demonstrated the possibility to stably adsorb redox-active metalloproteins on a metal electrode, with controlled molecular density. The fully preserved functionality found for the adsorbed molecules, along with the good coupling with the electrode, provide clear indication of redox protein efficacy in integration with electronic components. In addition, the present study indicates that the use of genetic engineering can be successfully applied to redox biomolecules for improving the communication with the metal electrode, thus expanding possible applications of hybrid systems to biosensors and biocatalytic devices.

In conclusion, the efficient ET capabilities of adsorbed molecules, their nanoscale dimensions and, importantly, the possibility of gating redox activity, offer the basic ground for the exploitation of protein redox properties in bio-nanodevices. This represents a good starting point also to build up hybrid systems able to interact with their physiological redox partner. Such systems may constitute the basic element for assembling biosensors, which find application in several fields.

The multidisciplinary approach, involving biology, chemistry, physics and surface science confirms to have unique potentiality to indicate future directions and opportunities in the progressing field of molecular biolelectronics.

Acknowledgements

This work has been partially supported by the 'Molecular Nanodevices' FIRB-MIUR Project, by the EC Project SAMBA (V Frame FET) and the Cost-Action D21. SAMBA (V Frame FET). We thank Elena Brunori for generating Figs. 1 and 2.

References

[1] I. Willner and B. Willner, *Trends in Biotech*. **19**, 222 (2001).
[2] I. Willner, *Science*, **298** 2407 (2002).
[3] J. S. Marvin and H. W. Hellinga, *Proc. Natl. Acad. Sci. USA* **98,** 4955 (2001).
[4] L.-Q. Gu, S. Cheley, H. Bayley, *Science* **291**, 636 (2001)
[5] Mathias Lösche, *Curr. Opin. Sol. State and Mat. Sci*. **2,** 546 (1997).
[6] G.V. Nazin, X.H. Qui, *W. Hom Science* **302**, 77 (2003).
[7] D.G.Castner, B.D.Ratner, *Surf. Sci*. **500**, 28 (2002).
[8] C. Lowe, *Curr. Opin. Struct. Biol*. **10**, 428 (2000).
[9] D. M. Adams, L. Brus, C.E.D. Chidsey, S. Creager, C. Creutz, C.R. Kagan, P.V. Kamat, X M. Lieberman, S. Lindsay, R.A. Marcus, R.M. Metzger, M.E. Michel-Beyerle, J.R. Miller, M.D. Newton, D.R. Rolison, O. Sankey, K.S. Schanze, J. Yardley, Xiaoyang Zhu, *J. Phys. Chem. B* **107**, 6668 (2003).
[10] K. Sigfridsson, M. Ejdeback, M. Sundahl, O. Hasson, *Arch. Biochem. Biophys*. **351**, 197 (1998).
[11] W. Haehnel, T. Jansen, K. Gause, R.B. Klösgen, B. Stahl, D. Michl, B. Huvermann, M. Karas, R.G. Hermann, *EMBO J.* **13**, 1028 (1994).
[12] G. Gilardi, A. Fantuzzi, Trends in Biotechnology. 2001, 19, 468; G. Gilardi, A. Fantuzzi, S. J. Sadeghi, *Current Opinion in Structural Biology* **11**, 491 (2001)
[13] D.I.Gittins, D. Bethell, D.J.Schiffrin, R.J.Nichols, *Nature* **408**, 67 (2000).
[14] A.N. Shipway and I.Willner, *Acc. Chem. Res*. **34**, 421 (2001).
[15] Ch. Loppacher, M. Guggisberg, O. Pfeiffer, E. Meyer, M. Bammerlin, R. Lüthi, R. Schlittler, J. K. Gimzewski, H. Tang, *C. Joachim, Phys. Rev. Lett*. **90**, 066107 (2003).
[16] Y. Xiao, F. Patolsky, E. Katz, J. F. Hainfeld, I. Willner, *Science* **299**, 1877 (2003).
[17] G.M. Whitesides, J.P.Mathias, C.T.Seto, *Science* **254**, 1312 (1991).
[18] S. Ferretti, S. Paynter, D.A. Russell, K.E. Sapsford, D.J. Richardson *Trends Anal. Chem*. **19**, 530 (2000).
[19] T. Sagara, K.Niwa, A. Sone, C. Hinnen, K. Niki, *Langmuir* **6**, 254 (1990).
[20] I. Taniguchi, K. Watanabe, M. Tominaga, F. M. Hawkridge, *J. Electroanal. Chem*. **333**, 331 (1992).
[21] I. Willner, E. Katz, *Angew. Chem. Int. Ed*. **39**, 1180 (2000).
[22] J. Wei, H. Liu, A. R. Dick, H. Yamamoto, Y. He, David H. Waldeck, *J. Am. Chem. Soc*. **124**, 9591 (2002).
[23] Z. Salamon, J. T. Hazzard, G. Tollin, *Proc. Natl. Acad. Sci. USA* **90**, 6420 (1993).
[24] T. Sagara, H. Murumaki, S. Igarashi, H. Sato, K. Niki, *Langmuir* **7**, 3190 (1991).
[25] S. Boussad and N.J.Tao, *J. Am. Chem. Soc*. **121**, 4510 (1999).

[26] Y.M. Lvov, Z. Lu, J.B. Schenkman, X. Zu, J.F. Rusling, Direct electrochemistry of Mb and cyt P450cam in alternate layer-by-layer films with DNA and other polyions, *J. Am. Chem. Soc*. **120**, 4073 (1998).
[27] D. E.Weisshaar, B. D. Lamp, M. D. Porter, *J. Am. Chem. Soc*. **114**, 5860 (1992).
[28] A. Ulman, *Chem. Rev*. **96**, 1533 (1996).
[29] J. Madoz, B.A.Kuznestov, F.J.Medrano, J.L. Garcia, V.M.Fernandez, *J. Am. Chem. Soc*. **119**, 1043 (1997).
[30] O. Cavalleri, C. Natale, M.E. Stroppolo, A. Relini, E. Cosulich, S. Thea, M. Novi, A. Gliozzi *Phys. Chem. Chem. Phys*. **2**, 4630 (2000).
[31] Q. Chi, J. Zhang, J.Andersen, J.E.T. Ulstrup, *J. Phys. Chem. B* **105**, 4669 (2001).
[32] J. J. Davis, D. Djuricic, K. K.W. Lo, E. N. K. Wallace, L.-L. Wong, H. A. Hill, *Faraday Discuss*. **116**, 15 (2000).
[33] X. Chen, R. Ferrigno, J. Yang, G. Whitesides, *Langmuir* **18**, 7009 (2002).
[34] L. Gorton, A. Lindgren, T. Larsson, F.D.Munteanu,T. Ruzgas, I.Gazaryan, *Analytica Chimica Acta* **400**, 91 (1999).
[35] R.G. Nuzzo, B.R. Zegarski, L.H. Dubois, *J. Am. Chem. Soc*. **109**, 733 (1987).
[36] H. Grönbeck, A. Curioni, W. Andreoni, *J. Am. Chem. Soc*. **122**, 3839 (2000).
[37] E.P. Friis, J.E.T. Andersen, Y.I. Kharkats, A.M. Kuznestov, R.J. Nichols, J.-D. Zhang, J. Ulstrup, *Proc. Nat. Acad. Sci. USA* **96**, 1379 (1999).
[38] Q. Chi, J. Zhang, J.U. Nielsen, E.P. Friis, I. Chorkendor, G.W. Canters, J.E.T. Andersen, J. Ulstrup, *J. Am. Chem. Soc*. **122**, 4047 (2000).
[39] J.J. Davis, H.A.O. Hill, A.M. Bond, *Coord. Chem. Rev*. **200–202**, 411 (2000).
[40] P. Facci, D. Alliata, S. Cannistraro, *Ultramicroscopy* **89**, 291 (2001).
[41] J. J. Davis, C. M. Halliwell, H. A. O. Hill, G.W. Canters, M. C. Van Amsterdam, M. *Ph. Verbeet, New. J. Chem*. **10**, 1119 (1998).
[42] J. J. Davis, H. A. O. Hill, *Chem. Commun*. 393 (2002).
[43] J.J. Davis, D.Bruce, G.W.Canters, J.Crozier, H.A.Hill, *Chem. Comm*. 576 (2003).
[44] L. Andolfi, S. Cannistraro, G.W. Canters, P. Facci, A. G. Ficca, I. M. C. Van Amsterdam, M. Ph. Verbeet, *Arch. Biochem. Biophys*. **399**, 81 (2002).
[45] K.W. Hipps, *Science* **294**, 536 (2001).
[46] X. D. Cui, A. Primak, X. Zarate, J. Tomfohr, O. F. Sankey, A. L. Moore, T. A. Moore, D. Gust, G. Harris, S. M. Lindsay, *Science* **294**, 571 (2001).
[47] B. Bonanni, D. Alliata, A.R. Bizzarri, S. Cannistraro, *Chem. Phys. Chem*. **4**, 1183 (2003).
[48] P. Friis, J.E.T. Andersen, L.L. Madsen, P. Møller, R.J. Nichols, K.G. Olsen, J. Ulstrup, *Electrochimica Acta* **43**, 2889 (1998).
[49] R.H. Holm, P. Kennepohl, E.I. Solomon, *Chem Rev*. **96**, 2239 (1996).
[50] L. Andolfi, B. Bonanni, G.W. Canters, M.Ph. Verbeet, S. Cannistraro, *Surf. Science* **530**, 181 (2003).
[51] A.R. Bizzarri, B. Bonanni, G. Costantini, S. Cannistraro, *Chem. Phys. Chem*. **4** 1189, (2003).
[52] A.R. Bizzarri, G. Costantini, S. Cannistraro, *Biophys. Chem*. **106**, 111 (2003).
[53] L. Andolfi, G.W. Canters, M.Ph. Verbeet, S. Cannistraro, *Biophys. Chem*. **107**, 107 (2004).
[54] L. Andolfi, D. Bruce, S. Cannistraro, G.W. Canters, J.J. Davis, H.A.O. Hill, J. Crozier, M.Ph. Verbeet, C.L. Wrathmell, Y.Astier. *J. Electroanal. Chem***. 565,** 21 (2004).

[55] M. Amrein, *STM and SFM in Biology*, ed. by O. Marti (Academic Press Inc., San Diego, CA, 1993).
[56] A. Engel, *Annu. Rev. Biophys. Chem*. **20**, 79 (1991), and references therein.
[57] R. Mukhopadhyay, *Curr. Sci*. **84**, 1202 (2003), and references therein.
[58] R. Sonnenfeld, P.K. Hansma, *Science* **232**, 211 (1986).
[59] H.Y. Liu, F. Fan, C.W. Lin, A. Bard, *J. Am. Chem. Soc*. **108**, 3838 (1986).
[60] S. M. Lindsay, T. Thundat, L. Nagahara, U. Knipping, R.L. Rill, *Science* **244**, 1063 (1989).
[61] J. Zhang, Q. Chi, A.M. Kuznetsov, A.G. Hansen, H. Wackerbarth, H.E.M. Christensen, J.E.T. Andersen, J. Ulstrup, *J. Phys. Chem. B* **106**, 1131 (2002).
[62] J. Zhang, Q. Chi, S. Dong, E. Wang, *Bioelectrochem. Bioener*. **39**, 267 (1996).
[63] A. Aviram, *Molecular Electronics-Science and Technology* (AIP, New York, 1992).
[64] E.P. Friis, J.E.T. Andersen, L.L. Madsen, P. Møller, J. Ulstrup, *J. Electroanal. Chem*. **431**, 35 (1997).
[65] J. Zhang, A. M. Kuznetsov, J. Ulstrup, *J. Electroanal. Chem*. **541**, 133 (2003).
[66] W. Schmickler, *J. Electroanal. Chem*. **296**, 283 (1990).
[67] G.B. Khomutov, L.V. Belovolova, S.P. Gubin, V.V. Khanin, A.Yu. Obydenov, A.N. Sergeev-Cherenkov, E.S. Soldatov, A.S. Trifonov, *Bioelectrochem*. **55**, 177 (2002).
[68] P.B. Lukins, T. Oates, *Biochim. Biophys. Acta* **1409**, 1 (1998).
[69] A. Vaught, T. W. Jing, S. M. Lindsay, *Chem. Phys. Lett*. **236**, 306 (1995).
[70] J.R. Hahn, Y.A. Hong, H. Kang *Applied Phys A* **66**, S467 (1998).
[71] G. Binning, C. F. Quate, Ch. Gerber, *Phys. Rev. Lett*. **56**, 930 (1986).
[72] S. Karrasch, R. Hegerl, J. H. Hoh, W. Baumeister, A. Engel, *Proc. Natl. Acad. Sci.* USA **91**, 836 (1994).
[73] D.M. Czajkowsky, Z. Shao, *FEBS Lett*. **430**, 51 (1998).
[74] S.Scheuring, P.Ringler, M. Borgnia, H.Stahlberg, D.J.Müller, P.Agre and A.Engel, *The EMBO Journal* **18**, 4981 (1999).
[75] Q. Zhong, D. Innis, K. Kjoller, V.B.Elings, *Surf. Sci*. **290**, L688 (1993).
[76] P.K. Hansma, J.P.Cleveland, M. Radmacher, D.A. Walters, P.E. Hillner, M. Bezanilla, M.Fritz, D.Vie, H.G. Hansma, C.B. Prater, J. Massie, L.Fukunaga, J. Gurley, V. Ellings, *Appl. Phys. Lett*.**64**, 1738 (1994).
[77] E. Henderson, P. G. Haydon, and D. S. Sakaguchi, *Science* **25**, 1944 (1992).
[78] J. Putman, K.O. van der Werf, B.G. de Grooth, N.F. van Hulst, and J. Greve, *Biophys. J.* **67**, 1749 (1994).
[79] A. Jeremic, M.Kelly, S.J.Cho, M.H. Stromer, B.P. Jena, *Biophys. J.* **85**, 2035 (2003).
[80] M. Radmacher, M. Fritz, H. G. Hansma, and P. K. Hansma, *Science* **265**, 1577 (1994).
[81] S. Kasas, N. H. Thomson, B. L. Smith, H. G. Hansma, X. Zhu, M. Guthold, C. Bustamante, E. T. Kool, M. Kashlev, and P. K. Hansma, *Biochemistry* **36**, 461 (1997).
[82] H. G. Hansma, *Annu. Rev. Phys. Chem*. **52**, 71 (2001) and references therein.
[83] E.-L. Florin, V. T. Moy, and H. E. Gaub, *Science* **264**, 415 (1994).
[84] P. Hinterdorfer, W. Baumgartner, H.J. Gruber, K. Schilcher, H. Schindler, *Proc. Natl. Acad. Sci. USA* **93**, 3477 (1996).
[85] F.A.Schabert, J.P.Rabe, *Biophys. J.* **70**, 1514 (1996).
[86] C. Möller, M. Allen, V. Elings, A. Engel, D J. Müller, *Biophys J.* **77**, 1150 (1999).
[87] G.-Y. Liu, N.A. Amro, *Proc. Nat. Acad. Sci. USA* **99**, 5165 (2002).
[88] M. Bergkvist, J. Carlsson, S. Oscarsson, *J. Phys. Chem. B* **105**, 2062 (2001).

[89] A. Ivarsson, P. O. Hegg, I. Lundstrom, U. Jonsson, *J. Colloid Interface Sci.* **13**, 169 (1985).
[90] M. Mrksich, G.B. Sigal, G. M. Whitesides, *Langmuir* **11**, 4383 (1995).
[91] D. Kowalczyk, S. Slomkowski, *J. Bioact. Comput. Pol*. **9**, 282 (1994).
[92] J. R. Lu, T. J. Su, P. N. Thirtle, R. K. Thomas, A. R. Rennie, R. J. Cubitt, *Colloid Interface Sci.* **206**, 212 (1998).
[93] S. John, T. Van Noort, K.O. Van der Werf, B.G. De Grooth, N.F. Van Hulst, J. Greve, *Ultramicroscopy* **69**, 117 (1997).
[94] H. Park, J. Park, A. Lim, E.H. Anderson, A.P. Alivisatos, P.L. McEuen, *Nature* **407**, 57 (2000).
[95] J. Chen, M.A. Reed, A.M. Rawleet, J. M. Tour, *Science* 286, 1550 (1999).
[96] C.P. Collier, E.W. Wong, M. Belohradsky, F.M. Raymo, J.F. Stoddart, P.J. Kuekes, R.S. Williams, J.R. Heath, *Science* **285**, 391 (1999).
[97] K. Slowinski, R.V. Chamberlain, R. Bilewicz, M. Majda, J. Am. Chem. Soc. **18**, 4709 (1996); (b) R.E. Holmlin, R.F. Ismagilov, V. Mujica, M.A. Ratner, M.A. Rampi, G.M. Whitesides, *Angew. Chem. Int. Ed*. **40**, 2316 (2001).
[98] D. Alliata, L. Andolfi, S. Cannistraro, *Ultramicroscopy* **101,** 231 (2004).
[99] D.J. Wold, C.D. Frisbie, J. Am. Chem. Soc. **122**, 2970 (2000); (b) D. J. Wold, C.D. Frisbie, *J. Am. Chem. Soc*. **123**, 5549 (2001).
[100] D.J. Wold, R. Haag, M.A. Rampi, C.D. Frisbie, J. Phys. Chem. B **106**, 2813 (2002).
[101] Y. Selzer, A. Salomon, D. Cahen, *J. Phys. Chem. B* **106**, 10432 (2002).
[102] K. Ramachandran, J.K. Tomfohr, J.Liu, O.F. Sankey, X. Zarate, A. Primak, Y. Terazono, T. A. Moore, A. L. Moore, D. Gust, L. A. Nagahara, S.M. Lindsay, *J.Phys. Chem. B* **107**, 6162 (2003).
[103] G. Leatherman, E.N. Durantini, D. Gust, T.A. Moore, A.L: Moore, S. Stone, Z. Zhou, P. Rez, Y.Z. Liu, S.M. Lindsay J.Phys. Chem. B **103**, 4006 (1999); (b) T. Ishida, W. Mizutani, Y. Aya, H. Ogiso, S. Sasaki, H. Tokumoto *J. Phys. Chem. B* **106**, 5886 (2002).
[104] J. Zhao, J.J. Davis, *Nanotechnology* **14**, 1023 (2003).
[105] B. Schnyder, D. Alliata, R. Kotz, H. Siegenthaler, *Appl. Surf. Sci*. **173**, 221 (2001); M.G. Sullivan, B. Schnyder, M. Bärtsch, D. Alliata, C. Barbero, R. Imhof, and R. Kötz *J. Electrochem. Soc*. **147**, 2636 (2000).
[106] F.A. Armstrong, R. Camba, H.A. Heering, J.Hirst, L. J.C. Jeuken, A.K. Jones, C.Leger, J.P. McEvoy, *Faraday Discuss*. **16**, 191 (2000).
[107] D. Alliata, R. Kötz, O. Haas, H. Siegenthaler, *Langmuir* **15**, 8483 (1999).
[108] D. Alliata, R. Kötz, P. Novák and H. Siegenthaler, *Electrochem. Comm*. **2**, 436 (2000).
[109] H. Hamann, A. Hamnett, W. Vielstich, in *Electrochemistry* (Ed: Wiley-VCH, New York 1998) p. 235.
[110] F.A. Armstrong, *J. Chem. Soc. Dalton. Trans*. **5**, 661 (2002).
[111] F.A. Armstrong, H.A. Heering, *J. Hirst, Chem. Soc. Rev*. **26**, 169 (1997).
[112] L.J.C. Jeuken, P. van Vliet, M.P. Verbeet, R. Camba, J.P. McEvoy, F.A. Armstrong, G.W. Canters, *J. Am. Chem. Soc*. **122**, 12186 (2000).
[113] J. Hirst, F.A. Armstrong, *Anal. Chem*. **70**, 5062 (1998).
[114] J. A. McCammon and S. C. Harvey, *Dynamics of Protein and Nucleic Acid*, (Cambridge University Press, Cambridge, 1987).

[115] C.L. Brooks, R.E. Bruccoleri, B. D. Olafson, D. J. Statos, S. Swaminathan, and M. Karplus, *J. Comp. Chem*. **4**, 187 (1983).
[116] W. F van Gunsteren and H.J.C. Berendsen, Angew. *Chem. Int. Ed. Engl*. **29**, 992 (1991).
[117] Jr.A.D. MacKerrell, D. Bashford, M. Bellott, Jr.R.L. Dunbrack, J.D. Evanseck, M.J. Field, S. Fischer, J. Gao, H. Guo, S. Ha, D. Joseph-McCarthy, L. Kuchnir, K. Kuczera, F.T.K. Lau, C. Mattos, S. Michnick, T. Ngo, D. T. Nguyen, B. Prodhom, W.E. Reiher III, B. Roux, M. Schlenkrich, J.C. Smith, R. Stote, J.M. Straub, M. Watanabe, J. Wiorkiewicz-Kuczera, D. Yin, and M. Karplus, *J. Phys. Chem. B* **102**, 3586 (1998).
[118] W.F van Gunsteren and H.J.C. Berendsen, *Groningen Molecular Simulation (GROMOS) Library Manual*, Biomos: Groningen, 1987.
[119] W.D. Cornell, P. Cieplak, C.I. Bayly, I. R. Gould, K.M. Jr. Merz, D.M. Ferguson, D.C. Spellmeyer, T. Fox, J. W. Caldwell, and P.A. Kollman, *J. Am. Chem. Soc*. **117**, 5179 (1995).
[120] H.J.C.Berendsen, J.R. Grigera, and T. P. Straatsma, *J. Phys. Chem*. **91**, 6269 (1987).
[121] W.L. Jorgensen, J. Chandrasekhar, J.D. Madura, R.W. Impey, and M. L. Klein, *J. Chem. Phys* **79**, 926 (1983).
[122] M.P. Allen, and D.J. Tisley, *Computer Simulation of Molecular Liquids*; Clarendon Press: Oxford, 1987.
[123] P.J. Steinbach and B.R. Brooks, *J. Comput. Chem*. **15**, 57 (1994).
[124] P.E. Smith, H.D. Blatt, and B. M. Pettitt, *J. Phys. Chem. B* **101**, 3886 (1997).
[125] J.P. Ryckaert, G. Ciccotti, H. J. C. Berendsen, *J. Comput. Phys*. **23** 327 (1977).
[126] H. Nar, A. Messerschmidt, R. Huber, M. van de Kamp, G.W. Canters, *J. Mol. Biol*. **218** 427 (1991).
[127] C. Arcangeli, A.R. Bizzarri, and S. Cannistraro, *Biophys. Chem*. **90** 45 (2001).
[128] M. Milani, L. Andolfi, S. Cannistraro, M.Ph. Verbeet, M. Bolognesi, *Acta Cryst. D* **57**, 1735 (2001).
[129] A. Ciocchetti, A.R. Bizzarri, and S. Cannistraro, *Biophys. Chem*. **69** 185 (1997).
[130] G.V.Louie and G.D.Brayer *J. Mol. Biol*. **214** 527 (1990).
[131] N. V. Prabhu, S. D. Dalosto, K. A. Sharp, W. W. Wright, and J. M. Vanderkooi, *J. Phys. Chem. B*, **106**, 5561 (2002).
[132] M.C. Vargas, P. Giannozzi, A. Selloni, and A.J. Scoles, *J. Phys. Chem. B* **105** 9509 (2001).
[133] S.Nose, *J. Chem. Phys*. **81**, 51 (1984).
[134] W.G. Hoover, *Phys. Rev. A* **31**, 1695 (1985).
[135] B.G. Karlsson, T. Pascher, M. Nordling, R. H. A. Ardvisson, L. G. Lundberg, *FEBS Lett*. **211**, 246 (1989).
[136] S. Hu, I.K. Morris, J.P. Singh, K.M.Smith, T.G. Spiro, *J. Am. Chem. Soc*. **115**, 12446 (1993).
[137] J. Bukowska, K. Jackowska, *Electrochim. Acta*, **35**, 315 (1990).
[138] J.Zhang, Q.Chi, J.U.Nielsen, A.G.Hansen, J.E.T. Andersen, H.Wackerbarth, J. Ulstrup, *Russian J. Electrochem*. **38**, 68 (2002).
[139] P. Markiewicz, M. C. Goh, *J. Vac. Sci. Technol. B* **13**, 1115 (1995).
[140] J. Vesenka, M. Guthold, C. L. Tang, D. Keller, E. Delain and C. Bustamante, *Ultramicroscopy* **42**, 1243 (1992).
[141] D. Losic, J.G. Shapter, J.J. Gooding, *Langmuir* **18**, 5422 (2002).

[142] S.L. Tang and A.J. McGhie, *Langmuir* **12**, 1088 (1996).
[143] A. Bertazzon, B.M. Conti-Tronconi, M.A. Raftery, *Proc. Nat. Acad. Sci. USA* **89**, 9632 (1992).
[144] G. Leanna, D. Cyr, K. Muyskens, G.W. Flynn, *Langmuir* **14**, 1465 (1998).
[145] S.J. Sowerby, M. Edelwirth, M. Reiter, W.M. Heckl, *Langmuir* **14**, 5195 (1998).
[146] S. A. Contera, H. Iwasaki, *Ultramicroscopy* **91**, 231 (2002).
[147] W. Han, E.N. Durantini, T.A. Moore, A.L. Moore, D. Gust, P. Rez, G. Leatherman, G.R. Seely, N. Tao, S.M. Lindsay, *J. Phys. Chem. B* **101**, 10719 (1997), and references therein.
[148] M. Heim, R. Steigerwald, R. Guckenberger, *J. Struc. Biol*. **119**, 212 (1997).
[149] F-R.F. Fan, A.J. Bard, *Proc. Natl. Acad. Sci. U.S.A*. **96**, 14222 (1999).
[150] M. Kuznetsov and J. Ulstrup, *J. Phys. Chem. A* **104**, 11531 (2000).
[151] U. Mazur and K.W. Hipps, *J.Phys. Chem. B* **103**, 9721 (1999).
[152] L. Scudiero, D.E. Barlow, U.Mazur, K.W. Hipps, *J. Am. Chem. Soc*. **123**, 4073 (2001).
[153] K.W. Hipps, D.E. Barlow, U.Mazur, *J. Phys. Chem. B* **104**, 2444 (2000).
[154] A. Aviram and M.A. Ratner, *Chem Phys. Lett*. **29**, 277 (1974).
[155] R.M. Metzger, *Acc. Chem. Res*. 32, 95 (1999).
[156] M.L. Chabinyc, X. Chen, R.E. Holmlin, H. Jacobs, H. Skulason, C.D. Frisbie, V. Mujica, M.A. Ratner, M.A. Rampi, G.M. Whitesides, *J. Am. Chem. Soc*. **124**, 11730 (2002).
[157] A.Troisi and M. Ratner, *J. Am. Chem. Soc*. **124**, 14528 (2002).
[158] A.J. Ikushima, T. Kanno, S. Yoshida, A. Maeda, *Thin Solid Films* **273**, 35 (1996).
[159] S. M. Lindsay, O. F. Sankey, Y. Li, C. Herbst, A. Rupprecht, *J. Phys. Chem*. **94**, 4655 (1990).
[160] Q. Chi, J. Zhang, E.P. Friis, J.E.T. Andersen, J. Ulstrup, *Electochem. Commun*. **1**, 91 (1999).
[161] D.M. Kolb, A.S. Dakkouri, N. Batina, *Nanoscale Probes of the Solid/Liquid Interface*, edited by A.A. Gewirth and H. Siegenthaler, NATO ASI Series Vol. 288, (Kluwer Academic Publishers: Dordrecht, 1995), pp 263-284.
[162] N.J. Tao, *Phys. Rev. Lett*. **76**, 4066 (1996).
[163] R.A. Marcus, *J. Chem. Phys*. **24**, 966 (1956).
[164] C. Smith, *Q. Rev. Biophys*. **24**, 227 (1991).
[165] A.R. Bizzarri, *J. Phys.: Cond. Matter* **16**, R1 (2004).
[166] C.E. Nordgren, D.J. Tobias, M.L. Klein, and L.K. Blaise, *Biophys. J*. **83**, 2906 (2002).
[167] M. Rief and H. Grubmueller, *Chem. Phys. Chem*. **3**, 255 (2002).
[168] F. Caruso, D. N. Furlong, K. Ariga, I. Ichinose, T. Kunitake, *Langmuir* **14**, 4559 (1998).
[169] N.D. Lang, *Phys. Rev. B* **52**, 5335 (1995).
[170] A.I. Onipko, K.-F. Berggren, Yu.O. Klymenko, L.I. Malysheva, J.J.W.M. Rosink, L.J. Geerlins, E. van der Drift, S. Radelaar, *Phys. Rev. B* **61**, 11118 (2000).
[171] U. Dürig, O. Züger, B. Michel, L. Häusslinh, H. Ringsdorf, *Phys. Rev. B* **48**, 1711 (1993).
[172] M. Heim, R. Eschrich, A. Hillebrand, H.F. Knapp, R. Guckenberger, G. Cevc, *J. Vac. Sci., Technol. B* **14**, 1498 (1996).
[173] M.-B. Song, J.-M. Jang, S.-E. Bae, C.-W. Lee, *Langmuir* **18**, 2780 (2002).

[174] N. Patel, M. C. Davies, M. Lomas, C. J. Roberts, S.J.B. Tendler, P.M. Williams, *J. Phys. Chem*. **101**, 5138 (1997).
[175] R. Guckenberger, M. Heim, G. Cevc, H. Knapp, W. Wiegräbe, A. Hillebrand, *Science* **266**, 1538-1541 (1994).
[176] Y.A. Hong, , J.R. Hahn, H. Kang, *J. Chem. Phys*. **108**, 4367 (1998).
[177] S. J. O'Shea, R.M. Atta, M.E. Welland, *Rev. Sci. Instrum*. **66**, 2508 (1995).
[178] J.J. Hopfield *Proc. Nat. Acad. Sci. USA* **71**, 3840 (1974).
[179] D.D.N. McLeod, H.C. Freeman, I. Harvey, P.A. Lay, A.M. Bond. *Inorg. Chem*. **35**, 7156 (1996).
[180] A. Szucs and M.Novak, *J. Electroanalytical Chem*. **383**, 75 (1995).
[181] H. Allen O. Hill, Nicholas I. Hunt, Alan M. Bond, *J. Electroanalytical Chem*. **436**, 17 (1997).
[182] Yanxiu Zhou, Tsutomu Nagaoka, Guoyi Zhu, *Biophys. Chem*. **79**, 55 (1999).
[183] P.D. Barker and A.G. Mauk, *J. Am. Chem. Soc*. **114**, 3619 (1992).
[184] A. Szucs and M.Novak, *J. Electroanalytical Chem*. **384**, 47 (1995).
[185] G.R. Moore and G.W. Pettigrew, *Cytochrome c: Evolution, Structural and Physicochemical Aspects*, (Springer-Verlag, Berlin 1990), p. 115.
[186] C. Marc Lett and J. Guy Guillemette, *Biochem. J*. **362**, 281 (2002).
[187] T. Sagara, K.Niwa, A.Sone, C.Hinnen, K.Niki, *Langmuir* **6**, 254 (1990).
[188] A.G. Hansen, A.Boise, J.U. Nielsen, H. Wackerbarth, I.Chorkendorff, J.E.T. Andersen, J. Zhang, J. Ulstrup, *Langmuir* **19**, 3419 (2003).
[189] O.M. Magnussem, F. Moeller, M.R. Vogt, R.J. Behm, in *Electrochemical Nanotechnology*, edited by W.J. Lorenz and W.Plieth (Wiley-VCH, Weinheim 1998) pp. 159-169.